UNIVERSITY OF CALIFORNIA

Los Angeles

Detection of Damage in a Composite Structure Using Guided Waves

A dissertation submitted in partial satisfaction of the

requirements for the degree of Doctor of Philosophy

in Mechanical Engineering

by

Harsh Kumar Baid

2012

ABSTRACT OF THE DISSERTATION

Detection of Damage in a Composite Structure Using Guided Waves

by

Harsh Kumar Baid

Doctor of Philosophy in Mechanical Engineering

University of California, Los Angeles, 2012

Professor Ajit K. Mal, Chair

Advanced composites are being increasingly used in state-of-the-art aircraft and aerospace structures. In spite of their many advantages composite materials are highly susceptible to hidden flaws that may occur at any time during the life of a structure and if undetected, may cause sudden and catastrophic failure of the entire structure. An example of such a structural component is the "honeycomb composite" in which thin composite skins are bonded with adhesives to the two faces of extremely lightweight and relatively thick metallic honeycombs. These components are often used in aircraft and aerospace structures due to their high strength to weight ratio. Unfortunately, the bond between the honeycomb and the skin may degrade with age and service loads can lead to separation of the load-bearing skin from the honeycomb (called "disbonds") and compromise the safety of the structure. The need for model-based studies is widely recognized in the NDE community and a great deal of work has indeed been carried out for simple, metallic structures. However the literature on composite structures is rather limited due to the enormous mathematical complexity involved in dealing with them. In

this dissertation a comprehensive approach including numerical (finite element method) and analytical method is used for calculating the ultrasonic wavefield in composite structural components with and without defects. Laboratory experiments are carried out on a composite honeycomb specimen containing damage to the skin or a localized disbond at the skin-core interfaces. The skin and the honeycomb composite are considered separately in order to understand the interaction of ultrasonic waves with damage in the two structures. The waves are launched into the specimen using a broadband PZT transducer and are detected by a distributed array of identical transducers located on the surface of the specimen. The guided wave components of the signals are shown to be strongly influenced by the presence of a defect in the skin or the honeycomb composite structure. The experimentally observed results are used to develop an autonomous scheme to locate the disbonds. The calculated results from the simulations are compared with existing and new experiments to validate and improve the models. The results should be very useful in model-based understanding of ultrasonic data collected during nondestructive inspection and evaluation (NDI/NDE) of advanced aircraft and aerospace structure and in the development of reliable health monitoring systems in the structures.

The dissertation of Harsh Kumar Baid is approved.

Vijay Gupta

William Klug

Jiann-Wen Ju

Ajit Mal, Committee Chair

University of California, Los Angeles

2012

TABLE OF CONTENTS

LIST OF FIGURES

LIST OF TABLES

ACKNOWLEDGEMENTS

I would like to express my profound gratitude and appreciation to my advisor Professor Ajit Mal, for his guidance, support, and encouragement throughout my study. His knowledge, imagination and insightfulness broadened my views and played an enormous role in my research. His intellectual guidance, work discipline and personal strengths inspired and taught me valuable skills that would be invaluable in my personal and professional life. I am greatly thankful to him for what I am today in life.

I am also grateful to Professor Vijay Gupta, Professor William Klug and Professor Jiann-Wen (Woody) Ju for agreeing to serve on my dissertation committee and for providing help and advice whenever needed.

I would like to extend my thanks to my former and current NDE laboratory colleagues, Dr. Sauvik Banerjee, Dr. Fabrizio Ricci and Mr. Himadri Samajder for their help during my research and to the undergraduate and graduate students working in the NDE laboratory for giving me the opportunity to engage in intellectual stimulating team work.

Finally, I must acknowledge the love, patience and support of my wife Sapna Baid and my parents.

VITA

EDUCATION:

- Ph.D. Candidate (Spring 2012)
- M.S. Mechanical Engineering (June 2009)
- B.S. Mechanical Engineering (June 2006)

  Department of Mechanical and Aerospace Engineering
  University of California at Los Angeles

RESEARCH AND TEACHING EXPERIENCE:

- UCLA Nondestructive Evaluation (NDE) Research Group
  Materials Degradation Characterization Laboratory (Summer 2005 - present)
  Los Angeles, California
  Graduate Student Researcher
- Teaching Assistant (Spring 2007 - Winter 2012):
  - Advanced Strength of Materials (MAE 156A)
  - Introduction to Finite Element Methods (MAE 168)
  - Mathematics of Engineering (MAE 182A)
  - Statics and Strength of Materials (MAE 101)
  - MS online cources (MAE 156A, MAE 168, and MAE 256A)

STUDENT SUPERVISION:

- HSSRP: High School Summer Research Program (Summer 2010 and 2011)
  - Supervised high school students in designing and conducting experiments in Materials Degradation Characterization Laboratory.
- CEED: Center for Excellence in Engineering & Diversity (Fall 2008)
  - Supervised freshmen students (E 87 course) in designing and conducting experiments in Materials Degradation Characterization Laboratory.
- MAE 199
  - Supervised undergraduate students in designing and conducting experiments in Materials Degradation Characterization Laboratory.

PUBLICATIONS

Conference Publications

- Indu Saxena, **Harsh Baid**, Narciso Guzman, Lothar U. Kempen, Ajit Mal, "Propagation loss with frequency of ultrasound guided waves in a composite metal-honeycomb structure," Proc. of SPIE, May 2009
- Sauvik Banerjee, Fabrizio Ricci, **Harsh Baid**, Ajit K. Mal, "Dynamic based damage detection in composite structures," Proc. of SPIE, Apr 2009
- **Harsh Baid**, Sauvik Banerjee, Shiv Joshi, Siddhartha Mal, "Detection of disbonds in a honeycomb composite structure using guided waves," Proc. of SPIE, Apr 2008
- Ajit Mal, Indu Saxena, **Harsh Baid**, and Dennis Keene, "Detection of disbonds in a honeycomb composite structure using guided waves," IWSHM, Stanford University, 2007

Oral and Poster Presentations

- "Dynamics Based Damage Detection in Composite Structures". MAE Research and Technology Review, UCLA Faculty Center, April 27th, 2012.
- "Damage Detection Techniques in Composite Structures Using Ultrasonic Guided Waves". 8th International Workshop on Structural Health Monitoring, pp 1923-1931, September 13-15, 2011 in Stanford, California.
- "A Conceptual Structural Health Monitoring System Based on Vibration and Wave Propagation". UCLA Engineering Tech Forum, April 23rd, 2009.
- "Dynamics Based Damage Detection in Composite Structures". UCLA Engineering Tech Forum, May 27th, 2008.

HONORS AND AWARDS

- Outstanding PhD Award in Mechanical Engineering, UCLA.
- Graduate fellowship from Mechanical and Aerospace Engineering Department, UCLA.

Chapter 1 INTRODUCTION

Advanced composites are being used increasingly in state-of-the-art aircraft and aerospace structures, due to their high specific stiffness and strength, and extremely low coefficient of thermal expansion. The new Boeing 787 and many Airbus models make extensive use of composites as their primary structural components. In addition, novel multifunctional composites are being developed both for commercial and military applications. The estimated use of composites in commercial aircraft is shown in Figure 1-1, the curves for military aircraft would probably be even steeper. It is well known that composite materials are highly susceptible to hidden flaws that may arise from manufacturing defects, foreign object impact, mechanical and thermal fatigue and other service related events. If these hidden flaws are undetected they can grow and lead to catastrophic failure of the structure. An example of such a catastrophic failure was explosion of the Delta II Launch Vehicle in January 1997 due to impact in the composite structures. The explosion was caused due to a hidden delamination in one of the strapped-on Graphite Epoxy Motors (GEMs) [1]. Other examples include the crash of the Airbus AA-587 due to loss of its composite vertical stabilizer and the explosion of a X-33 fuel tank also appear to have been caused by the presence of hidden delaminations [2, 3]. Since many of these defects can occur at any time during service of the structure, proper maintenance at regular intervals is critical to insure the safety of these structures, adding large amounts to their cost of operation and maintenance.

Life extension and safe operation of aircraft, aerospace and civil structures requires an intensive and costly program of inspection and maintenance at regular intervals. Methods to assess structural damage and cracks/delaminations in aircraft components without removing paint continue to remain cumbersome and labor-intensive requiring subjective judgment.

According to some estimates, over 25% of the life cycle cost of an aircraft or aerospace structure, which includes pre-production, production and post-production costs can be attributed to operation and support, involving inspection and maintenance. The life cycle cost of new aircraft and aerospace structures can be reduced significantly with the development of a more efficient nondestructive evaluation technology using an effective data collection system and an interpretation methodology based on fundamental physical models.

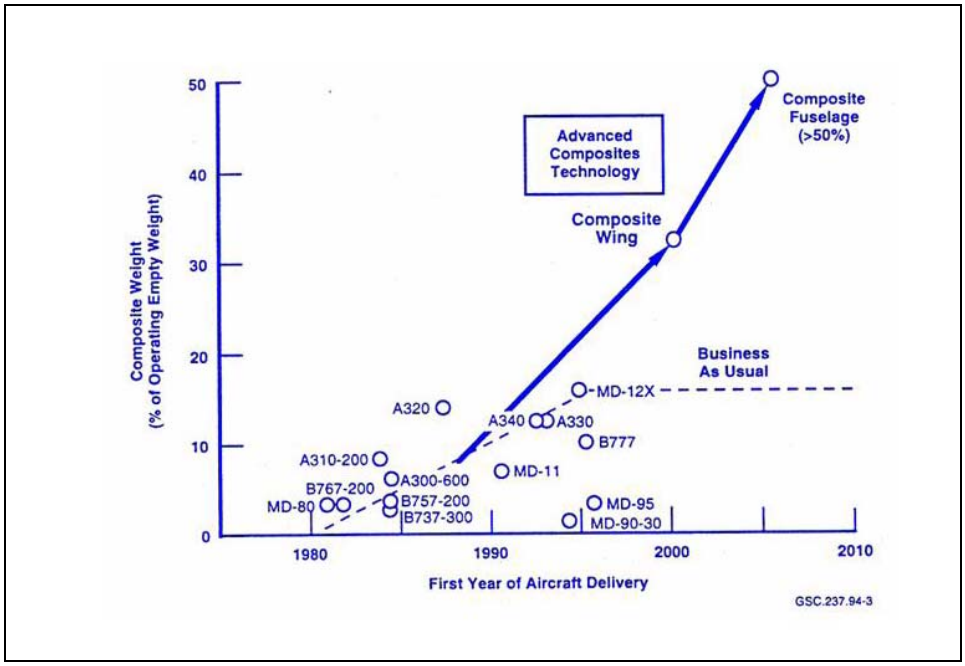

Figure 1-1: Composite in commercial aircrafts

A number of techniques are available for detecting and characterizing defects in aircraft and aerospace structures. These include visual inspection, tap testing, electromagnetics, radiography, thermography, and ultrasonics. However, the currently available methods that can be used to nonintrusively assess structural damage and cracks/delamination on aircraft components (such as thermography, coin-tap testing, and water-jet coupled ultrasound imaging,

or squirter) are cumbersome, time consuming, and costly. Squirter, the off-line ultrasonic (US) scanning system that uses water-jets (e.g., Scanmaster-IRT Model DS-2005, and other systems from Mortec, Olympus NDT, and others) are expensive instruments that require the test structure to be unmounted and transferred to a defined location where the sample can be scanned. The transportation process could further damage the component needing additional evaluation. As an Example, the vertical stabilizer of a typical aircraft could take up to three hours to scan with the squirter, not including the time required for disassembly, reassembly, and loss of service. To overcome the limitations of the conventional, rigorous, and time-consuming off-line non-destructive examination of large area structures, *in situ* inspection methods, which do not require the disassembly of the structure, need to be improved. In this dissertation, a conceptual real-time damage detection system based on ultrasonics is developed for assessing the health of composite structural components in scheduled periodic inspections. The technique is applied to detect hidden damage in a woven composite laminate and composite-aluminum honeycomb aircraft structural component using broadband transducers that can be placed at different locations on the surface of the structural components. This approach offers the potential for developing an *in situ* diagnostic/prognostic ultrasound imaging system for determining the location and size of delaminations and disbonds in composite aircraft structures.

Two general approaches to structural health monitoring are currently being pursued by many investigators. One is the global approach in which changes in the vibrational properties of a structure caused by damage are measured and analyzed in an effort to detect and characterize the damage and the other is a local approach whereby changes in the characteristics of ultrasonic waves propagating across existing defects or created by emerging defects are measured and analyzed to detect and characterize them [4-12]. Many of the techniques are based on the fact

that the dynamical response of a structure to time dependent loads can be measured accurately, that the response changes with the initiation and growth of damage and that careful model based analysis of the measured data on a continuing basis can provide detailed information on the location and severity of the damage. In this dissertation the wave propagation approach along with a novel technique based on a "damage index" is introduced and used to detect impact damage in a woven composite panel.

In order to develop an efficient and reliable damage detection and monitoring system using ultrasonic transducers, it is necessary to have a clear understanding of the quantitative nature of ultrasonic waves that can be transmitted in composite structures with and without damage. The general features of elastic waves that can be transmitted in isotropic and anisotropic solids have been studied in great detail over the past several decades [13-14]. These studies were motivated, in part, by the need to understand the nature of ultrasonic waves that can be transmitted in structural components [15-17]. In contrast, the literature on the response of anisotropic and multilayered composite plates to buried or surface sources that are representative of impact or fatigue damage is relatively sparse.

The exact solution of three-dimensional problems consisting of multilayered, angle-ply laminates of finite thickness and large lateral dimensions subjected to various types of surface loads, has been given in [18-27]. In these papers, the response problem was formulated using triple integral transforms involving one in time and two in space, leading to an exact representation of the elastodynamic field in the transformed frequency-wavenumber domain. The inversion of the transforms required numerical evaluation of a double wavenumber integral followed by frequency inversion using the fast Fourier transform (FFT) algorithm. The main computational effort in this approach involves the accurate evaluation of the double wavenumber

integrals. The evaluation of this integral is computationally intensive due to the presence of singularities and the highly oscillatory nature of the integrands at higher frequencies and large distances between the field and source points.

Approximate thin-plate theories, such as the classical plate theory (C.P.T) under Kirchoff-Love kinematic assumption, and shear deformation plate theory (S.D.P.T) or Mindlin theory, have been developed to obtain the analytical solution to a variety of problems involving the dynamic response of thin isotropic and anisotropic plates [28, 30]. A comprehensive review of recent research on guided waves in composite plates and their use in nondestructive material characterization can be found in [29].

The finite element method (FEM) is also a versatile tool to analyze this class of problems and a dynamic finite element code has been developed for the calculation of acoustic emission (AE) waveforms in isotropic and anisotropic plates [31-32]. This code has been validated with both experimental measurements and analytical predictions for a variety of source conditions and plate dimensions in isotropic materials. Although the FEM can handle complex geometries and has the capability to accommodate reflections from the lateral boundaries, it is computationally much more intensive than the analytical methods discussed above.

As indicated earlier, this research involves NDE and health monitoring of a relatively thin woven composite laminate and a thick layered plate consisting of an aluminum honeycomb core bonded to two woven composite face sheets. The objective is to develop reliable and efficient defects monitoring systems in the structures using ultrasonic guided Lamb type waves. The guided waves are selected as probes due to their ability to propagate large distances across the plate and their strong sensitivity to the presence of crack-like defects in their propagation path. A good understanding of the characteristics of the waves as they propagate across the plate in

absence and presence of defects is a prerequisite to the development of a reliable monitoring system for the structure. Almost all of the wave propagation studies mentioned above involve angle-ply laminates consisting of a stack of unidirectional fiber reinforced materials with different orientations. In the theoretical models, each ply is assumed to be transversely isotropic with its symmetry axis on a plane parallel to the surface of the laminate. This homogenized model of the ply has been shown to be adequate when the wavelengths are large compared to the ply thickness which is usually less than 10 μm. A reasonable homogenized model for the material of the woven composite plate is also transversely isotropic but with its symmetry axis normal to the plate surface. This is also true for the honeycomb material where the symmetry axis is parallel to the axis of the cells of the core. Thus the theoretical problem that is considered for the woven composite panel here is a homogeneous plate composed of a transversely isotropic material with symmetry axis normal to its surface. The model of the honeycomb composite is three-layered transversely isotropic plate composed of the honeycomb core bonded to the composite face sheets. The theoretical solutions of these problems are not available in the literature and are provided here using analytical and numerical (Finite Element) methods. The elastic constants of the two materials (woven composite and aluminum honeycomb core) are determined form mixture typed theories, and from destructive and ultrasonic nondestructive experiments. The validity of the assumption of transverse isotropy in the frequency range of are demonstrated from experiments.

Due to the complex geometry and material properties it is difficult if not impossible to predict the quantitative properties of guided waves in these structures using purely analytical approaches. Based on simplified model, the dynamic behavior of the honeycomb sandwich was investigated. The material properties of honeycomb structure were obtained from the simplified

model proposed by Gibson and Ashby [33]. Several methods exist for determining the effective properties of plane weave lamina and unidirectional cross-ply laminates. It is more difficult to determine the effective properties of twill woven lamina. Once we determine plane weave and cross-ply properties, the properties of the 2/2 twill lamina can be bounded by these two cases. The numerical method described by Naik [34] can be used to estimate the properties of the plane weave lamina, which is relatively simple compared to other methods (e.g. finite element methods), but still retains relatively high accuracy. The material properties of the cross-ply laminate were determined using a modified Hashin model [35]. A simple rule of mixture method described by Whitcomb and Xiadong [36] was used to estimate the material properties of the 2/2 twill lamina.

The dissertation is composed of seven chapters. Chapter 1 contains introduction and literature review. In chapter 2 the elastic properties of the composite and the honeycomb are determined using a combination of mechanical and ultrasonic tests. In chapter 3 propagation characteristics of ultrasonic waves in composite structures understood theoretically, experimentally, and numerically (finite element method). The characterization consists of obtaining dispersion curves, proving the transverse isotropy, and attenuation in both the face sheet and sandwich structure. Guided wave propagation as well as determination of impact damage in the composite panel using guided wave and damage index algorithm is discussed in Chapter 4. In chapter 5 and 6 detection of damage both experimentally and numerically in a thick aluminum plate as well as sandwich structure is discussed. Finally, concluding remarks are discussed in Chapter 7.

Chapter 2 DETERMINATION OF MATERIAL PROPERTIES OF THE SANDWICH PANEL

The sandwich panel of interest is composed of two carbon-epoxy face sheets with an aluminum honeycomb core with hexagonal cells. The face sheet consists of 8 layers of 2/2 twill woven carbon fiber with a $[0°/45°/0°/45°]_s$ stacking sequence. The effective elastic properties will be used for both the face sheet and the core material in analyzing the propagation of guided waves in the panel. The justification for this idealization will be provided later.

2.1 Effective Properties of the Composite Face Sheets Using Theoretical Approach

The 2/2 twill-woven carbon fabric, a balanced weave, has 12 yarns-per-inch in both the warp and fill directions. Each lamina is 0.221 mm thick with a density of 0.0197 g/cm^3, and each yarn is composed of 3000 strands of T300 carbon fibers and the matrix that binds the material is Unibond 1070 epoxy. The properties of these materials are listed in Table 2-1.

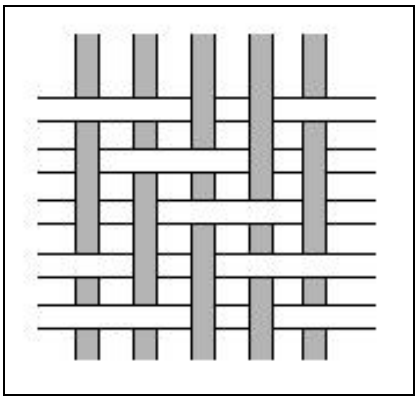

Figure 2-1: 2/2 Twill Weave

Table 2-1: Elastic properties of T-300 Carbon Fibers and Epoxy (from Naik and Ganesh [37])

$E_{11}^{f,m}$ (GPa)	$E_{22}^{f,m}$ (GPa)	$E_{33}^{f,m}$ (GPa)	$G_{12}^{f,m}$ (GPa)	$G_{13}^{f,m}$ (GPa)	$G_{23}^{f,m}$ (GPa)	$\nu_{12}^{f,m}$	$\nu_{13}^{f,m}$	$\nu_{23}^{f,m}$
230	40	40	24	24	13.4	0.23	0.23	0.26
3.5	3.5	3.5	1.3	1.3	1.3	0.35	0.35	0.35

Several methods exist for determining the effective properties of the plane weave lamina and the unidirectional cross-ply laminates, although it is more difficult to determine the effective properties of twill woven lamina. Once we determine plane weave and cross-ply properties, the properties of the 2/2 twill lamina can be bounded by these twos. The numerical method described by Naik [34], which is relatively simple compared to other methods (e.g. finite element methods), are used here to estimate the properties of the plane weave. The cross-ply material properties were determined using the modified Hashin model [35]. A simple rule of mixture method, described by Whitcomb and Xiadong [36], can be used to estimate the effective material properties of the 2/2 twill lamina from the following five equations:

$$\frac{1}{E_{11}} = \frac{V_w}{E_{11}^w} + \frac{V_s}{E_{11}^s} \tag{2.1}$$

$$E_{33} = E_{33}^w V_w + E_{33}^s V_s \tag{2.2}$$

$$\nu_{13} = \left(\frac{V_w}{E_{11}^w} \nu_{13}^w + \frac{V_s}{E_{11}^s} \nu_{13}^s \right) \Bigg/ \left(\frac{V_w}{E_{11}^w} + \frac{V_s}{E_{11}^s} \right); \quad \nu_{12} = \nu_{12}^w V_w + \nu_{12}^w V \tag{2.3}$$

$$G_{13} = G_{13}^w V_w + G_{13}^w V_s \tag{2.4}$$

$$G_{12} = G_{12}^w \tag{2.5}$$

where V_w is the volume fraction of the wavy region and V_s is the volume fraction of the straight region. For the 2/2 twill weave both V_w and V_s are about 0.5. The superscript, w, indicates

properties of the wavy region, which are modeled using the properties for a plane weave lamina and the superscript, s, indicates properties for the straight regions, which are modeled using the properties of the cross-ply laminate. Table 2-2 give the input parameters required for estimating the effective properties of the plane weave and cross-ply laminae.

Table 2-2: Input parameters for estimating effective properties of plane weave and cross-ply laminae.

Packing density of the yarn, p_d	0.65
Yarn spacing, a	2.032 mm
Filament diameter, d_f	0.007 mm
Number of filaments in the yarn, N	3000
Fiber volume fraction	V_f

Effective properties of unidirectional lamina and laminate

The effective properties of the unidirectional lamina are found using the modified Hashin method [35] and those for [0/90] cross-ply laminate are determined using classical laminate theory (CLT) for the in-plane properties. Its out-of-plane properties remain the same as that for the individual lamina. To determine the in-plane properties based on CLT, we need to use the following steps (Jones [38]):

(1) Determine the reduced stiffness's (Q_{ij}) for a plane stress state in the 1-2 plane for each lamina from the relation

$$Q_{ij} = \begin{bmatrix} Q_{11} & Q_{12} & 0 \\ Q_{12} & Q_{22} & 0 \\ 0 & 0 & Q_{66} \end{bmatrix} \qquad (2.6)$$

where,

$$Q_{11} = \frac{E_1}{1-\nu_{12}\nu_{21}}, Q_{22} = \frac{E_2}{1-\nu_{12}\nu_{21}}, Q_{12} = \frac{\nu_{12}E_2}{1-\nu_{12}\nu_{21}} = \frac{\nu_{21}E_1}{1-\nu_{12}\nu_{21}}, Q_{66} = G_{12}$$

$$\frac{\nu_{12}}{E_1} = \frac{\nu_{21}}{E_2}$$

(2) Transform the lamina properties to the laminate coordinates.

$$\left[\bar{\mathbf{Q}}\right] = \left[\mathbf{T}\right]^{-1}\left[\mathbf{Q}\right]\left[\mathbf{T}\right]^{-T} \tag{2.7}$$

where,

$$\left[\mathbf{T}\right] = \begin{bmatrix} \cos^2\theta & \sin^2\theta & 2\sin\theta\cos\theta \\ \sin^2\theta & \cos^2\theta & -2\sin\theta\cos\theta \\ -\sin\theta\cos\theta & \sin\theta\cos\theta & \cos^2\theta - \sin^2\theta \end{bmatrix}$$

And θ is the orientation of the lamina. In the cross-ply laminate $\theta = \pm 90^\circ$

(3) Determine the extensional stiffness, A_{ij}.

$$A_{ij} = \sum_{k=1}^{N}\left(\bar{Q}_{ij}\right)_k\left(z_k - z_{k-1}\right) \tag{2.8}$$

For a [0/90] cross-ply with thickness *h* for each lamina, it can be shown that:

$$A_{ij} = \left(\left(\bar{Q}_{ij}\right)^{0^\circ} + \left(\bar{Q}_{ij}\right)^{90^\circ}\right) \times h \tag{2.9}$$

(4) Invert the A_{ij} matrix to find the extensional compliance, A^*_{ij}.

$$A^*_{ij} = \begin{bmatrix} A_{11} & A_{12} & A_{16} \\ A_{12} & A_{22} & A_{26} \\ A_{16} & A_{26} & A_{66} \end{bmatrix}^{-1} = \begin{bmatrix} A^*_{11} & A^*_{12} & A^*_{16} \\ A^*_{12} & A^*_{22} & A^*_{26} \\ A^*_{16} & A^*_{26} & A^*_{66} \end{bmatrix} \tag{2.10}$$

(5) Using the extensional compliance for the laminate, the in-plane laminate engineering constants can be defines as:

$$E_{11} = \frac{1}{t}\frac{1}{A_{11}^*}, E_{22} = \frac{1}{t}\frac{1}{A_{22}^*}, G_{12} = \frac{1}{t}\frac{1}{A_{66}^*}, \nu_{12} = \frac{A_{12}^*}{A_{22}^*} \qquad (2.11)$$

where, *t* is the thickness of the laminate.

To find the elastic properties of a [0°/45°/0°/45°/45°/0°/45°/0°] stacking sequence we need to follow the same approach as above. The only difference will be extensional stiffness, A_{ij} matrix, where:

$$A_{ij} = \left(\left(\bar{Q}_{ij}\right)^{0^\circ} + \left(\bar{Q}_{ij}\right)^{45^\circ} \right) \times 4h \qquad (2.12)$$

Effective properties of plane weave lamina and laminate

A program called "Micromechanics and Laminate Analysis of Textile Fabric Composites" (Shivakumar and Challa [39]) was used to compute the effective properties of the plane weave lamina and 8-layer plane weave with a $[0°/45°/0°/45°]_s$ stacking sequence. The input values used are listed in Tables 2-1 and 2-2.

Plots for the effective properties of plane weave, 2/2 twill weave, the unidirectional lamina with T300 carbon fiber and epoxy matrix, the 8-layer plane weave, 2/2 twill, and unidirectional cross-ply laminates with a $[0°/45°/0°/45°]_s$ stacking sequence are shown in Figures 2-2 and 2-3.

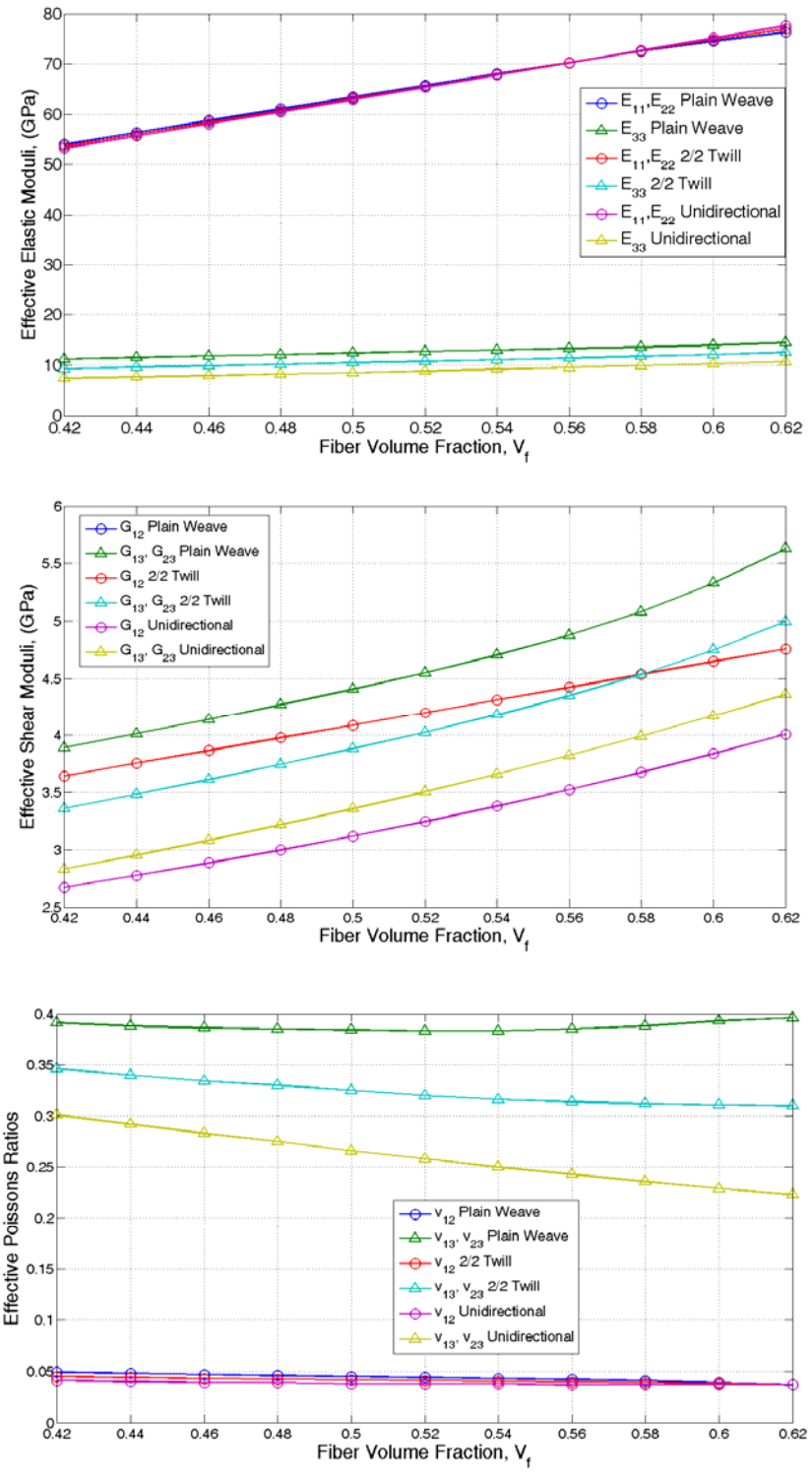

Figure 2-2: Estimated effective elastic constants of plane-weave, 2/2 twill weave, and unidirectional cross-ply lamina with T300 carbon fiber and epoxy matrix.

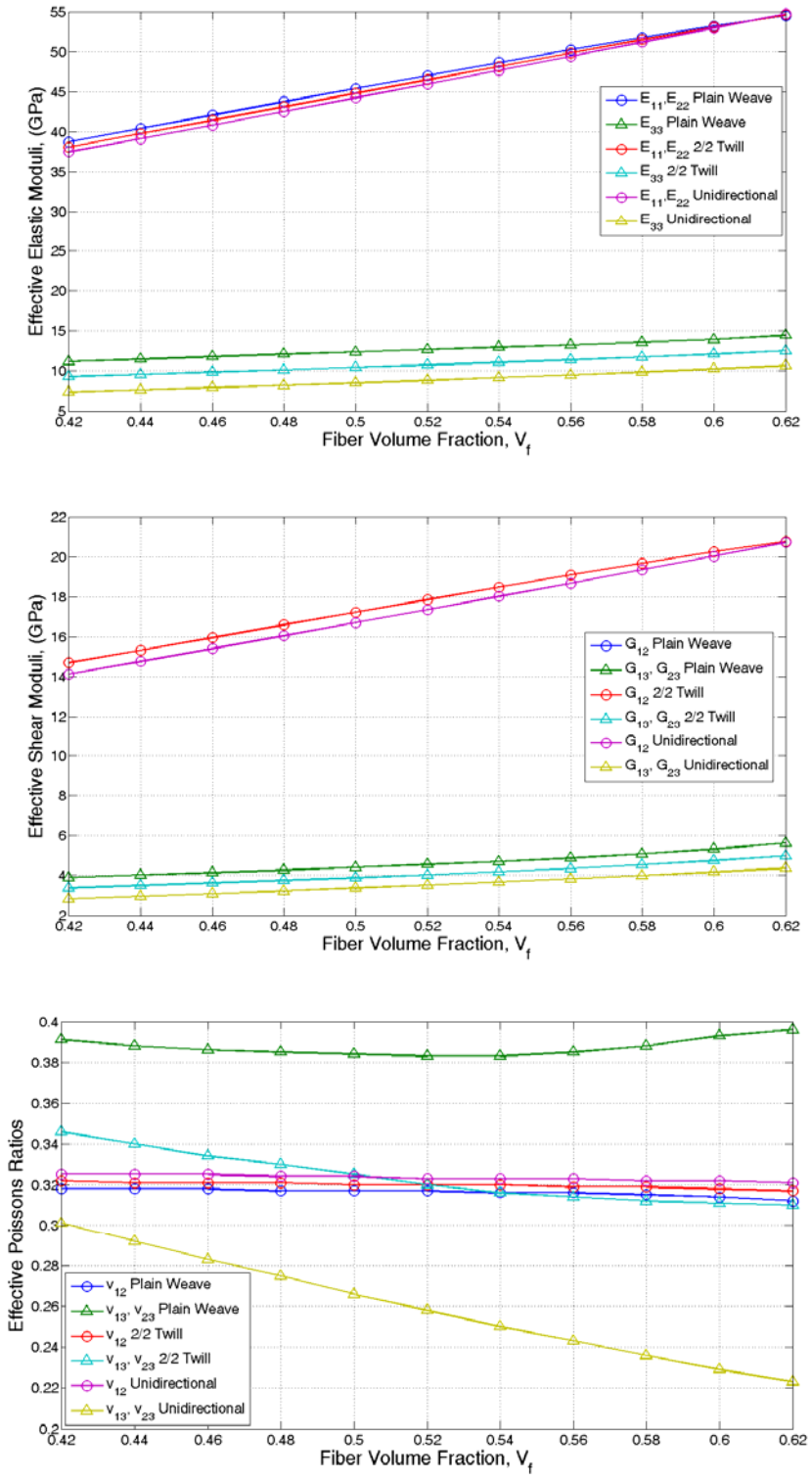

Figure 2-3: Same as in Figure 2-2 for 8 layer plain weave, 2/2 twill, and unidirectional cross-ply laminate with a [0°/45°/0°/45°/45°/0°/45°/0°] stacking sequence.

2.2 Effective Properties of Composite Face sheets Using Experimental Approach

Some of the material constants were also determined experimentally for the composite face sheet to validate the above estimates. The constant E_{22} was determined by applying a tensile load in the x_2 direction and measuring the extension in the same direction using an extensometer. The stress-strain plot obtained experimentally is shown in Figure 2-4. From the data obtained experimentally, the Young's Modulus E_{22} is found to be 38.8 GPa.

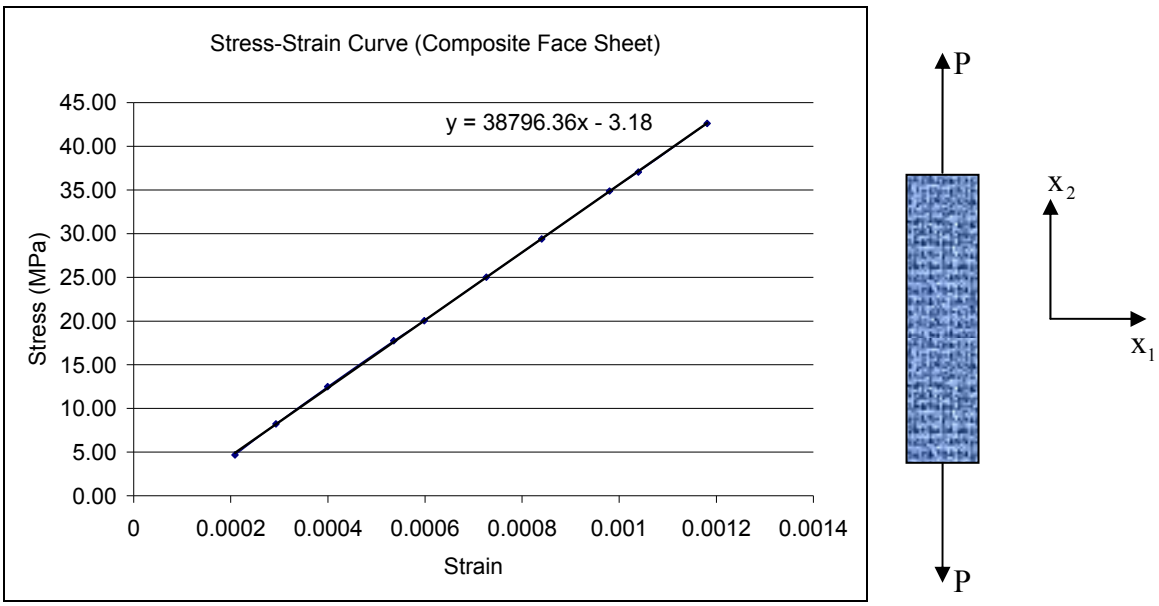

Figure 2-4: Stress-Strain Plot for the Composite Face Sheet

The Poisson ratio in the 1-2 plane (ν_{12}) was determined by applying tensile load in the x_2 direction and measuring strains in both the x_1 and x_2 directions using strain gauges mounted on the test sample. From the experimental data, $\nu_{12} = 0.3137$.

2.3 Effective Properties of Composite Face sheets Using Wave Propagation Approach

The shear modulus G_{23} and the elastic constant E_{33} for the composite face sheet were determined from the following equations (Mal and Singh [40]), using wave propagation experiments

$$G_{23} = v_{23}^2 \rho \qquad (2.13)$$

$$E_{33} = \frac{\rho E_{22}(1-\nu_{12})v_{11}^2}{E_{22}(1-\nu_{12}) + 2\rho v_{13}^2 v_{11}^2} \qquad (2.14)$$

where v_{11} and v_{23} are the longitudinal and shear wave velocities respectively of wave propagation along the thickness direction of the composite face sheet. From Equation (2.14) E_{33} can be calculated by assuming a value for ν_{13} from Figure 2-3 for V_f = 0.5. The measured velocities using through transmission of ultrasonic waves were v_{11} = 2880 m/s, v_{23} = 1517 m/s. These results are nearly independent of the frequency of the ultrasonic waves. For ρ = 1276.3 kg/m^3, E_{22} = 38.8 GPa, $\nu_{12} = 0.3137$, and $\nu_{13} = 0.324$ Equations (2.13) and (2.14) give G_{23} = 2.93714 GPa and E_{33} = 9.77 GPa. The estimated effective properties of the composite face sheet obtained from the mixture type theory and destructive and ultrasonic nondestructive experiments is given in Table 2-3.

Table 2-3: The estimated effective properties of the Twill woven carbon fiber composite using mixture typed theory for $V_f = 0.5$.

	E_{11}, E_{22} (GPa)	E_{33} (GPa)	$G_{12} = \frac{E_{11}}{2(1+\nu_{13})}$ (GPa)	G_{13}, G_{23} (GPa)	ν_{12}, ν_{21}	ν_{31}, ν_{32} $= \frac{E_{33}}{E_{11}}\nu_{13}$	ν_{13}, ν_{23}
Experiment	38.8	9.77	14.7675	2.937	0.3137	0.081585	0.324
Theroy	44.795	10.753	17.230	3.881	0.320	0.07778	0.324

It should be noted that the experimentally determined values of the effective properties are significantly different from those from the theory given in Table 2-3. The experimental value in Table 2-3 will be used in calculating the wave propagation characteristics in subsequent sections.

2.4 Effective Properties of the Honeycomb Core

The honeycomb core has a regular hexagonal cell structure made of 5052 aluminum approximately 12 mm width. The geometry of the hexagonal cell used in determining the effective material properties of the core is shown in Figure 2-5. A complicating factor in determining the properties of the core material resulted from the manufacturing process shown in Figure 2-6. A sheet of aluminum is crimped and the adhesive is applied to the flat faces. These sheets are then stacked to create the honeycomb geometry. The result of this process is two walls in each unit cell which have a double wall thickness. This complication changes the shear moduli and density compared to single thickness walls but does not have a significant effect on the elastic moduli. The approximate expressions for the elastic properties of the regular hexagonal honeycomb core are given in Equations (2.15 and 2.16) (Gibson and Ashby[33]).

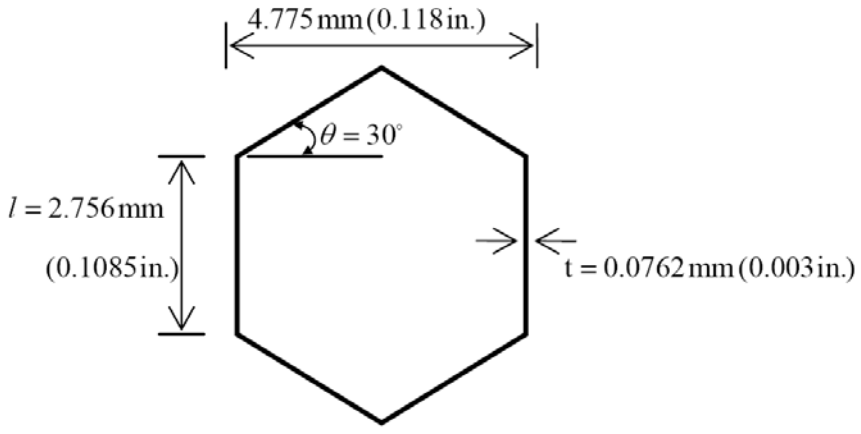

Figure 2-5: Regular hexagonal honeycomb unit cell geometry.

Table 2-4: Properties of 5052 Aluminum material properties.

$E(GPa)$	$G(GPa)$	ν	$\rho(g/cm^3)$
70.3	25.9	0.33	2.68

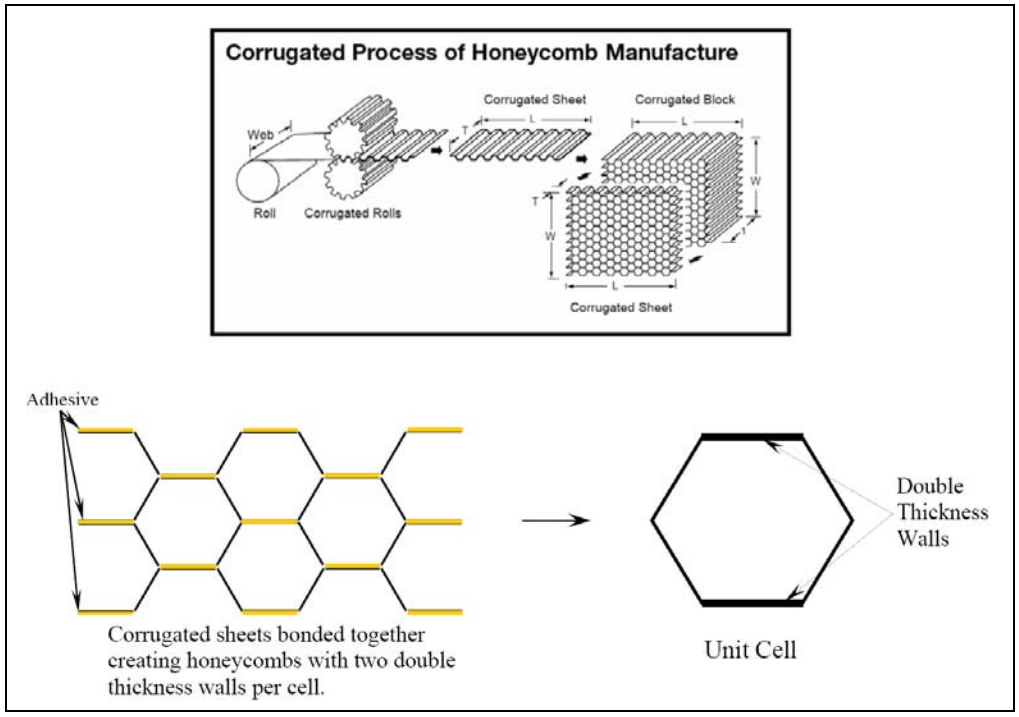

Figure 2-6: Honeycomb core manufacturing process showing double wall thickness due to corrugated sheet bonding.

Equation (2.15) gives the expression for the relative density of the double wall honeycomb core (ρ^*) to the solid material (ρ_s). In this expression, t is the wall thickness of the honeycomb cell and *l* is the length of the edge of the cell.

$$\frac{\rho^*}{\rho_s} = \frac{8}{3\sqrt{3}}\frac{t}{l} = 0.042568 \qquad (2.15)$$

Equations (2.16) give expressions for the elastic. As can be seen, the in-plane elastic muduli $E_i^*, G_{ij}^*, \text{and } \nu_{ij}^*$ relative to their values in the monolithic aluminum, $E_i^s, G_{ij}^s, \text{and } \nu_{ij}^s$:

$$\frac{E_1^*}{E_s} = \frac{E_2^*}{E_s} = \frac{4}{\sqrt{3}}\left(\frac{t}{l}\right)^3 = 4.88\times10^{-5} \tag{2.16a}$$

$$\frac{E_3^*}{E_s} = \frac{2}{\sqrt{3}}\frac{t}{l} = \frac{\rho^*}{\rho_s} = 0.042568 \tag{2.16b}$$

$$\nu_{12}^* = \nu_{21}^* = 1 \tag{2.16c}$$

$$\nu_{13}^* = \frac{E_1^*}{E_3^*}\nu_s, \nu_{23}^* = \frac{E_2^*}{E_3^*}\nu_s \tag{2.16d}$$

$$\nu_{31}^* = \nu_{32}^* = \nu_s \tag{2.16e}$$

$$\frac{G_{12}^*}{E_s} = \frac{1}{\sqrt{3}}\left(\frac{t}{l}\right)^3 = 1.22\times10^{-5} \tag{2.16f}$$

$$\frac{G_{13}^*}{G_s} = \frac{G_{23}^*}{G_s} = \frac{1}{\sqrt{3}}\left(\frac{t}{l}\right) = 0.015963 \tag{2.16g}$$

It can be seen that as expected the in-plane moduli are much smaller than the corresponding out-of-plane moduli. Using equation (2.16), dimensions of the unit cell (Figure 2-5) and the material properties of 5052 aluminum (Table 2-4) in equation (2.15 and 2.16) the estimated density and elastic properties of the honeycomb core are calculated and given in Table 2-5.

Table 2-5: Estimated effective properties for a regular hexagonal honeycomb core.

E_{11} (GPa)	E_{22} (GPa)	E_{33} (GPa)	G_{12} (GPa)	G_{13} (GPa)	G_{23} (GPa)	ν_{12}, ν_{21}	ν_{31}, ν_{32}	ν_{13}, ν_{23}	ρ (kg/m^3)
3.43×10^{-3}	3.43×10^{-3}	2.99	0.86×10^{-3}	0.413	0.413	1.00	0.33	3.79×10^{-4}	114.1

Chapter 3 GUIDED WAVE PROPAGATION IN COMPOSITE STRUCTURES

The degradation of composite materials and composite structures can be assessed using ultrasonic nondestructive evaluation (NDE) techniques. For successful application of these techniques to locate and estimate the severity of the damage, it is extremely important to understand the propagation characteristics of ultrasonic waves in these structures. Wave propagation in composites is extremely complex due to its material inhomogeneity and anisotropy, where characteristics of the waves depend on the laminate layup, direction of wave propagation, frequency, and interface conditions. When elastic waves are generated by surface sources in a plate, they experience repeated reflections at the top and bottom surfaces alternately. The mutual interference of the reflected waves results in propagation guided by the plate surfaces. The guided waves are dispersive, i.e., their velocity of propagation along the plate is dependent on the frequency and the thickness of the plate. The dispersion relation for a homogeneous elastic isotropic plate was first derived by Lamb [41]. Lamb waves are guided waves that travel parallel to the surface of a homogeneous plate of finite thickness, infinite lateral dimensions, and traction-free boundaries. Since lamb waves are guided and stay confined inside the plate, they can travel over long distances, allowing inspection of a large area in plate-like structures with limited number of sensors. Guided waves are classified in to three types in isotropic structures according to their polarization or the direction of displacement vector. The one polarized in the plane perpendicular to the plate, say in the x-y plane shown in Figure 3-1, are called symmetric (or extensional, S) waves and anti-symmetric (or flexural, A) waves, and the one polarized in the plane of the plate are called shear horizontal (SH) waves.

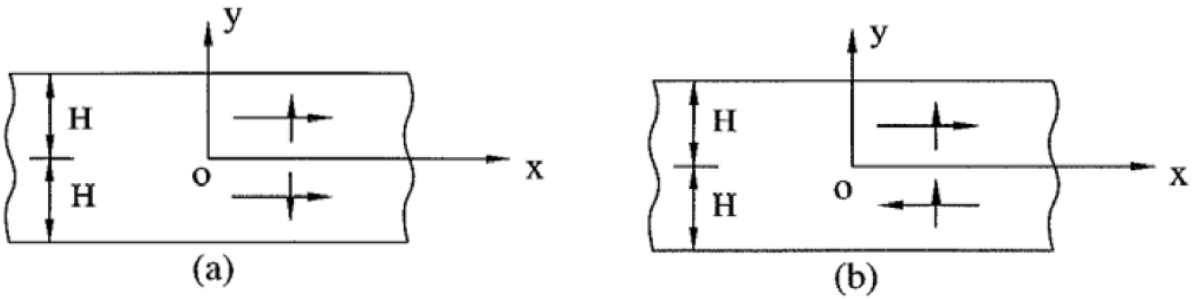

Figure 3-1: Guided waves in a homogeneous plate: (a) symmetric motion and (b) antisymmetric motion [40]

3.1 Dispersion Relation for an Elastic Isotropic Plate

For a homogeneous isotropic elastic plate under plane strain conditions for *anti-symmetric* motion of the plate, the dispersion equation is of the following form [40]

$$\left(2k^2 - k_2^2\right)^2 \sinh\left(\eta_1 H\right)\cosh\left(\eta_2 H\right) - 4k^2\eta_1\eta_2 \sinh\left(\eta_2 H\right)\cosh\left(\eta_1 H\right) = 0 \qquad (3.1)$$

where,

$$\eta_j = \sqrt{k^2 - k_j^2}\ ,\ k = \frac{\omega}{c}\ , k_j = \frac{\omega}{c_j}, j = 1,2 \qquad (3.2)$$

The solution of equation (3.1) gives the wave number k, from which the wave speed c can be calculated using the relation $k = \frac{\omega}{c}$. Since equation (3.1) is a transcendental equation and c is a function of ω. The waves are then called dispersive, and the equation giving c as a function of ω is called dispersion equation. If the frequency is small, an approximate solution of the dispersion equation can be found as:

$$\frac{c}{c_2} = \left[\frac{4}{3}\left(1 - \left(\frac{c_2}{c_1}\right)^2\right)\right]^{1/4}\left(\frac{\omega H}{c_2}\right)^{1/2}$$

At high frequencies the dispersion equation reduces to Rayleigh wave equation.

$$\left(2k^2 - k_2^2\right)^2 - 4k^2\eta_1\eta_2 = 0 \tag{3.3}$$

For *symmetric* motion of the plate the dispersion equation is of the following form [34],

$$\left(2k^2 - k_2^2\right)^2 \sinh\left(\eta_2 H\right)\cosh\left(\eta_1 H\right) - 4k^2\eta_1\eta_2 \sinh\left(\eta_1 H\right)\cosh\left(\eta_2 H\right) = 0 \tag{3.4}$$

In the limit of zero frequency, the phase velocity c tends to a finite value c_p, given by

$$c_p = 2c_2\sqrt{1 - \left(\frac{c_2}{c_1}\right)^2} \tag{3.5}$$

At low frequencies, the symmetric Lamb waves are called "*extensional waves*" and are designated as the S_o mode; the anti-symmetric waves are called "*flexural waves*" and are referred to as the A_o mode. At intermediate frequencies, the dispersion equation must be solved numerically. The graphical results shown in Figure 3-2, called *dispersion curves*.

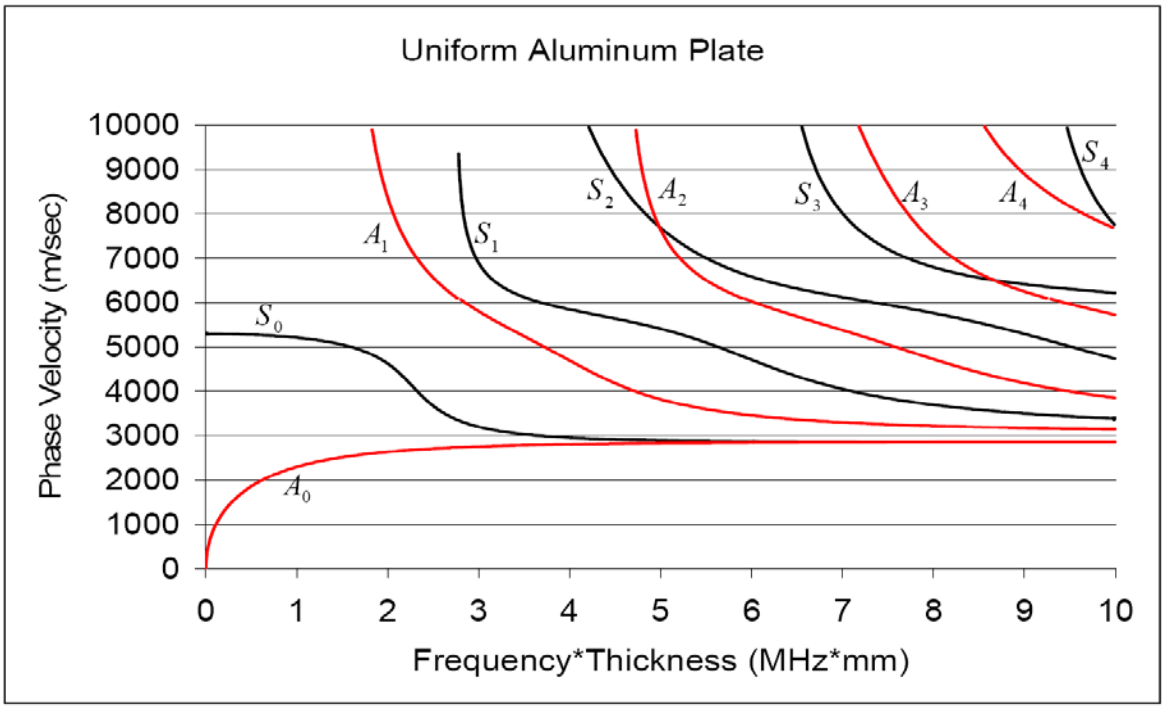

Figure 3-2: Dispersion curves for Lamb waves in an aluminum plate.

3.2 Dispersion Relation for an Elastic Transversely Isotropic Plate

As indicated in Chapter 2, the composite plate of interest here is transversely isotropic with its symmetric axis normal to the plate. In this section the dispersion properties of lamb waves in a transversely isotropic plate with symmetry axis along x_3-axis (figure 3-3) are determined. Since the dispersion curves are strongly dependent on some of the elastic constants of the material, they can be used to determine these constants as a further check on the validity of the estimated values in Table 2-3 obtained experimentally.

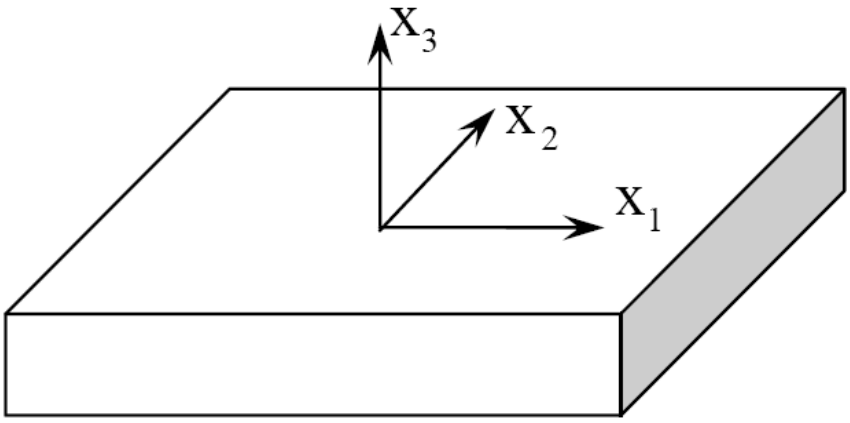

Figure 3-3: Composite Layer

For a homogeneous and transversely isotropic material with 1-2 plane as the plane of isotropy, the stress components σ_{ij} can be expressed in terms of the displacement components u_i by the following equations:

$$\begin{Bmatrix}\sigma_{11}\\ \sigma_{22}\\ \sigma_{33}\\ \sigma_{23}\\ \sigma_{31}\\ \sigma_{12}\end{Bmatrix}=\begin{bmatrix} c_{11} & c_{12} & c_{13} & 0 & 0 & 0\\ c_{12} & c_{22} & c_{13} & 0 & 0 & 0\\ c_{13} & c_{13} & c_{33} & 0 & 0 & 0\\ 0 & 0 & 0 & c_{44} & 0 & 0\\ 0 & 0 & 0 & 0 & c_{44} & 0\\ 0 & 0 & 0 & 0 & 0 & \frac{1}{2}(c_{11}-c_{12}) \end{bmatrix}\begin{Bmatrix} u_{1,1}\\ u_{2,2}\\ u_{3,3}\\ u_{2,3}+u_{3,2}\\ u_{1,3}+u_{3,1}\\ u_{1,2}+u_{2,1}\end{Bmatrix} \tag{3.6}$$

The equations of motion with no body forces are,

$$\begin{aligned}\frac{\partial\sigma_{11}}{\partial x_1}+\frac{\partial\sigma_{12}}{\partial x_2}+\frac{\partial\sigma_{13}}{\partial x_3}&=\rho\frac{\partial^2 u_1}{\partial t^2}\\ \frac{\partial\sigma_{12}}{\partial x_1}+\frac{\partial\sigma_{22}}{\partial x_2}+\frac{\partial\sigma_{23}}{\partial x_3}&=\rho\frac{\partial^2 u_2}{\partial t^2}\\ \frac{\partial\sigma_{13}}{\partial x_1}+\frac{\partial\sigma_{23}}{\partial x_2}+\frac{\partial\sigma_{33}}{\partial x_3}&=\rho\frac{\partial^2 u_3}{\partial t^2}\end{aligned} \tag{3.7}$$

In order to determine the propagation characteristics of the guided waves we consider the plane strain model shown in Figure 3-4.

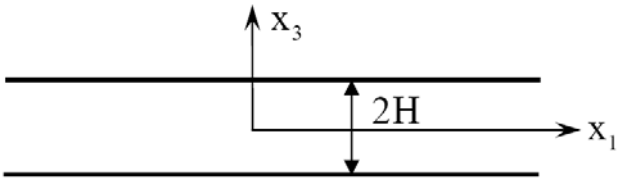

Figure 3-4: A plane strain model of the transversely isotropic plate.

$$u_2=0 \text{ and } \frac{\partial}{\partial x_2}=0$$

Then the stress displacement relations and equations of motion can be rewritten as,

$$\sigma_{11}=c_{11}\frac{\partial u_1}{\partial x_1}+c_{13}\frac{\partial u_3}{\partial x_3},\sigma_{33}=c_{13}\frac{\partial u_1}{\partial x_1}+c_{33}\frac{\partial u_3}{\partial x_3},\sigma_{13}=c_{44}\left[\frac{\partial u_1}{\partial x_3}+\frac{\partial u_3}{\partial x_1}\right] \tag{3.8}$$

$$\frac{\partial \sigma_{11}}{\partial x_1}+\frac{\partial \sigma_{13}}{\partial x_3}-\rho\frac{\partial^2 u_1}{\partial t^2}=0,\frac{\partial \sigma_{13}}{\partial x_1}+\frac{\partial \sigma_{33}}{\partial x_3}-\rho\frac{\partial^2 u_3}{\partial t^2}=0 \qquad (3.9)$$

The displacement components associated with the lamb waves can be expressed in the form:

$$u_\alpha = A_\alpha e^{i(kx_1-\omega t)+\eta x_3}, \qquad \alpha = 1,3 \qquad (3.10)$$

where η is a function of ω and c, and A_α are constants.

Inserting equation (3.10) into equation (3.8),

$$\begin{aligned}\sigma_{11} &= \left(ikc_{11}A_1+\eta c_{13}A_3\right)e^{i(kx_1-\omega t)+\eta x_3}\\ \sigma_{13} &= c_{44}\left(\eta A_1+ikA_3\right)e^{i(kx_1-\omega t)+\eta x_3}\\ \sigma_{33} &= \left(ikc_{13}A_1+\eta c_{33}A_3\right)e^{i(kx_1-\omega t)+\eta x_3}\end{aligned} \qquad (3.11)$$

Substituting from equation (3.11) into the equations of motion (3.9) leads to the linear system:

$$\begin{bmatrix}\left(\eta^2 c_{44}+\rho\omega^2-k^2c_{11}\right) & ik\eta\left(c_{13}+c_{44}\right)\\ ik\eta\left(c_{13}+c_{44}\right) & \left(\eta^2 c_{33}+\rho\omega^2-k^2c_{44}\right)\end{bmatrix}\begin{Bmatrix}A_1\\A_3\end{Bmatrix}=\begin{Bmatrix}0\\0\end{Bmatrix} \qquad (3.12)$$

For nontrivial solution of equation (3.12) for A_1 and A_3, η must satisfy the equation

$$\left(\eta^2 c_{44}+\rho\omega^2-k^2c_{11}\right)\left(\eta^2 c_{33}+\rho\omega^2-k^2c_{44}\right)+k^2\eta^2\left(c_{13}+c_{44}\right)^2=0$$

which can be expressed in the form

$$\eta^4+\eta^2k^2\left\{\frac{\rho c^2}{c_{33}}+\frac{\rho c^2}{c_{44}}-\frac{\left(c_{11}c_{33}-c_{13}^2-2c_{13}c_{44}\right)}{c_{33}c_{44}}\right\}+k^4\left(\frac{\rho c^2}{c_{44}}-1\right)\left(\frac{\rho c^2}{c_{33}}-\frac{c_{11}}{c_{33}}\right)=0 \qquad (3.13)$$

Thus

$$\eta_{1.2} = k\sqrt{\frac{-A \pm \sqrt{A^2 - 4B}}{2}}$$

where

$$A = \frac{c^2}{c_{3L}^2} + \frac{c^2}{c_{3T}^2} - \frac{\left(c_{11}c_{33} - c_{13}^2 - 2c_{13}c_{44}\right)}{c_{33}c_{44}},\ B = \left(\frac{c^2}{c_{3T}^2} - 1\right)\left(\frac{c^2}{c_{3L}^2} - \frac{c_{11}}{c_{33}}\right)$$

$$c_{3L} = \sqrt{\frac{c_{33}}{\rho}} \text{ and } c_{3T} = \sqrt{\frac{c_{44}}{\rho}}$$

From equation (3.12), the constants A_1 and A_2 are related through

$$\frac{A_3}{A_1} = \frac{k^2 c_{11} - \rho\omega^2 - \eta^2 c_{44}}{ik\eta\left(c_{13} + c_{44}\right)} \qquad (3.14)$$

For the isotropic case

$c_{11} = c_{33} = \lambda + 2\mu = \rho c_1^2,\ c_{44} = \mu = \rho c_2^2,\ c_{13} = \lambda,\ c_{13} + 2c_{44} = c_{11}$

and the expressions for η_l and η_2 reduce equation (3.2)

3.2.1 Dispersion Relation for the Symmetric Case:

The general solution for the symmetric problem can be expressed in the form

$$u_1\left(x_1, x_3\right) = \left(a_1 \cosh \eta_l x_3 + a_2 \cosh \eta_2 x_3\right) e^{ikx_1}$$
$$u_3\left(x_1, x_3\right) = \left(b_1 \sinh \eta_l x_3 + b_2 \sinh \eta_2 x_3\right) e^{ikx_1} \qquad (3.15)$$

where a_i and b_i are constants to be determined from the boundary conditions.

From equation (3.14)

$$\frac{b_1}{a_1} = \frac{k^2 c_{11} - \rho\omega^2 - \eta_1^2 c_{44}}{ik\eta_1 (c_{13} + c_{44})} = \beta_1$$

$$\frac{b_2}{a_2} = \frac{k^2 c_{11} - \rho\omega^2 - \eta_2^2 c_{44}}{ik\eta_2 (c_{13} + c_{44})} = \beta_2 \qquad (3.16)$$

equations (3.8), (3.15) and (3.16) yield the stress components,

$$\sigma_{13} = c_{44}\left[\frac{\partial u_1}{\partial x_3} + \frac{\partial u_3}{\partial x_1}\right]$$

$$= c_{44}\left[a_1\eta_1 \sinh\eta_1 x_3 + a_2\eta_2 \sinh\eta_2 x_3 + ika_1\beta_1 \sinh\eta_1 x_3 + ika_2\beta_2 \sinh\eta_2 x_3\right] e^{ikx_1}$$

$$= c_{44}\left[a_1\left(\eta_1 + \frac{k^2 c_{11} - \rho\omega^2 - \eta_1^2 c_{44}}{\eta_1 (c_{13} + c_{44})}\right)\sinh\eta_1 x_3 + a_2\left(\eta_2 + \frac{k^2 c_{11} - \rho\omega^2 - \eta_2^2 c_{44}}{\eta_2 (c_{13} + c_{44})}\right)\sinh\eta_2 x_3\right] e^{ikx_1}$$

$$= c_{44}\left[a_1\left(\frac{\eta_1^2 c_{13} + k^2 c_{11} - \rho\omega^2}{\eta_1 (c_{13} + c_{44})}\right)\sinh\eta_1 x_3 + a_2\left(\frac{\eta_2^2 c_{13} + k^2 c_{11} - \rho\omega^2}{\eta_2 (c_{13} + c_{44})}\right)\sinh\eta_2 x_3\right] e^{ikx_1} \qquad (3.17)$$

Similarly

$$\sigma_{13} = c_{44}\left[\frac{\partial u_1}{\partial x_3} + \frac{\partial u_3}{\partial x_1}\right]$$

$$= c_{44}\left[a_1\eta_1 \sinh\eta_1 x_3 + a_2\eta_2 \sinh\eta_2 x_3 + ika_1\beta_1 \sinh\eta_1 x_3 + ika_2\beta_2 \sinh\eta_2 x_3\right] e^{ikx_1}$$

$$= c_{44}\left[a_1\left(\eta_1 + \frac{k^2 c_{11} - \rho\omega^2 - \eta_1^2 c_{44}}{\eta_1 (c_{13} + c_{44})}\right)\sinh\eta_1 x_3 + a_2\left(\eta_2 + \frac{k^2 c_{11} - \rho\omega^2 - \eta_2^2 c_{44}}{\eta_2 (c_{13} + c_{44})}\right)\sinh\eta_2 x_3\right] e^{ikx_1}$$

$$= \left\{\frac{a_1\left[-k^2 c_{13}(c_{13} + c_{44}) - \eta_1 c_{33} c_{44} + (k^2 c_{11} - \rho\omega^2) c_{33}\right]}{ik(c_{13} + c_{44})}\cosh\eta_1 x_3\right.$$

$$\left. + \frac{a_2\left[-k^2 c_{13}(c_{13} + c_{44}) - \eta_2 c_{33} c_{44} + (k^2 c_{11} - \rho\omega^2) c_{33}\right]}{ik(c_{13} + c_{44})}\cosh\eta_2 x_3\right\} e^{ikx_1} \qquad (3.18)$$

The boundary conditions that must be satisfied are $\sigma_{13} = \sigma_{33} = 0$ at $x_3 = H$, which lead to,

$$\begin{bmatrix} P & Q \\ R & S \end{bmatrix} \begin{Bmatrix} a_1 \\ a_2 \end{Bmatrix} = \begin{Bmatrix} 0 \\ 0 \end{Bmatrix} \tag{3.19}$$

where,

$$P = \left(\frac{\eta_1^2 c_{13} + k^2 c_{11} - \rho\omega^2}{\eta_1 (c_{13} + c_{44})} \right) \sinh \eta_1 H$$

$$Q = \left(\frac{\eta_2^2 c_{13} + k^2 c_{11} - \rho\omega^2}{\eta_2 (c_{13} + c_{44})} \right) \sinh \eta_2 H$$

$$R = \frac{\left[-k^2 c_{13} (c_{13} + c_{44}) - \eta_1 c_{33} c_{44} + (k^2 c_{11} - \rho\omega^2) c_{33} \right]}{ik (c_{13} + c_{44})} \cosh \eta_1 H$$

$$S = \frac{\left[-k^2 c_{13} (c_{13} + c_{44}) - \eta_2 c_{33} c_{44} + (k^2 c_{11} - \rho\omega^2) c_{33} \right]}{ik (c_{13} + c_{44})} \cosh \eta_2 H$$

For nontrivial solution of equation (3.19) for a_1 and a_2 the phase velocity and ω must satisfy the transcendental equation.

$$\frac{\left[\eta_1^2 c_{13} + k^2 c_{11} - \rho\omega^2 \right] \left[-k^2 c_{13} (c_{13} + c_{44}) - \eta_2 c_{33} c_{44} + (k^2 c_{11} - \rho\omega^2) c_{33} \right]}{ik \eta_1 (c_{13} + c_{44})^2} \sinh \eta_1 H \cosh \eta_2 H$$

$$= \frac{\left[\eta_2^2 c_{13} + k^2 c_{11} - \rho\omega^2 \right] \left[-k^2 c_{13} (c_{13} + c_{44}) - \eta_1 c_{33} c_{44} + (k^2 c_{11} - \rho\omega^2) c_{33} \right]}{ik \eta_2 (c_{13} + c_{44})^2} \sinh \eta_2 H \cosh \eta_1 H$$

or

$$\frac{(\sinh kA_1 H)(\cosh kA_2 H)}{(\sinh kA_2 H)(\cosh kA_1 H)} = \frac{A_1 \left[A_2^2 - \frac{c_{11}}{c_{13}} \left(\frac{c^2}{c_{1L}^2} - 1 \right) \right] \left[\frac{c_{13}}{c_{33}} \left(\frac{c_{13}}{c_{44}} + 1 \right) + A_1^2 + \frac{c_{11}}{c_{44}} \left(\frac{c^2}{c_{1L}^2} - 1 \right) \right]}{A_2 \left[A_1^2 - \frac{c_{11}}{c_{13}} \left(\frac{c^2}{c_{1L}^2} - 1 \right) \right] \left[\frac{c_{13}}{c_{33}} \left(\frac{c_{13}}{c_{44}} + 1 \right) + A_2^2 + \frac{c_{11}}{c_{44}} \left(\frac{c^2}{c_{1L}^2} - 1 \right) \right]} = \frac{N}{D} \tag{3.20}$$

where,

$$A_1 = \frac{\eta_1}{k} = \sqrt{\frac{-A + \sqrt{A^2 - 4B}}{2}} = i\sqrt{\frac{A - \sqrt{A^2 - 4B}}{2}}$$

$$A_2 = \frac{\eta_2}{k} = \sqrt{\frac{-A - \sqrt{A^2 - 4B}}{2}} = i\sqrt{\frac{A + \sqrt{A^2 - 4B}}{2}}$$

$$A = \frac{c^2}{c_{3L}^2} + \frac{c^2}{c_{3T}^2} - \frac{\left(c_{11}c_{33} - c_{13}^2 - 2c_{13}c_{44}\right)}{c_{33}c_{44}}, B = \left(\frac{c^2}{c_{3L}^2} - \frac{c_{11}}{c_{33}}\right)\left(\frac{c^2}{c_{3T}^2} - 1\right)$$

$$k = \frac{\omega}{c}, c_{1L}^2 = \frac{c_{11}}{\rho}, c_{3L}^2 = \frac{c_{33}}{\rho}, c_{3T}^2 = \frac{c_{44}}{\rho} \qquad (3.21)$$

As $\omega \to 0,$ the equation reduces to:

$$\left(c_{13}A_2^2 - a\right)\left(b + c_{33}c_{44}A_1^2\right) - \left(c_{13}A_1^2 - a\right)\left(b + c_{33}c_{44}A_2^2\right) = 0$$

where

$$a = c_{11}\left(\frac{c^2}{c_{1L}^2} - 1\right),\ b = c_{13}\left(c_{13} + c_{44}\right) + ac_{33}$$

After simplification, this leads to

$$\left(bc_{13} + ac_{33}c_{44}\right)\left(A_1^2 - A_2^2\right) = 0$$

Thus,

$$bc_{13} + ac_{33}c_{44} = 0,\ c = c_{1L}\sqrt{1 - \frac{c_{13}^2}{c_{11}c_{33}}}$$

This reduces to the correct value of $c = c_p$ for the isotropic case $\left(\text{equation } 3.5\right)$:

$$c_p = 2c_2\sqrt{1 - \frac{c_2^2}{c_1^2}}$$

Another solution is given by

$$A_1^2 - A_2^2 = 0, A^2 - 4B = 0$$

which does not have real roots.

In the isotropic case:

$$c_{11} = c_{33} = \lambda + 2\mu = \rho c_1^2,\ c_{44} = \mu = \rho c_2^2,\ c_{13} = \lambda,\ c_{13} + 2c_{44} = c_{11}, c_{1L}^2 = \frac{c_{11}}{\rho} = c_1^2$$

$$\left.\begin{aligned} A_1 &= \frac{\eta_1}{k} = \sqrt{1 - \frac{c^2}{c_1^2}} \\ A_2 &= \frac{\eta_2}{k} = \sqrt{1 - \frac{c^2}{c_2^2}} \end{aligned}\right\} \Rightarrow \frac{A_1}{A_2} = \frac{\eta_1}{\eta_2}$$

It can be shown that equation (3.20) becomes:

$$\frac{(\sinh kA_1H)(\cosh kA_2H)}{(\sinh kA_2H)(\cosh kA_1H)} = \left(\frac{\eta_1}{\eta_2}\right)\frac{\left(2k^2 - k_2^2\right)}{2\eta_1^2}\left(\frac{2k^2 - k_2^2}{2k^2}\right) = \frac{\left(2k^2 - k_2^2\right)^2}{4\eta_1\eta_2 k^2}$$

This is same as equation (3.4) for the isotropic case, confirming the accuracy of equation (3.20)

Equation (3.20) is a transcendental equation which must be solved numerically. The equation has multiple roots corresponding to different modes of the lamb waves. In order to obtain correct numerical solution it is necessary to identify the cutoff frequencies at which the higher modes appear. As in the isotropic case, the cutoff frequencies are obtained in the limiting case. Thus as $c \to \infty,\ D \to 0$ and $\sinh(kA_2H)\cosh(kA_1H) \to 0$. This agrees with the equation for the cutoff frequencies in the symmetric case.

3.2.2 Dispersion Relation for the Anti-symmetric Case:

The general solution for anti-symmetric problem can be expressed in the form:

$$u_1(x_1, x_3) = (a_1 \sinh \eta_1 x_3 + a_2 \sinh \eta_2 x_3)\, e^{ikx_1}$$

$$u_3(x_1, x_3) = (b_1 \cosh \eta_1 x_3 + b_2 \cosh \eta_2 x_3)\, e^{ikx_1} \qquad (3.22)$$

Using a procedure similar to the symmetric case, the dispersion equation can be formed as,

$$\frac{(\sinh kA_2H)(\cosh kA_1H)}{(\sinh kA_1H)(\cosh kA_2H)}=\frac{A_1\left[A_2^2-\frac{c_{11}}{c_{13}}\left(\frac{c^2}{c_{1L}^2}-1\right)\right]\left[\frac{c_{13}}{c_{33}}\left(\frac{c_{13}}{c_{44}}+1\right)+A_1^2+\frac{c_{11}}{c_{44}}\left(\frac{c^2}{c_{1L}^2}-1\right)\right]}{A_2\left[A_1^2-\frac{c_{11}}{c_{13}}\left(\frac{c^2}{c_{1L}^2}-1\right)\right]\left[\frac{c_{13}}{c_{33}}\left(\frac{c_{13}}{c_{44}}+1\right)+A_2^2+\frac{c_{11}}{c_{44}}\left(\frac{c^2}{c_{1L}^2}-1\right)\right]} \qquad (3.23)$$

The solution of the dispersion equations for transversely isotropic case for both symmetric and anti-symmetric cases are presented in Figure 3-5, where the values of c are obtained numerically for a given range of frequencies. The material used is for a 1.78 mm thick 2/2 twill carbon fiber composite plate with properties given in Table 2-3. The five independent stiffness constants of the material are c_{11}, c_{12}, c_{33}, c_{13} and c_{44}. These are related to constants $E_{11}=E_{22}=E_1$, $E_{33}=E_3$, ν_{12}, $\nu_{31}=\nu_{32}$, $G_{23}=G_{13}$ through

$$c_{11}=\frac{E_1(1-\nu_{32}\nu_{23})}{(1+\nu_{12})(1-\nu_{12}-2\nu_{32}\nu_{23})},\ c_{12}=\frac{E_2(\nu_{12}+\nu_{32}\nu_{23})}{(1+\nu_{12})(1-\nu_{12}-2\nu_{32}\nu_{23})},\ c_{33}=\frac{E_3(1-\nu_{12})}{(1-\nu_{12}-2\nu_{32}\nu_{23})},$$

$$c_{13}=\frac{\nu_{23}E_3}{(1-\nu_{12}-2\nu_{32}\nu_{23})},\ c_{55}=G_{13}$$

(Note: $G_{12}=E_1/[2(1+\nu_{12})]$ and $\nu_{13}=\nu_{23}=E_2\upsilon_{32}/E_3$)

The stiffness constants are given in Table 3-1.

Table 3-1: Stiffness constants of the woven composite plate.

c_{11} (GPa)	c_{12} (GPa)	c_{33} (GPa)	c_{13} (GPa)	c_{44} (GPa)
45.37	15.83	9.42	4.69	2.94

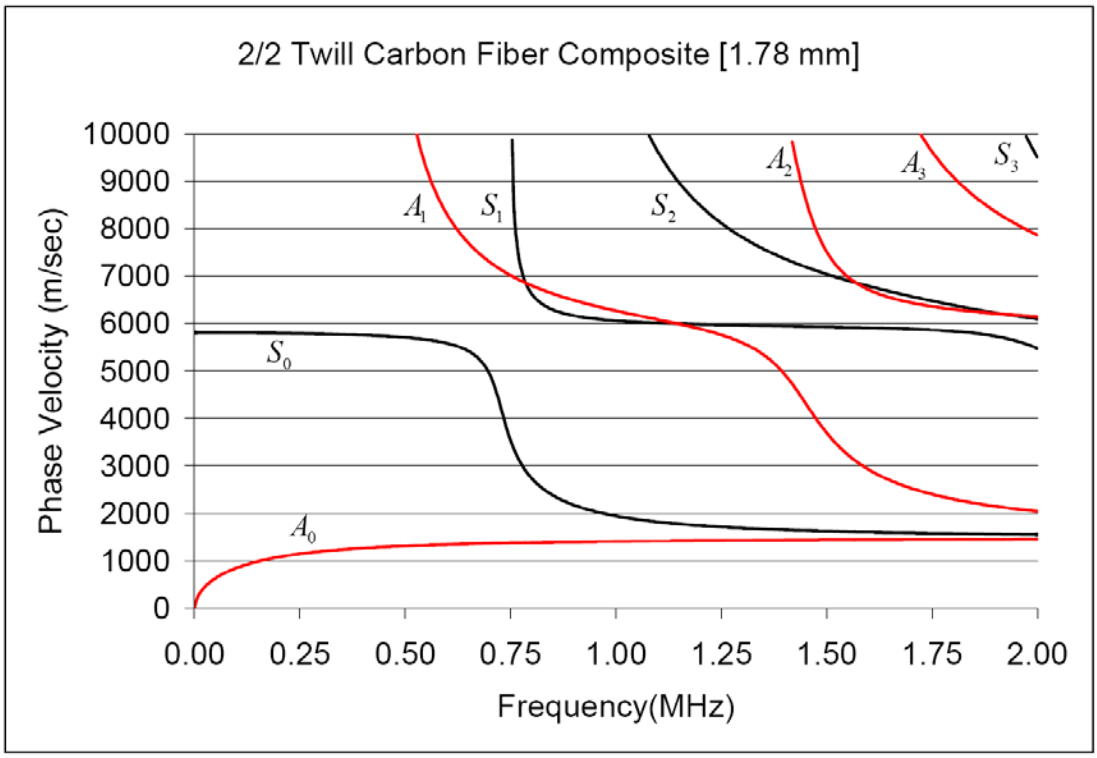

Figure 3-5: Dispersion curve for Lamb wave velocity in composite plate.

3.3 Experimental Approach to Determine Lamb Wave Group Velocity in the Composite Face Sheet

In this section Lamb wave velocity in the composite face plate is measured experimentally and compared with their theoretical values as additional check on the estimates of the elastic constants. The general experimental setup used for the tests is shown in Figure 3-6. Several broadband transducers (B1025, Digital Wave) with flat response in the range (100 kHz to 1 MHz) are placed precisely on the composite surface with the aid of a plexiglass faces sheet with an array of holes drilled with an accuracy of 0.1mm in position. The diameter of the holes is equal to that of the transducers. The plexiglass sheet is attached to the surface of the specimen with marking tapes and it helps in repeating experiments with identical transducer locations.

Thus only two transducers are needed to obtain data from an array of transducers with prescribed positions. The transmission of ultrasound is aided by the application of an ultrasonic gel couplant (Sonotech). Several identical broadband PZT transducers (Digital Wave B1025) are used as transmitters and receivers of the waves. A 5-cycle sinusoidal tone burst enclosed in a Hanning window in the range frequency between 100-350 kHz were generated by an arbitrary waveform generator (Stanford Research Systems) and applied to the PZT actuator. The input source has the following form:

$$P(t) = \frac{1}{2}\left[1 - \cos\left(\frac{2\pi ft}{5}\right)\right]\sin(2\pi ft) \tag{3.24}$$

where f is the central frequency. A four channel signal conditioner (Digital Wave Corp., Model FM-1) is used to boost and filter the signals in all experiments. The ultrasonic signal is digitized and recorded directly in a four-channel digital oscilloscope with 100 MHz sampling rate (54624A, Agilent Technologies).

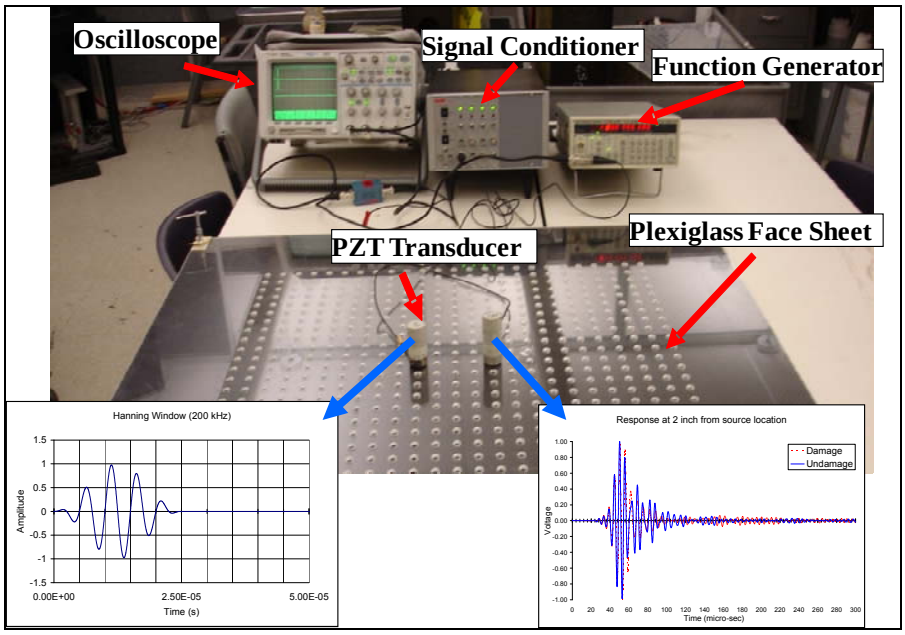

Figure 3-6: Experimental setup for ultrasonic NDE

In order to determine the velocity of the waves, the signals are recorded at distances of 2-10 inches (50.8-254 mm) from the source on the test sample. Since the Lamb waves are dispersive, the direct time-of-flight measurements to calculate the phase velocity would produce error in the results. Thus the dispersive signals need to be subjected to a short time Fourier transform (e.g., Wavelet transform) to determine the group velocity of the waves. To this end the digital signals are processed using an AGU-Vallen Wavelet [42-44] program which performs their wavelet transforms. The wavelet transformation decomposes each signal into frequency bands, and resolution. The received signals and the contour plots of their wavelet transforms are obtained as shown in Figures 3-7 and 3-8.

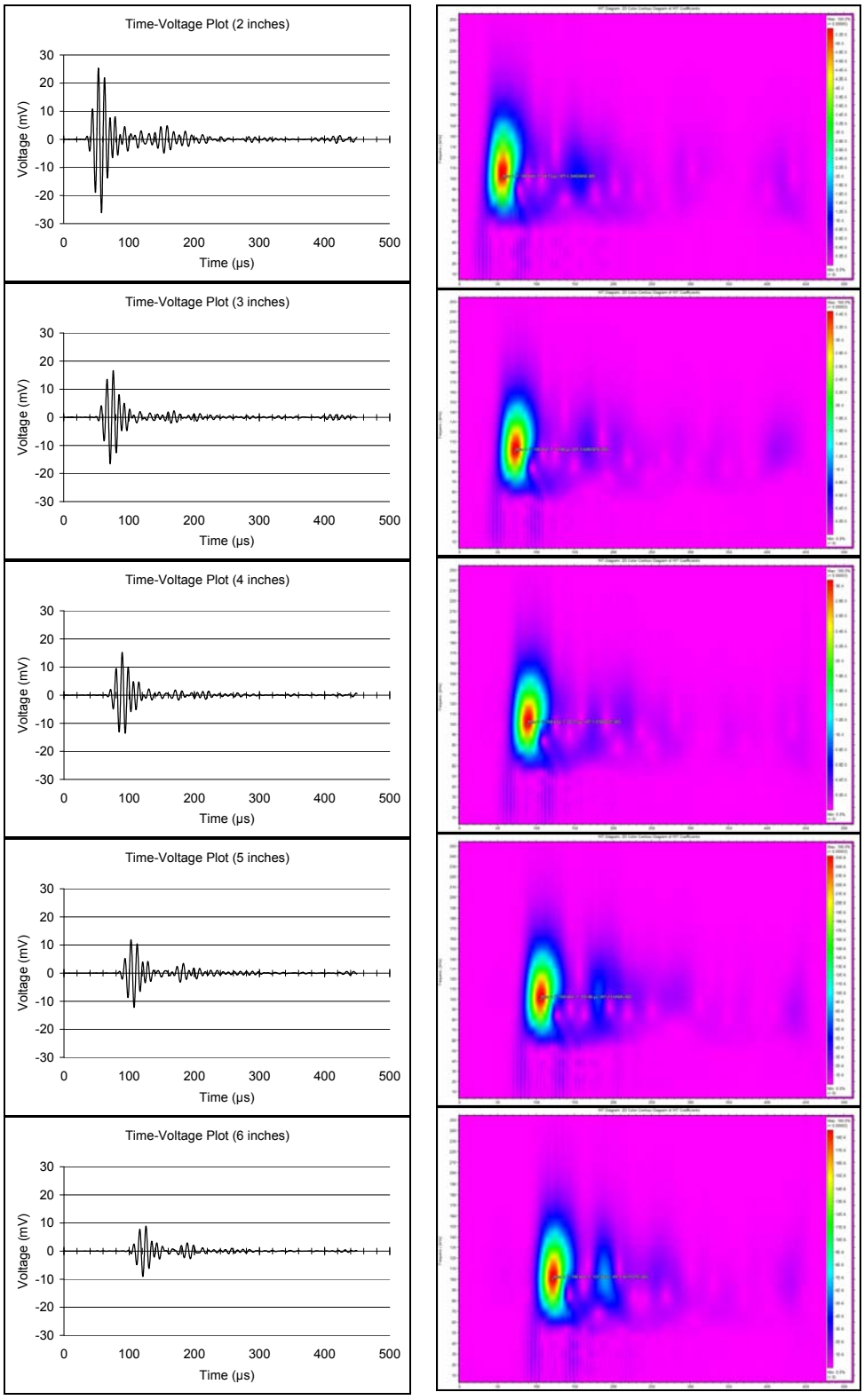

Figure 3-7: Experimentally obtained signals at 2 through 6 inches (50.8 mm – 152.4 mm) and corresponding contour plot of the wavelet transform of the composite face sheet

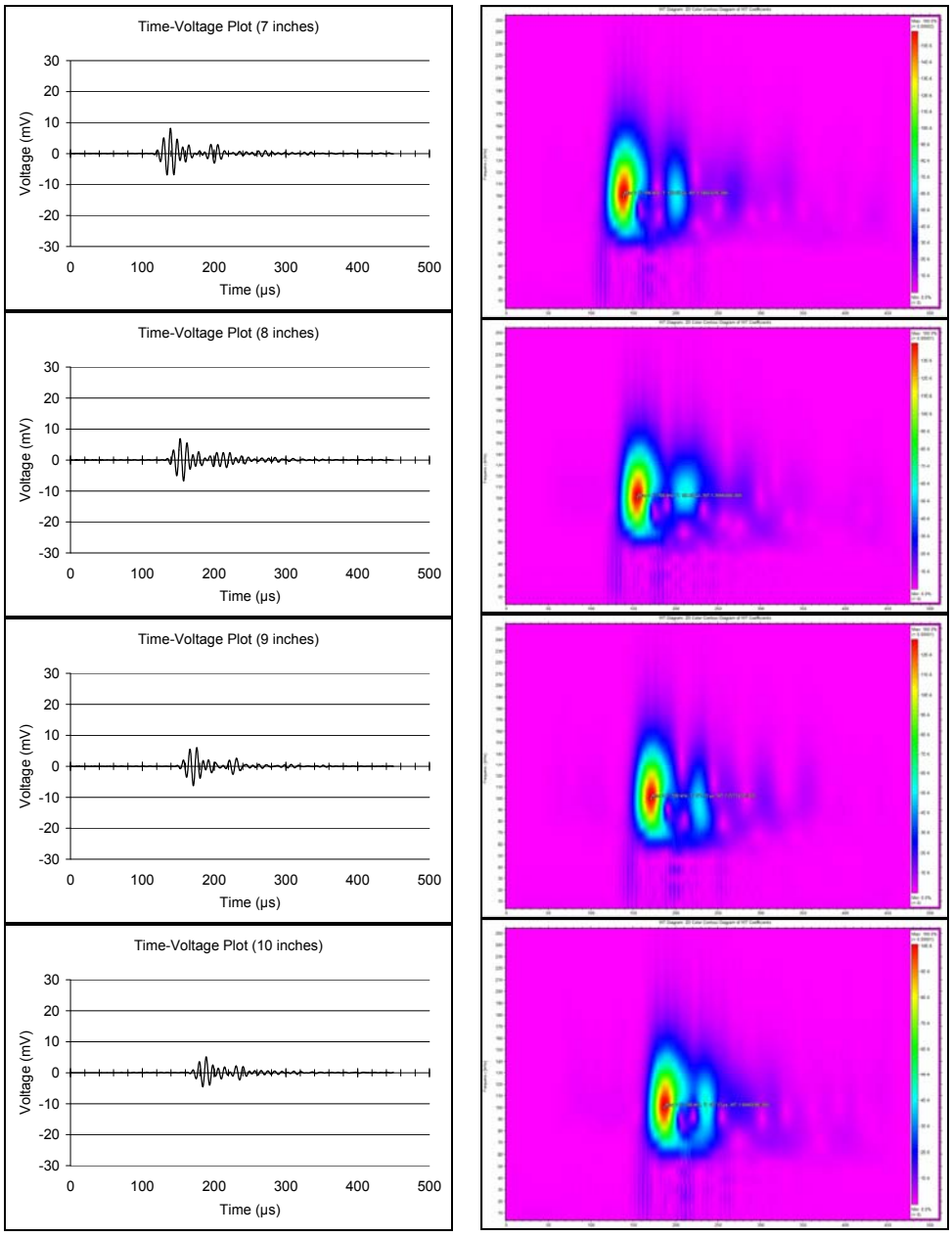

Figure 3-8: Same as Figure 3-7 at 7 through 10 inches (177.8 mm - 254 mm)

From the contour plots the time of arrival of the wave groups at 100 kHz frequency are obtained, and plotted as shown in Figure 3-9. The group velocity at this particular frequency can be calculated by measuring the slope of the line, which in this case is 1.5507 mm/µs. The group velocities at various frequencies using the above approach are presented in Table 3-2.

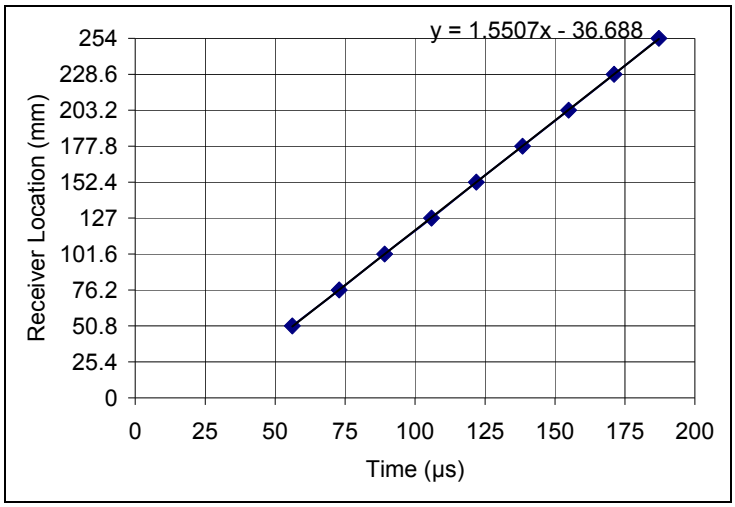

Figure 3-9: Time location plot for 100 kHz input central frequency

Table 3-2: Group velocities at various frequencies in the 1-2 plane of the composite plate obtained experimentally

Frequency (MHz)	Group Velocity (A_0 mode) (m/s)	Group Velocity (S_0 mode) (m/s)
0.100	1550.7	-
0.125	1569.4	-
0.150	1564.6	-
0.175	1550.7	-
0.200	1556.7	-
0.225	1547.9	-
0.250	1526.1	-
0.300	-	5868.2
0.325	-	5644.4
0.350	-	5644.4
0.425	-	5976.5
0.450	-	5969.5
0.475	-	5976.5
0.500	-	5644.4

The theoretical group velocity can be obtained from the following relation

$$c_g = \frac{c}{\left(1 - \frac{\partial c}{\partial \omega} k\right)} \qquad (3.25)$$

where c is phase velocity given in Figure 3-4, ω is the circular frequency, k=ω/c, and $\frac{\partial c}{\partial \omega}$ is obtained by numerical differentiation of the phase velocity curves in Figure 3-5. Both theoretical and experimental group velocities are presented in Figure 3-10. It can be seen that the experimental values agree very well with their theoretical values using the material properties given in Table 2-3, providing additional check on the accuracy of the estimated properties.

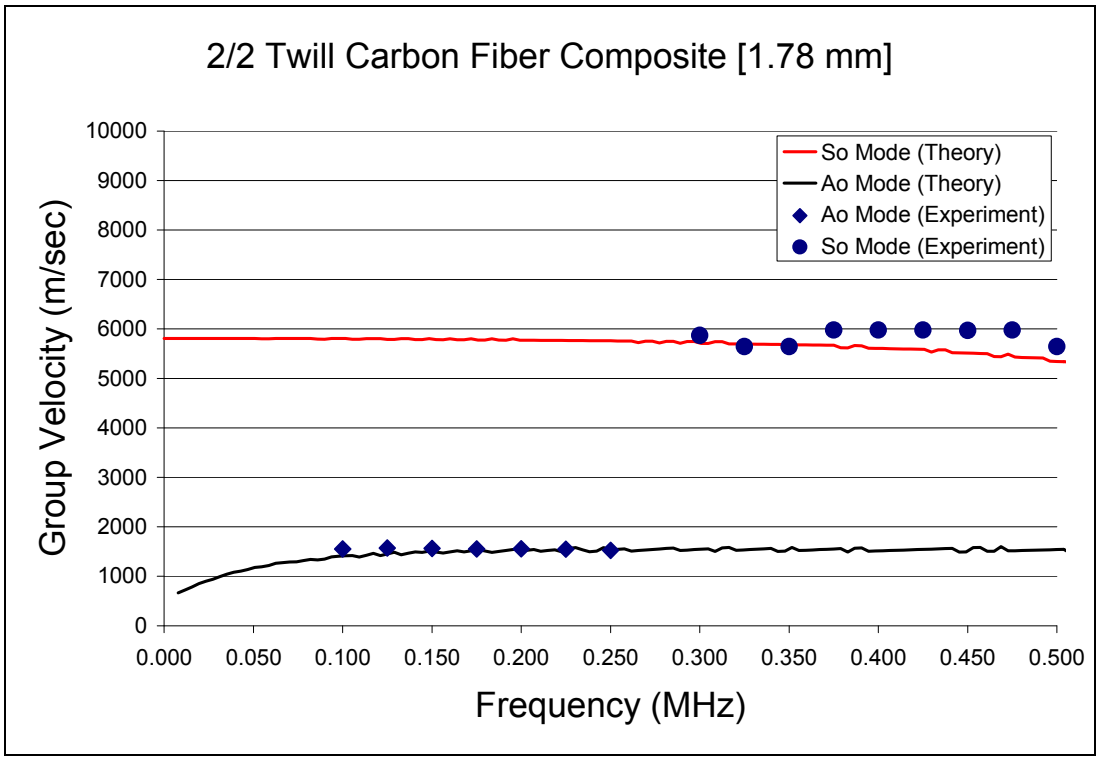

Figure 3-10: Dispersion curve for Lamb wave group velocity in composite plate.

3.4 Verification of Transverse Isotropy of the Composite Panel

In this section, the assumption of the transverse isotropy of the composite plate is verified by measuring Lamb wave group velocity in different directions on the symmetry plane. The measured velocities in different directions using the experimental set up of Figure 3-6 are presented in Table 3-3. It can be seen that velocity is independent of the direction of propagation, confirming the assumption of transverse isotropy of the woven composite plate.

Table 3-3: Group velocity for different angles of propagation in the 1-2 plane of the composite plate

Frequency (MHz)	Group Velocity (A_0 mode only) (m/s)		
	0°	90°	45°
0.100	1550.7	1539.4	1528.6
0.150	1569.4	1516.4	1578.9
0.200	1564.6	1494.1	1596.5
0.250	1550.7	1563.1	1545.0

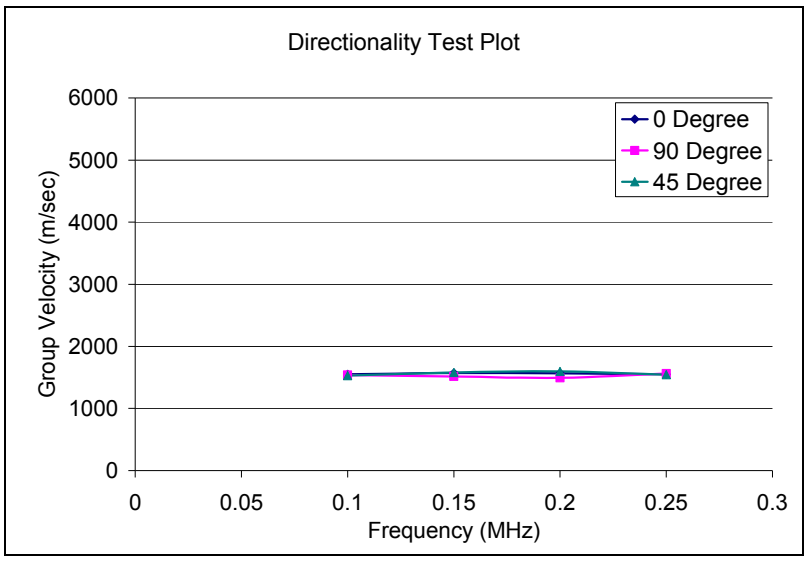

Figure 3-11: Directionality test for composite panel

3.5 Attenuation in the Composite Panel

Attenuation is the loss of signal strength over its propagation distance. This is an important factor when designing a damage-monitoring system, as it will determine how to maximize inspection area with a minimum number of measurements.

For the input source given in equation (3-25) with 100 kHz central frequency, the peak amplitude of the received time-voltage signals (see Figure 3-7) at locations 50.8 mm through 228.6 mm from the source location is measured. A clear signal is obtained at a distance 254 mm from the source location, but the signal strength would likely be inadequate for measurements further away from the source. Figure 3-12 shows the peak signal amplitude at distances 50.8 mm through 228.6 mm.

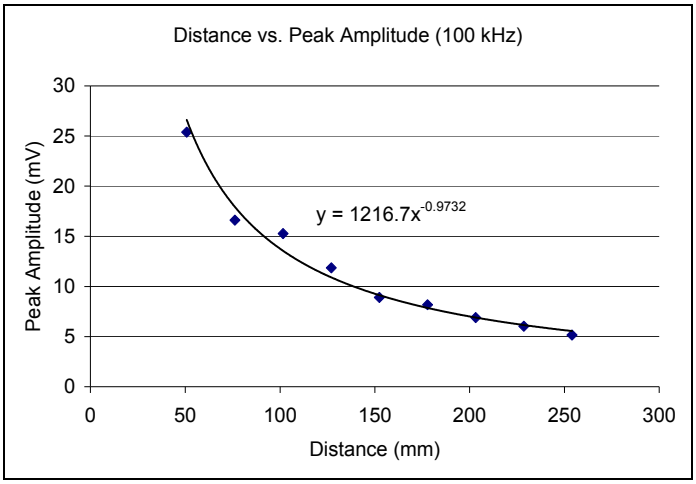

Figure 3-12: Peak voltage with source-receiver distance, indicating ultrasound propagation loss (at 100 kHz).

The amplitude was found to attenuate with distance r as $1/r$, which is typical of geometrical (cylindrical) spreading. Based on these measurements, an inspection range of 228.6 mm can be obtained using a single piezoelectric source transducer (B1025, Digital Wave) at a

drive voltage of 2V. It should be noted, however, the range can be increased at higher driving voltage.

3.6 Lamb Wave Group Velocity in a Honeycomb Composite Structure using Experimental Approach

The honeycomb composite plate consists of a 0.5in. thick aluminum honeycomb core sandwiched between two 0.075in. thick 2/2 twill carbon fiber composite face sheets (Figure 3-13). The velocity of guided Lamb type waves in this three-layered medium can be obtained from its theoretical model using the global matrix developed in [18]. The experimental procedure described in the previous section is used to determine the group velocity of the waves. As in the composite skin discussed in section 3.3 the time-voltage ultrasonic signals were recorded at 9 locations at a distances of 2-10 inches (50.8mm – 254 mm) from the source on the surface of the honeycomb composite structure. The received signals at locations 2-10 inches (50.8mm – 254 mm) from the source given in equation (3.25) and their corresponding contour plots of the wavelet transforms for the received signals are shown in Figure 3-14 and 3-15.

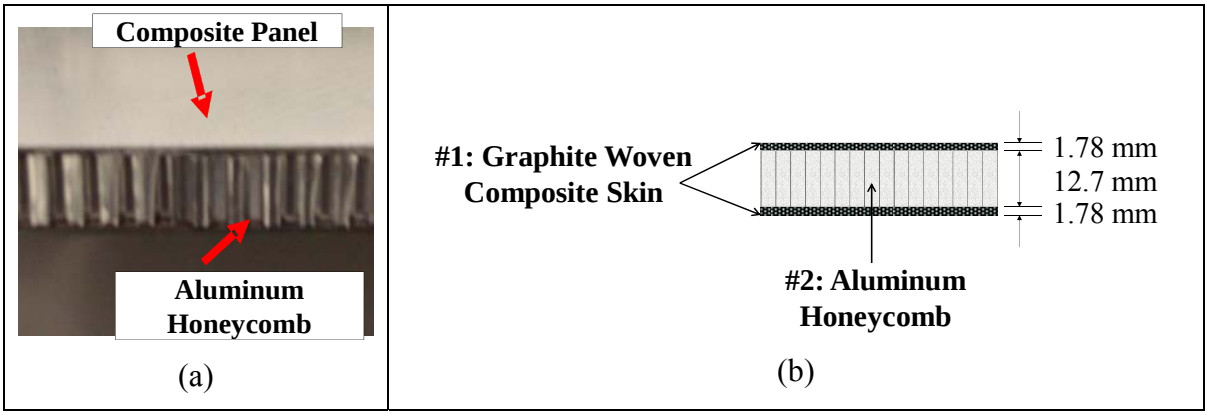

Figure 3-13: (a) 2/2 Twill Woven Carbon Fiber Composite Panel and Aluminum Honeycomb Sandwich Structure, (b) Test specimen dimension.

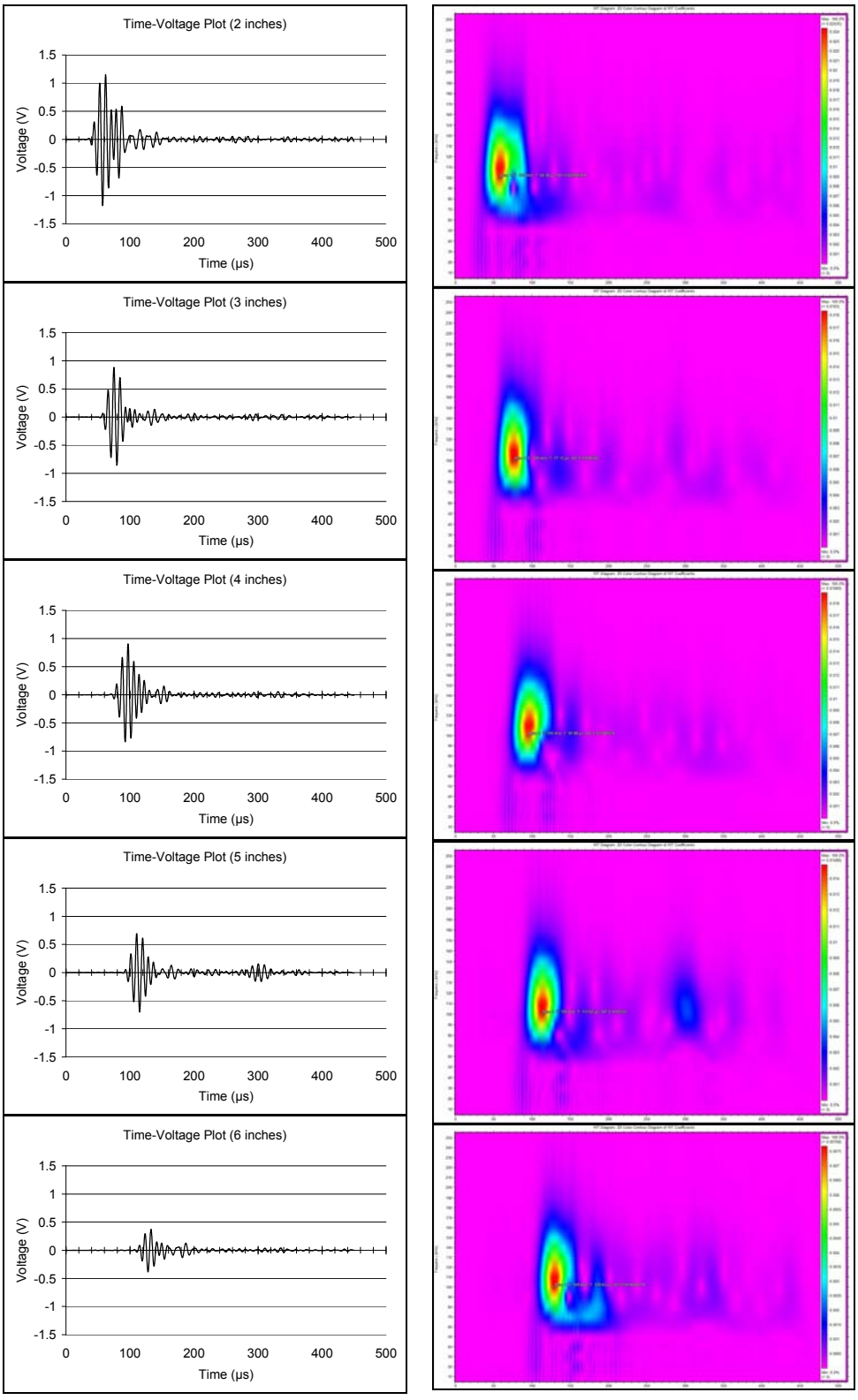

Figure 3-14: Experimentally obtained signals at 2 through 6 inches (50.8 mm – 152.4 mm) and corresponding contour plot of the wavelet transform of the sandwich structure

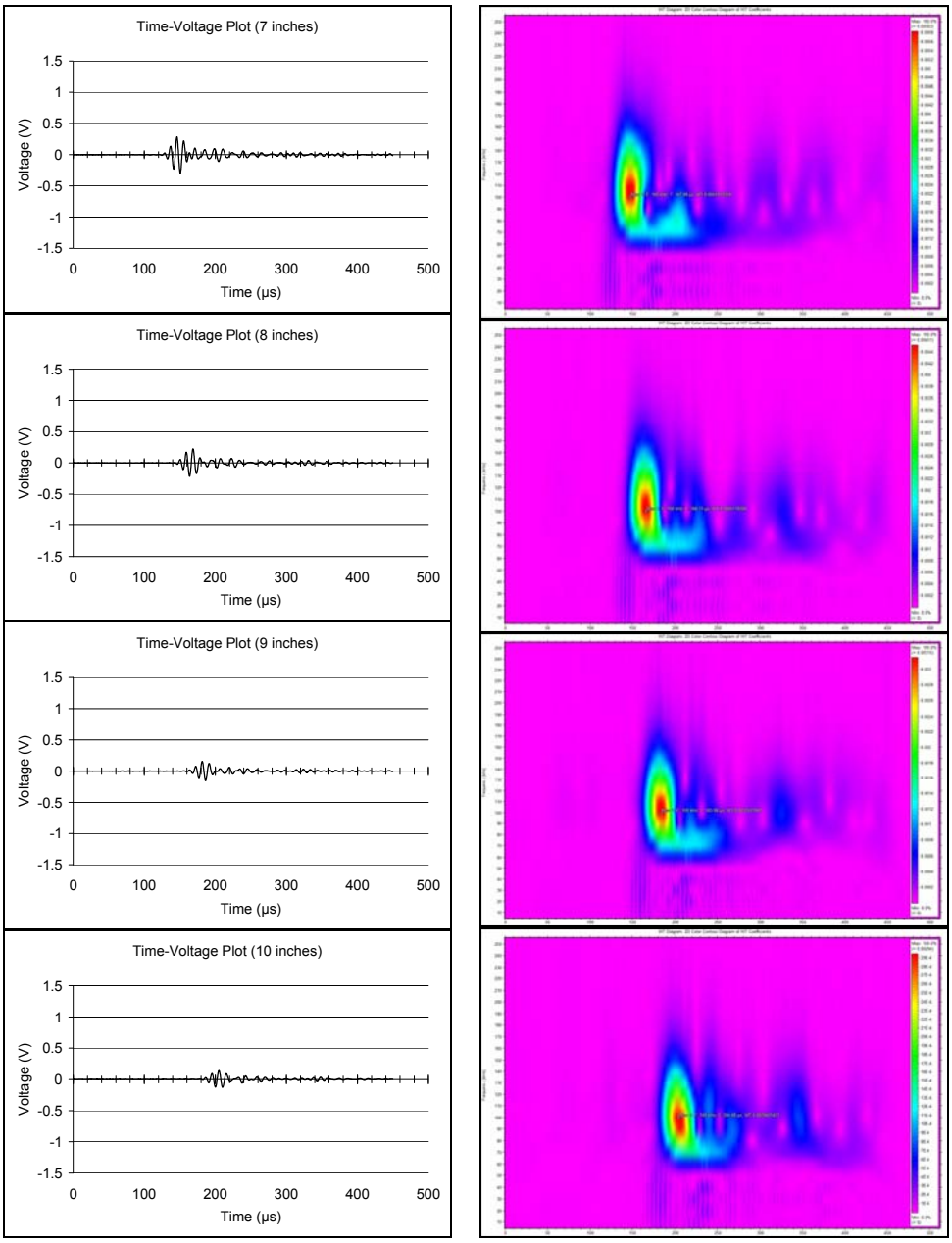

Figure 3-15: Same as Figure 3-14 at 7 through 10 inches (177.8 mm - 254 mm)

Using the same procedure as in previous section the travel time of the wave groups at 100 kHz is shown in Figure 3-14 and the group velocity as a function of frequency is plotted in Figure 3-15.

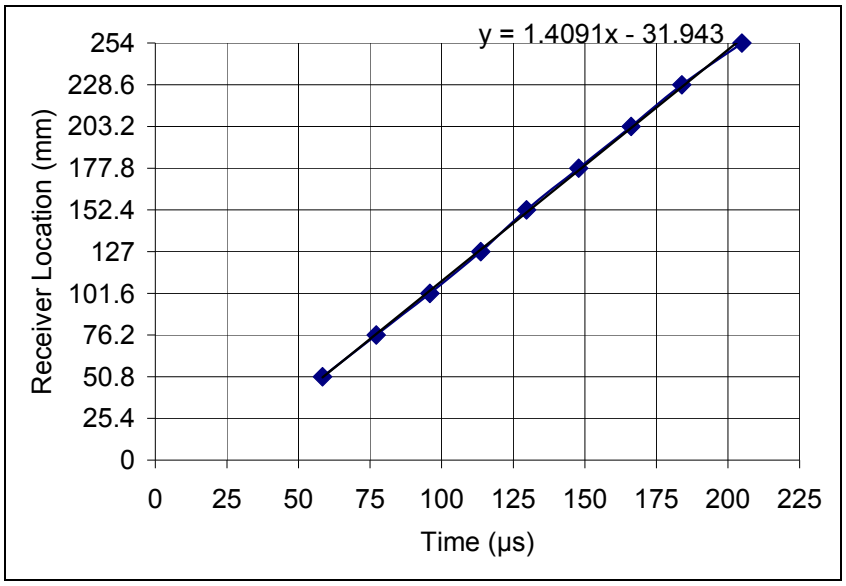

Figure 3-16: Time location plot for 100 kHz input central frequency

Group velocities at various frequencies using the above approach are presented in Table 3-4 and plotted in Figure 3-17.

Table 3-4: Group velocities at various frequencies in the 1-2 plane of the sandwich structure obtained experimentally

Frequency (MHz)	Group Velocity (A_0 mode) (m/s)
0.075	1195.8
0.100	1409.1
0.125	1448.2
0.150	1443.6
0.175	1429
0.200	1430.1
0.250	1422.1

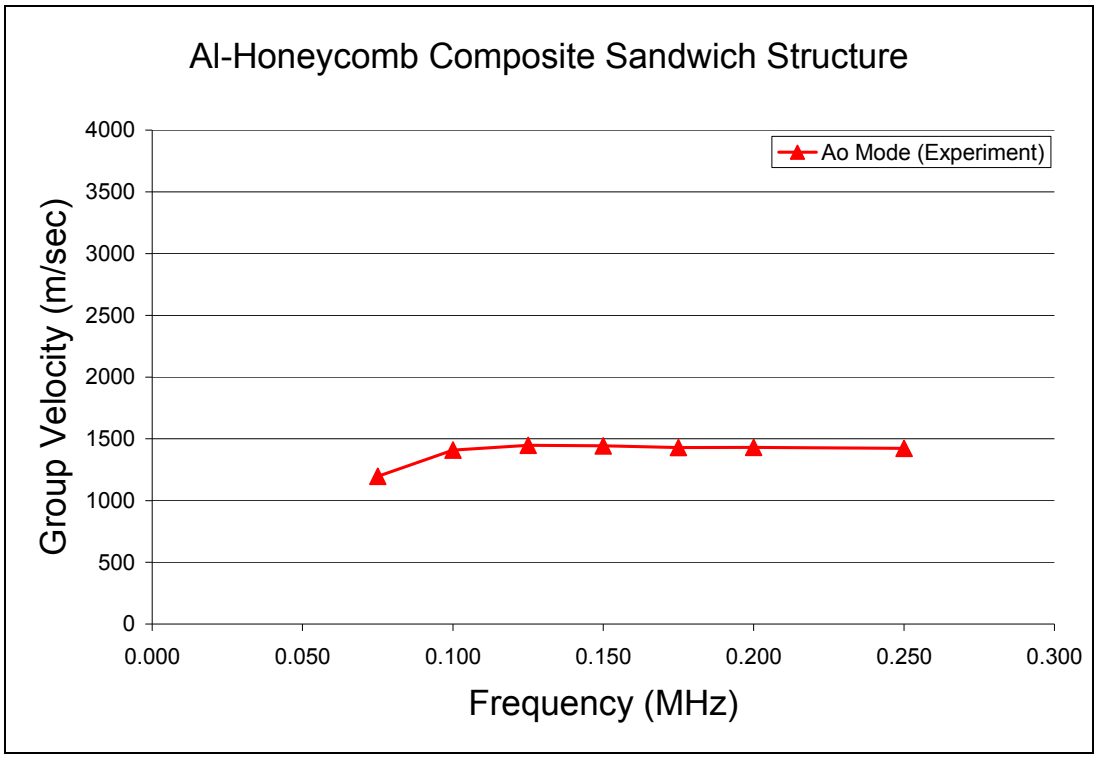

Figure 3-17: Dispersion curve for Lamb wave group velocity in Honeycomb Composite Sandwich Structure.

These results will be compared with those obtained for a numerical simulation in the next section.

3.7 Lamb Wave Group Velocity in a Honeycomb Composite Structure Using Numerical Simulation

A finite element simulation is carried out to determine the characteristics of Lamb waves in a plane-strain model of the sandwich plate. The honeycomb core and composite panel are modeled separately and then assembled together using surface-based tie constrains to connect the nodes at the interface. This constrains ties the two regions together and thus there is no relative motion between them at the interface. The 2-D plane strain finite element model contains 405,000 CPE4R elements (ABAQUS, 4-node bilinear plane strain quadrilateral, with reduced integration, hourglass control) with 420,084 nodes. The mesh density that is used for the

sandwich structure includes at least 10 elemental nodes within the wavelength of each Lamb wave mode. The effective material properties for both the composite panel and honeycomb core used in the simulation are given in Tables 2-3 and 2-5. Both the displacements and rotations are assumed to vanish at the right and the left ends of the model. Guided wave propagation is activated in the sandwich structure using the source given in equation (3.24) with various central frequencies. Figures 3-18 and 3-19 show the schematic of the finite element model for both symmetric and anti-symmetric cases with appropriate boundary conditions, the applied vertical loads and the receiver locations. The red spots represent the source locations and blue spots represent the receiver locations. The dynamic simulation was accomplished using the ABAQUS/EXPLICIT® [45] code. The vertical displacement on the surface of the plate were calculated at the locations R_2, R_3, R_4, R_5, R_6, R_7, R_8, R_9 and R_{10}. The time-displacement data were calculated at 9 locations at a distance of 2 - 10 inches (50.8 mm – 254 mm) from the source on the surface of honeycomb composite sandwich structure. The time-displacement data were then downloaded directly to a personal computer for post processing in AGU-Vallen Wavelet [42-44] program. The received time-displacement data for anti-symmetric case at locations 2-10 inches (50.8mm – 254 mm) from the source and the corresponding contour plots of the wavelet transforms for the received signals are shown in Figures 3-21 and 3-22.

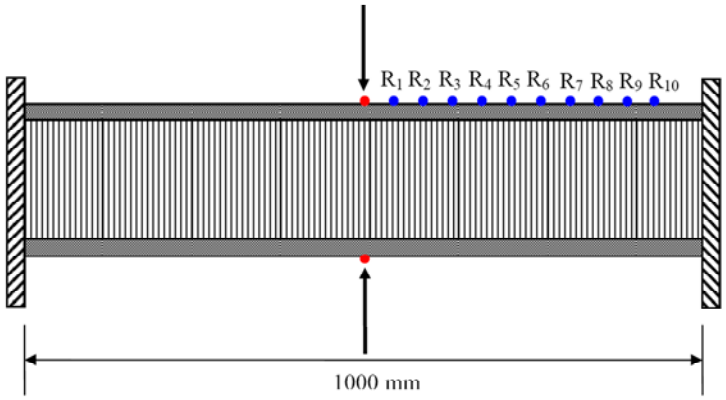

Figure 3-18: Schematic of the 2-D finite element model for the symmetric case with applied vertical source and receiver positions.

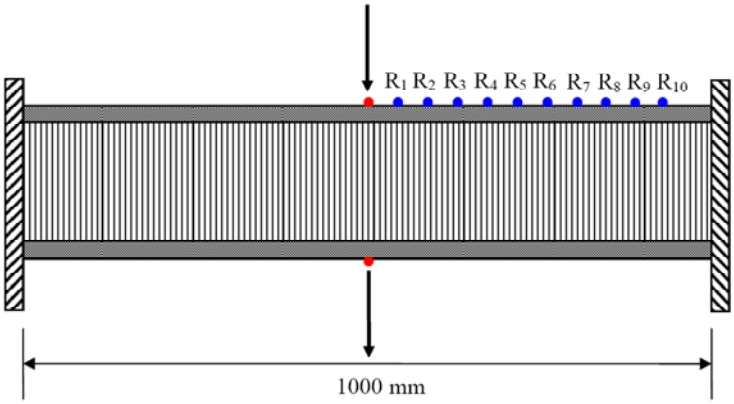

Figure 3-19: Same as Figure 3-15 for the anti-symmetric case

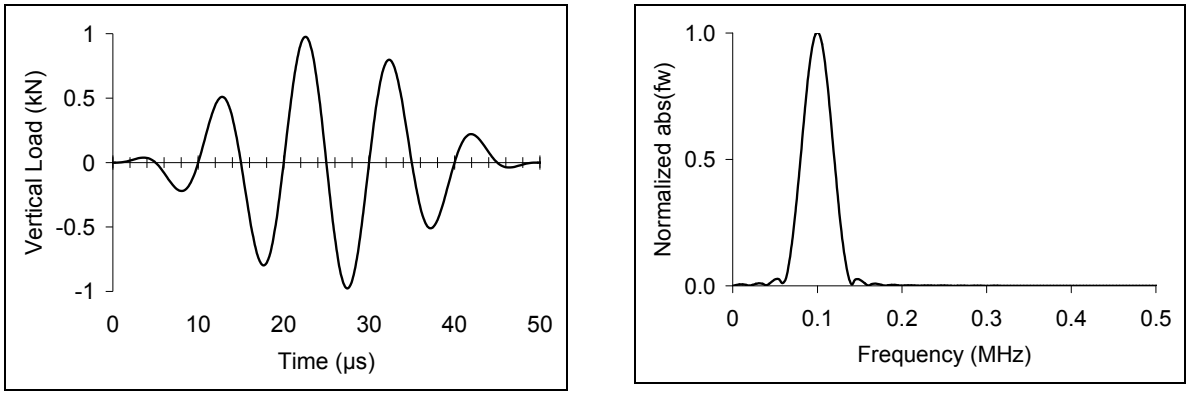

Figure 3-20: A narrow band pulse - central frequency 100 kHz in (a) Time domain (left) (b) Frequency Domain (right)

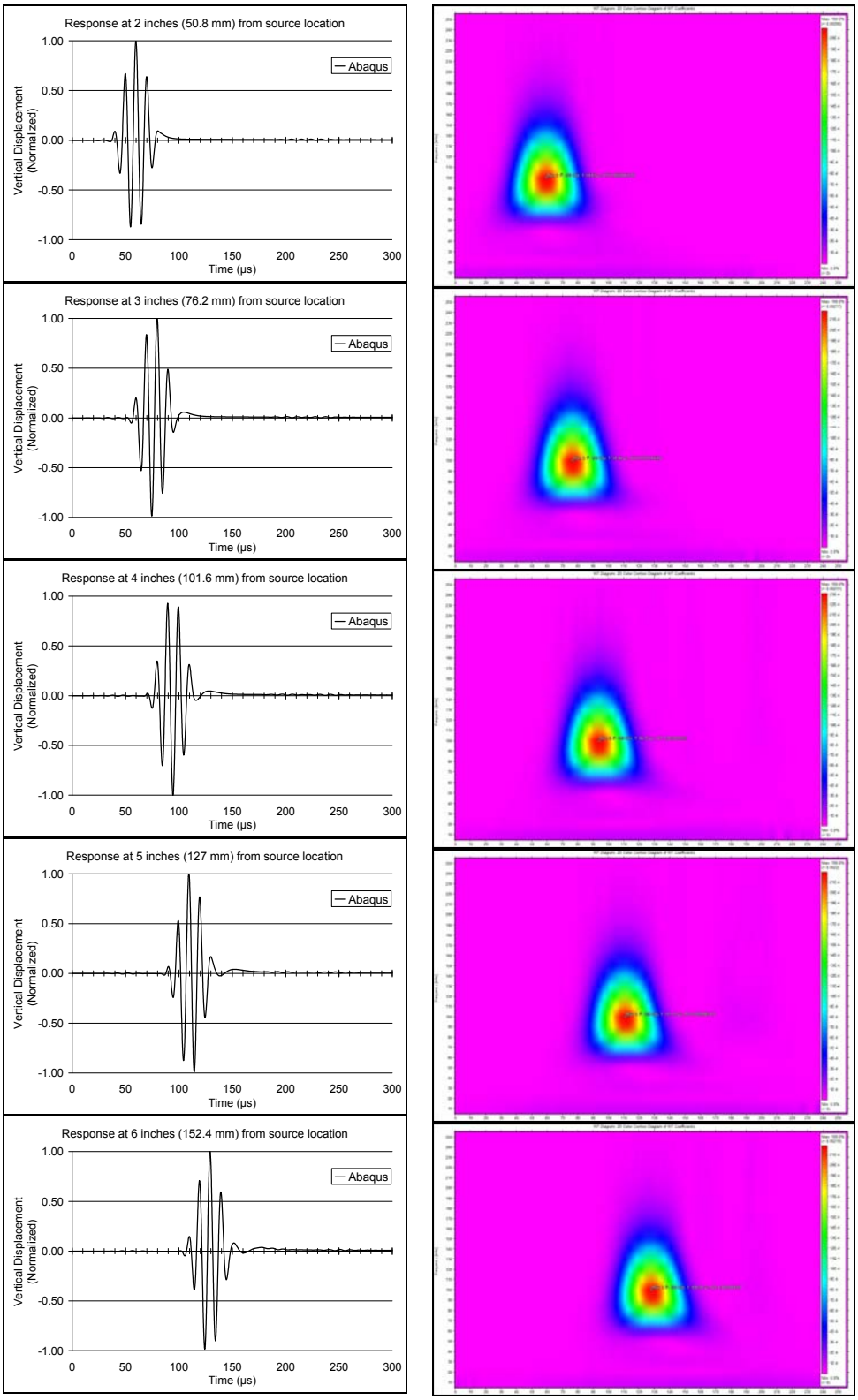

Figure 3-21: Numerically obtained signals at 2 through 6 inches (50.8 mm – 152.4 mm) and corresponding contour plot of the wavelet transform of the sandwich structure

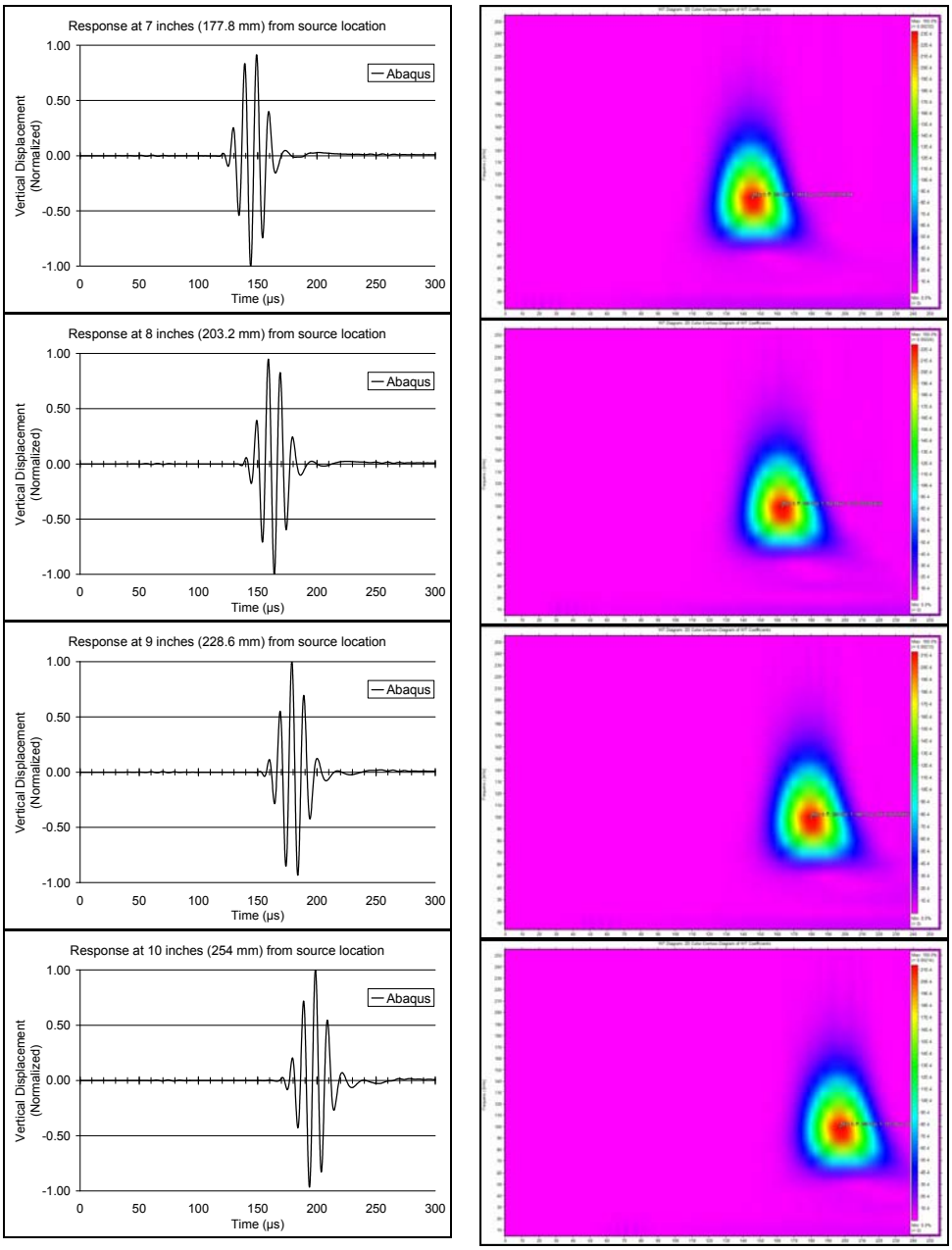

Figure 3-22: Same as Figure 3-21 at 7 through 10 inches (177.8 mm – 254 mm)

Again the travel time of the wave groups at 100 kHz is shown in Figure 3-20. The group velocity as a function of frequency is plotted in Figure 3-24 together with the experimental values obtained in the previous section. The two results agree quite well, indicating the accuracy of the material model.

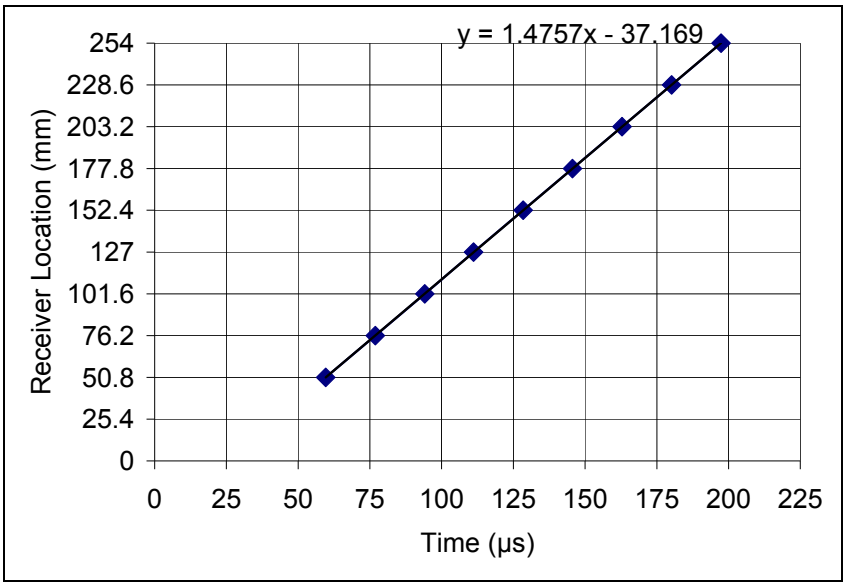

Figure 3-23: Time location plot for 100 kHz input central frequency

Table 3-5: Group velocities at various frequencies in the 1-2 plane of the sandwich structure obtained using numerical simulation

Frequency (MHz)	**Group Velocity (A_0 mode) (m/s)**	**Group Velocity (S_0 mode) (m/s)**
0.05	1323.2	-----
0.075	1425.3	-----
0.100	1475.7	1177
0.125	1501.8	1342.4
0.150	1512.3	1404.3
0.175	1514.5	1448.3
0.200	1512.6	1466.1
0.250	1500.7	1486.5

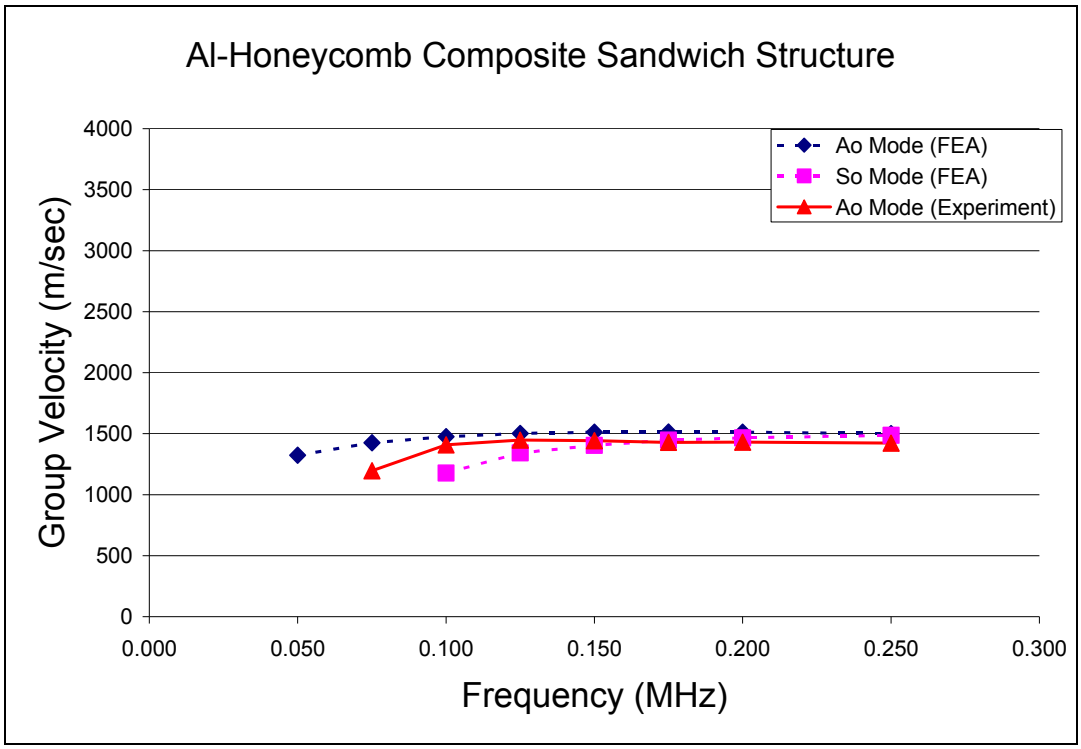

Figure 3-24: Dispersion curve for Lamb wave group velocity in Honeycomb Composite Sandwich Structure.

3.8 Verification of Transverse Isotropy of the Sandwich Panel

As section 3.4 the assumption of the transverse isotropy of the sandwich panel is verified by measuring the Lamb wave group velocity in different directions on the symmetry plane. The measured velocities are presented in Table 3-6 and plotted in Figure 3-25. The velocity is nearly independent of the propagation direction confirming the assumption of transverse isotropy.

Table 3-6: Group velocity for different angles of propagation in the 1-2 plane of the sandwich structure

Frequency (MHz)	Group Velocity (A_0 mode only) (m/s)		
	0°	90°	45°
0.100	1409.1	1328.1	1330.4
0.150	1443.6	1411.1	1367.8
0.200	1430.1	1430.9	1381.4

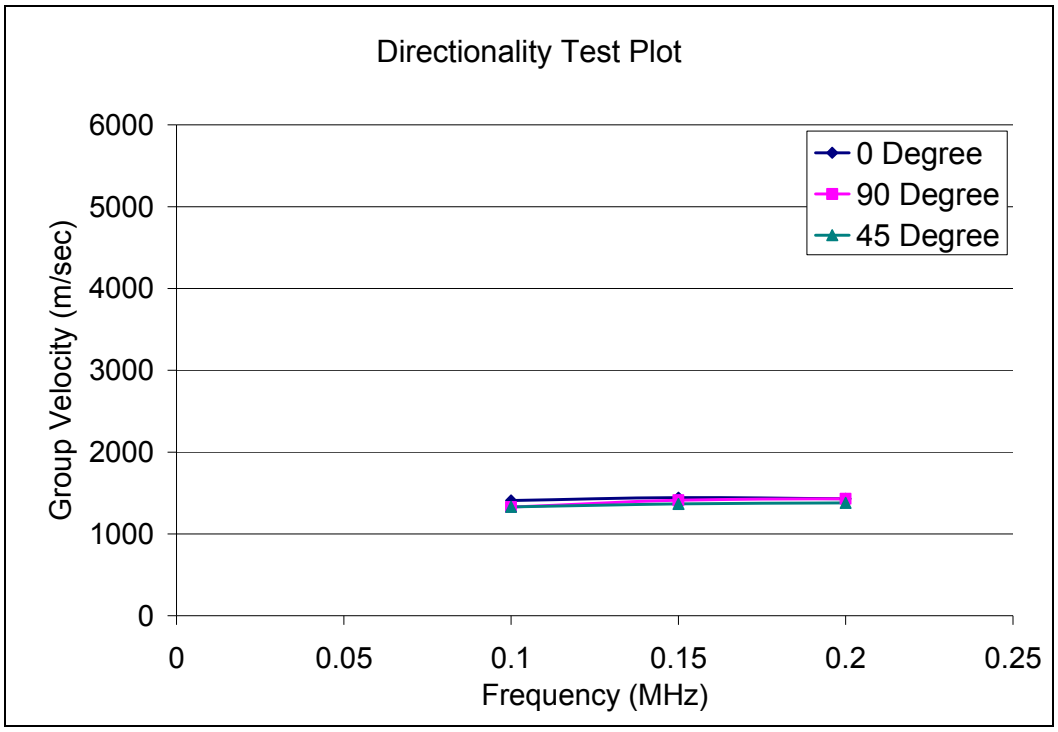

Figure 3-25: Measured Lamb wave group velocity in the 1-2 plane for the sandwich structure

3.9 Attenuation in the Sandwich Plate

The peak amplitude of the measured signal as a function of the source-receiver distance is plotted in Figure 3-26. Again the amplitude was found to attenuate with distance *r* as 1/*r*, which is typical of geometrical (cylindrical) spreading. Based on these measurements, an inspection range of 228.6 mm can be obtained using a single piezoelectric source transducer (B1025, Digital Wave) at a drive voltage of 2V.

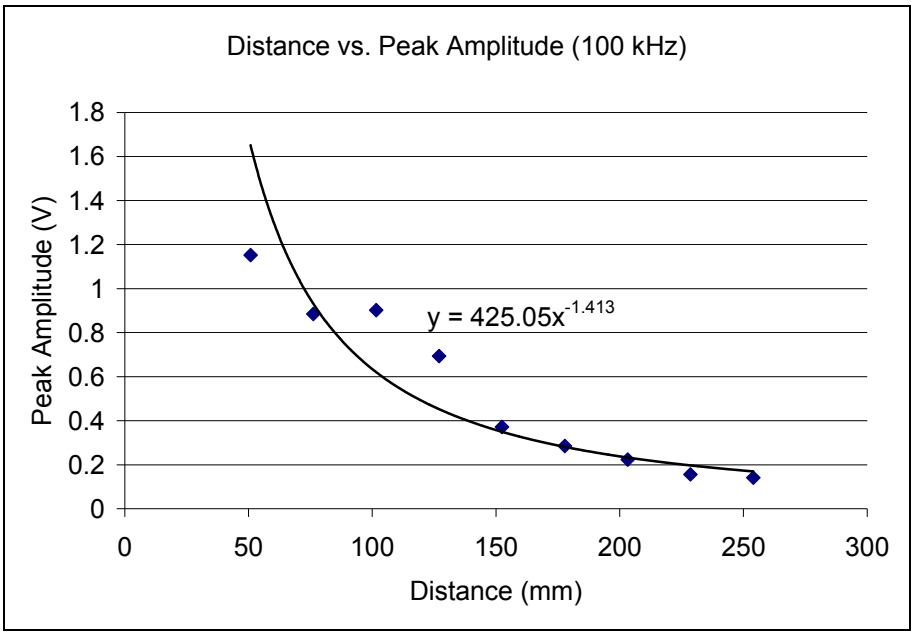

Figure 3-26: Piezoelectric transducer peak voltage with reference to source-receiver distance, indicating ultrasound propagation loss (at 100 kHz).

Chapter 4 DAMAGE DETECTION IN A COMPOSITE PANEL USING GUIDED WAVES

In this chapter, the problem of detection of damage due to impact on the composite face sheet using ultrasonic Lamb waves is considered. An improved ultrasonic test setup consisting of a distributed, high fidelity and broad band sensor array is used to determine changes in the dynamical properties of the composite face sheet resulting from the appearance of the impact damage. A damage index comparing the measured dynamical response of two successive states of the structure is introduced as a determinant of structural damage. The method relies on the fact that the dynamical properties of a structure change with the presence of damage. The value of the index at a given sensor increases with its proximity to the damage. A sensitivity analysis is carried out in an effort to determine a threshold value of the index below which no reliable information about the state of health of the structure can be estimated. It is shown that the automated procedure is able to identify damage from its appearance, with a high degree of confidence.

Damage identification using the wave propagation approach requires a good understanding of the properties of the various types of waves that can be transmitted in the structure in presence or absence of damage. In thin-walled structures, the predominant waves are Lamb waves that can propagate to relatively large distances from the source. The propagation characteristics of these waves in the composite face sheet used in this study are described in Chapter 3. The specific characteristics of waves in a face sheet when they are generated by surface mounted ultrasonic sources requires the solution of a more complex problem involving boundary loads. Similar problems involving dynamic surface loads on multilayered composite laminates have been solved [18-27], the symmetry axis in these problems has been assumed to be parallel to the laminate surface. The solution of the present problem where the symmetry axis is

normal to the plate surface does not seem to be available in the literature. In this section the response of the woven composite face sheet to a dynamic surface line load is calculated by means of numerical (Finite Element) method. The calculated waveforms are compared with those obtained from ultrasonic experiments using the test set up described in section 3.3 for their mutual validation.

4.1 A plane strain Finite Element Modeling of Lamb Wave Propagation in the Woven Composite plate

The Finite element method offers several advantages over analytical and experimental methods. The powerful software packages that are available today offer flexibility with regards to model complexity and analysis that cannot be easily achieved with experimental or analytical methods. There are a number of commercially available software packages that perform modeling and finite element analysis. Of the software packages that were available to us, ABAQUS offered an explicit-dynamic modeling capability that we needed for this particular case. A dynamic finite element simulation was conducted to evaluate the wave propagation characteristics in the composite plate. The 2-D plane strain finite element model of the composite plate contained CPE4R elements (ABAQUS, 4-node bilinear plane strain quadrilateral, with reduced integration, hourglass control) with 50010 nodes. The mesh density that was used for the composite plate included at least 10 elemental nodes within the wavelength of the Lamb wave modes. The material properties used in the simulation are given in Table 2-3.

Figure 4-1 shows the schematic of the 2-D model with applied vertical load and receiver locations; the red spots represent the source and blue spots represent the receivers.

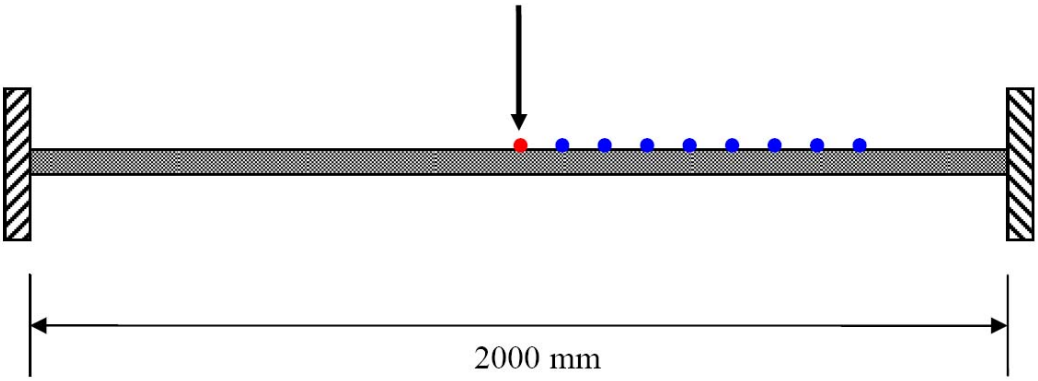

Figure 4-1: Schematic of the 2-D model with applied vertical source and receiver positions.

4.2 Lamb Wave Propagation in Transverse Isotropic plate due to Modified Input Source

The input source from the function generator used in the experiment given in equation (3-24), is plotted in Figure 4.2a for a central frequency of 100 kHz. However this source is modified by various components of the test set up before it is transmitted as a force on the specimen.

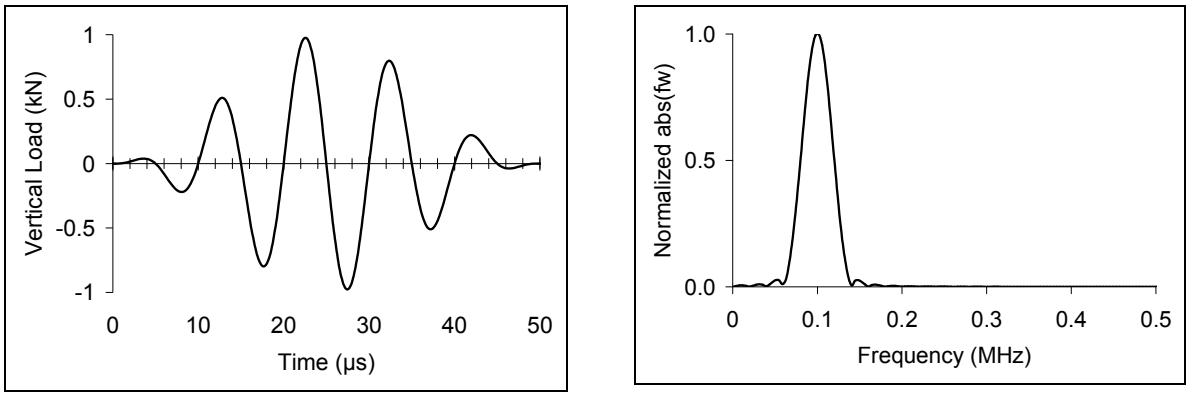

Figure 4-2: A narrow band pulse - central frequency 100 kHz in (a) Time domain (left) (b) Frequency Domain (right)

In the frequency domain the modified input source signal is calculated from equation (4.1).

$$F_{mod}(\omega) = \frac{V_{exp}(\omega)}{U_{Th}(\omega)} \times F(\omega) \qquad (4.1)$$

where $V_{exp}(\omega)$ is the received signal at a given location on the composite panel obtained experimentally and $U_{Th}(\omega)$ is the received signal at the same location for a source $F(\omega)$ in the FEA model. Once $F_{mod}(\omega)$ is obtained, it is inverted in the time domain to determine modified input force for the FEM model that can be compared with experimental data. An example of such a modified signal is shown in Figure 4-3.

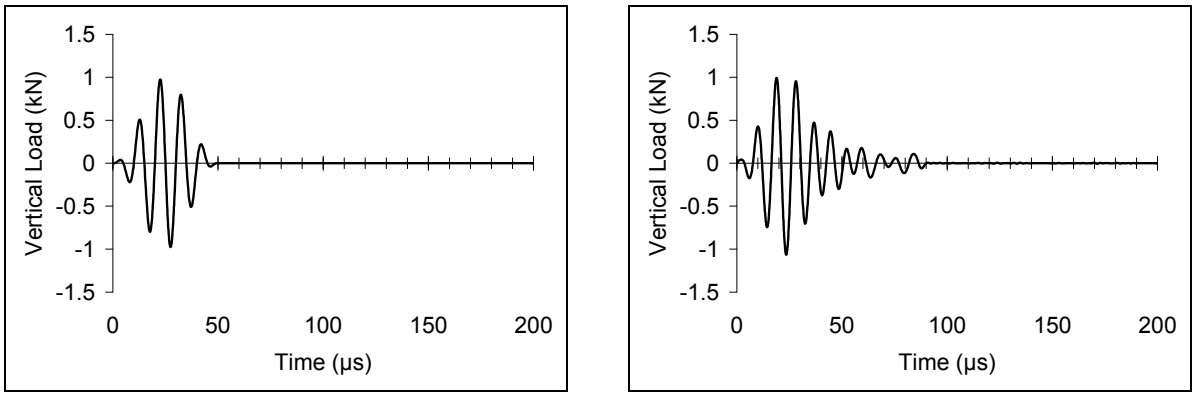

Figure 4-3: (a) Signal used in the experiment (left)
(b) Modified signal for input in the FE model (right)

The Experimental and FEA responses at receiver locations due to modified five-cycle sine pulse at 100 kHz central frequency are shown in Figure 4-4.

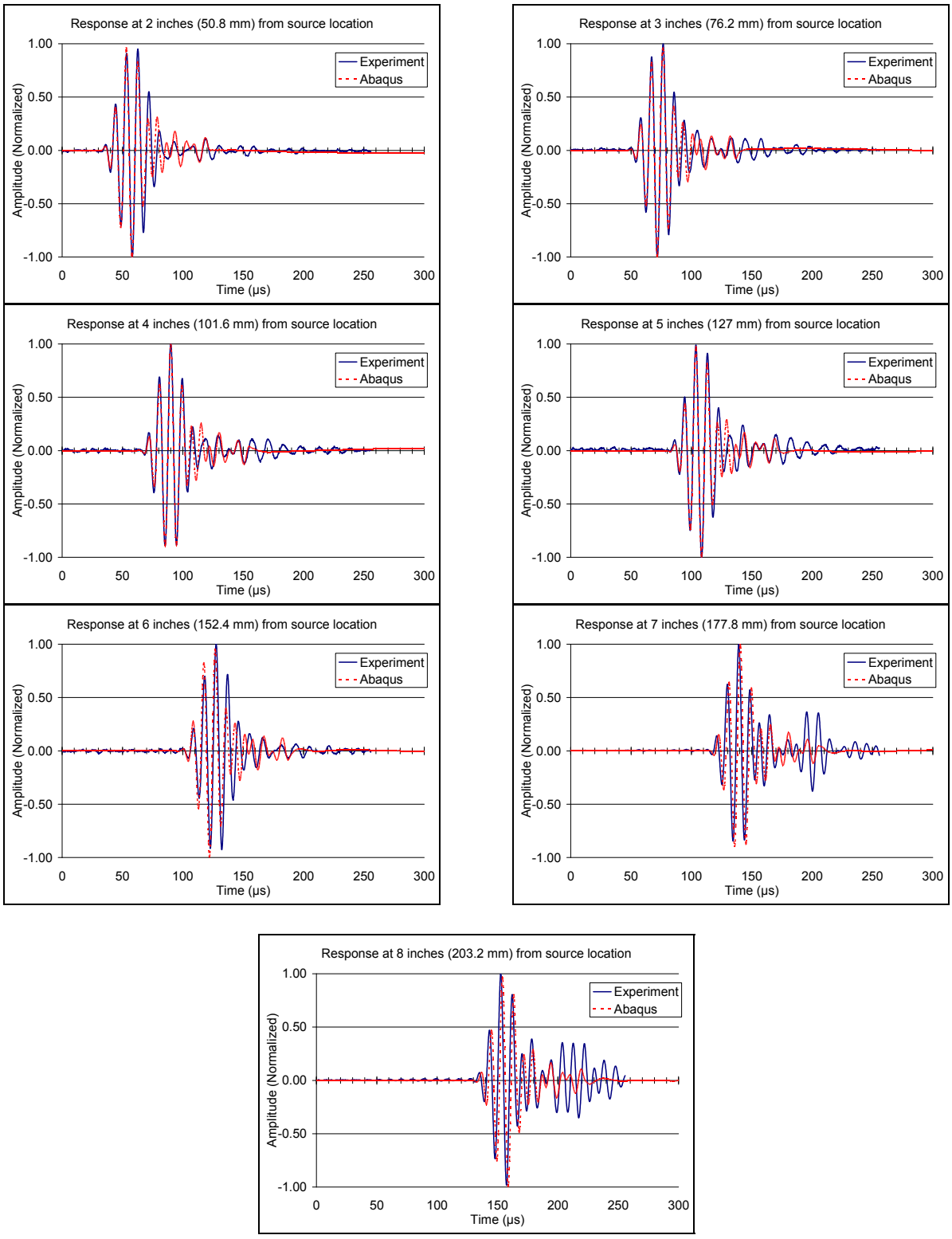

Figure 4-4: Experimentally and numerically obtained signals at 2-8 inches (50.8 mm - 203.2 mm) in the composite face sheet

4.3 Structural Health Monitoring (SHM) Using Guided Wave Data

The research in this chapter is directed toward developing a reliable method for detecting and characterizing existing and emerging defects in critical structural components (plates) before they grow to a critical size and compromise the safety and integrity of the structure. The damage may be due to foreign object impact on the surface or internal delamination. An improved ultrasonic test setup consisting of distributed, high fidelity sensor arrays is used to determine changes in the dynamical properties of the composite face sheet with the appearance of impact damage. A damage index, comparing the measured dynamical response of two successive states of the structure is introduced as a determinant of structural damage. The method relies on the fact that the dynamical properties of a structure change with the initiation of impact damage. The value of the index at a given sensor increases with the proximity of the impact damage to the sensor. A sensitivity analysis has been carried out in an effort to determine a threshold value of the index below which no reliable information about the state of health of the structure can be estimated. It is shown that the automated procedure is able to identify an impact damage right from its appearance, with high degree of confidence.

Experimental Setup

The general experimental setup used for the test cases is shown in Figure 3-6 and discussed in section 3.3. A five-cycle sinusoidal tone bursts enclosed in a Hanning window with frequency 200 kHz (Figure 4-5) was generated by an arbitrary waveform generator (Stanford Research Systems).

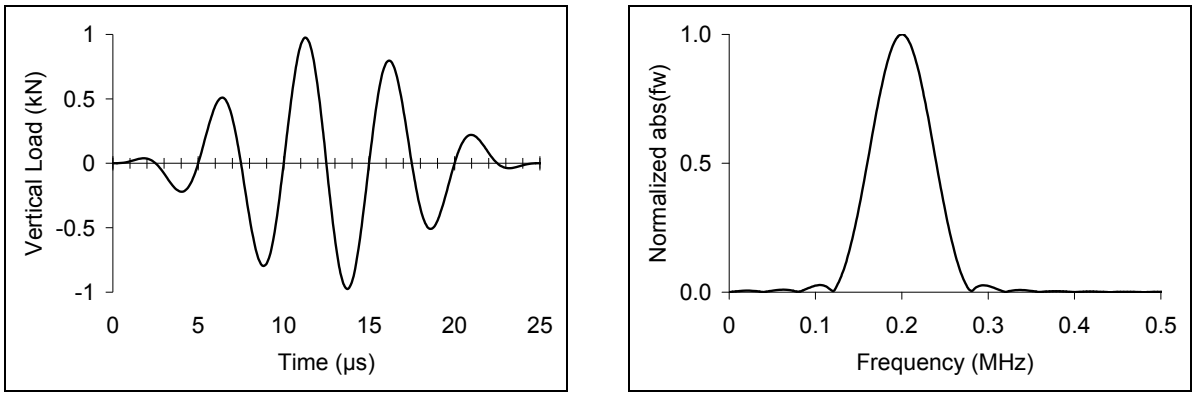

Figure 4-5: A narrow band pulse - central frequency 200 kHz in (a) Time domain (left) (b) Frequency Domain (right)

Damage Index

A 2/2 twill woven carbon fibre composite panel of thickness 1.78 mm was taken and impacted at particular location. First a baseline ultrasonic response data (time-voltage) was created for the undamaged specimen. Figure 4-6 shows the distribution of transmitter and receiver sensors on the composite panel. The red spots represent source locations whereas the blue spots represent the receiver locations. The specimen was impacted once from given height and weight (Table 4-1) at a particular location as shown in Figure 4-6. After the panel was impacted time-voltage data are collected exact way as the base line data. For statistical analysis, five sets of data are taken for each case by three different operators.

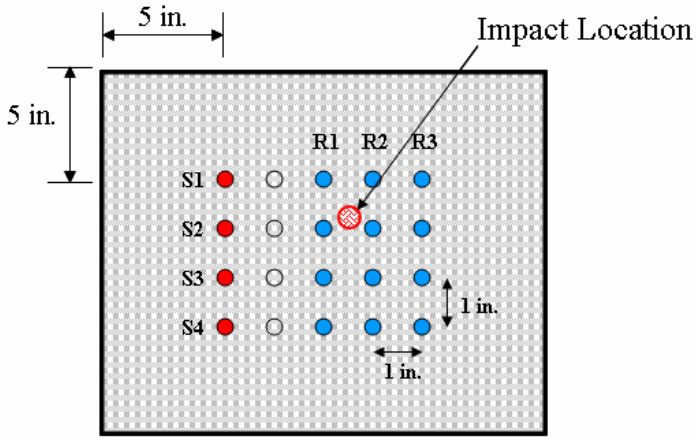

Figure 4-6: Source is fixed at S1 through S4 and receiver is moved along their respective row

Table 4-1: Impact height, weight, velocity and energy.

Height (m)	Weight (kg)	Impact Velocity (m/s)	Impact Energy (Joule)
0.18	5.1	1.88	9.0

In both pre and post-damage cases, the signals are recorded in the time domain and then transformed into the frequency domain by fast-Fourier transform (FFT). The damage index *DI* [5] at the *i* th sensor location is defined as follows:

$$(DI)_i = \left| 1 - \frac{\{F_i\}^T_{\text{post-damage}} * \{F_i\}_{\text{post-damage}}}{\{F_i\}^T_{\text{pre-damage}} * \{F_i\}_{\text{pre-damage}}} \right| \qquad (4.2)$$

where, *F* is the frequency domain response vector of the signal, whose elements are calculated in the frequency range of interest.

Damage produced by the impact modifies the elastic waves propagating between the source and the receivers. Thus the pre-damage and post-damage signals at some control points differ in their properties. Complete pre- and post time-voltage signals at all the control points for one specific trial and the corresponding FFT plots for the received signals are shown in Figure 4-7 through Figure 4-10. A careful model based analysis of the signals can in principle be used to

determine the nature, location and severity of the damage. However, the damage caused by the impact is extremely complex, and the solution of even the direct problem of wave interaction with the damaged region in this complex structure is extremely difficult if not impossible. The damage index approach offers a more pragmatic approach for approximately locating and characterizing the damage. It can be seen from Figures 4-8 that the influence is most pronounced at locations S2R2 and S2R3 due to the transmission of the waves through the damaged area. The index is calculated using the square of the measured voltage as the response parameter in equation (4.2) at 12 control points in the frequency range of 0 - 0.4 MHz and are plotted in Figure 4-11.

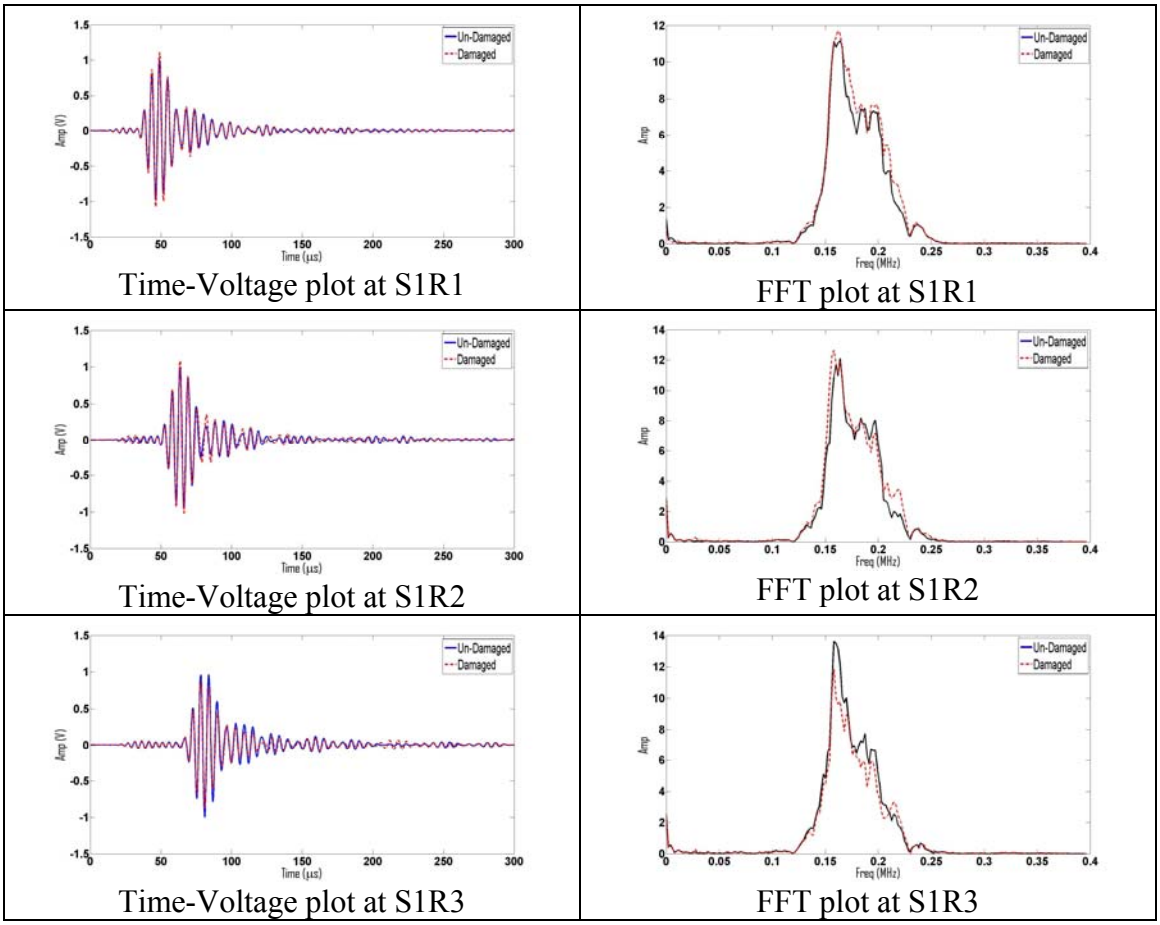

Time-Voltage plot at S1R1 | FFT plot at S1R1

Time-Voltage plot at S1R2 | FFT plot at S1R2

Time-Voltage plot at S1R3 | FFT plot at S1R3

Figure 4-7: Undamaged and damaged signals in a composite face sheet at locations S1R1, S1R2, and S1R3 and their corresponding FFT plots

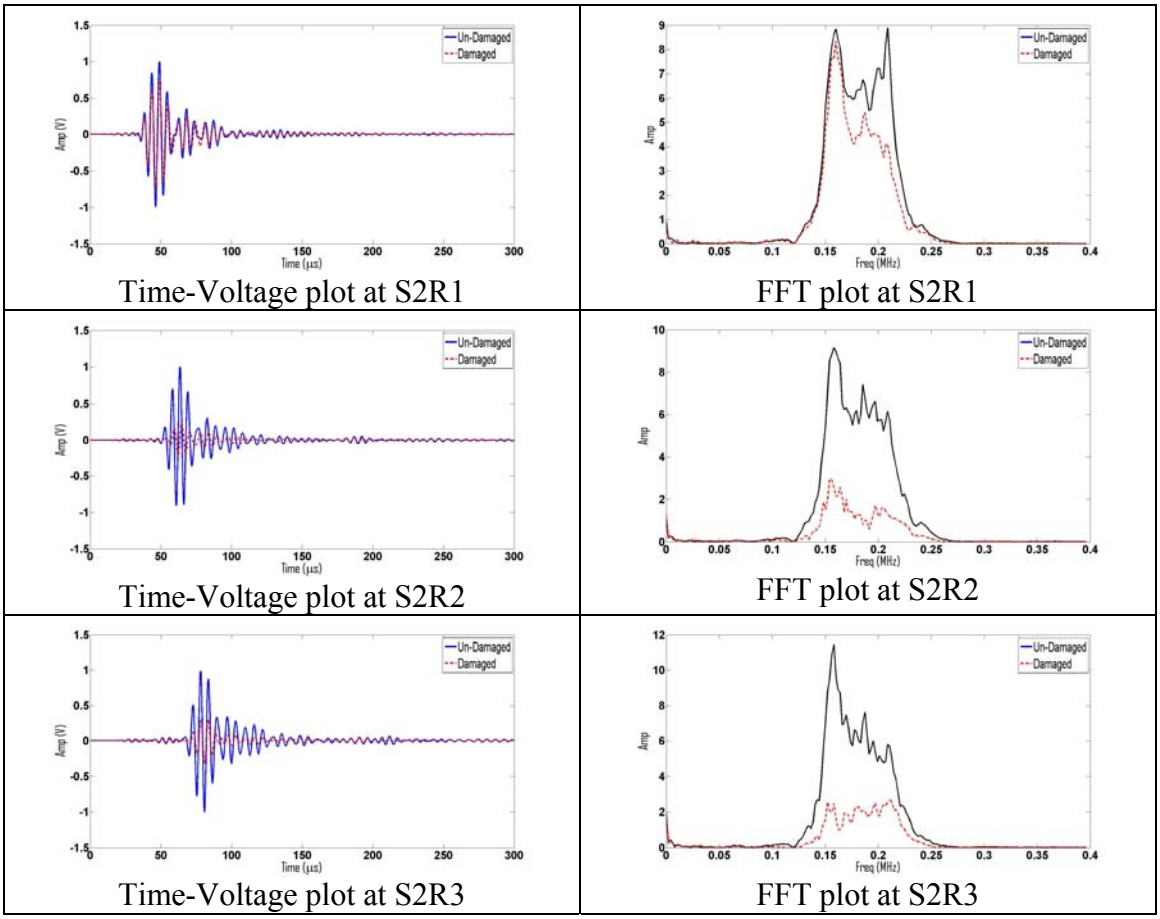

Time-Voltage plot at S2R1 | FFT plot at S2R1

Time-Voltage plot at S2R2 | FFT plot at S2R2

Time-Voltage plot at S2R3 | FFT plot at S2R3

Figure 4-8: Same as Figure 4-7 at locations S2R1, S2R2, and S2R3

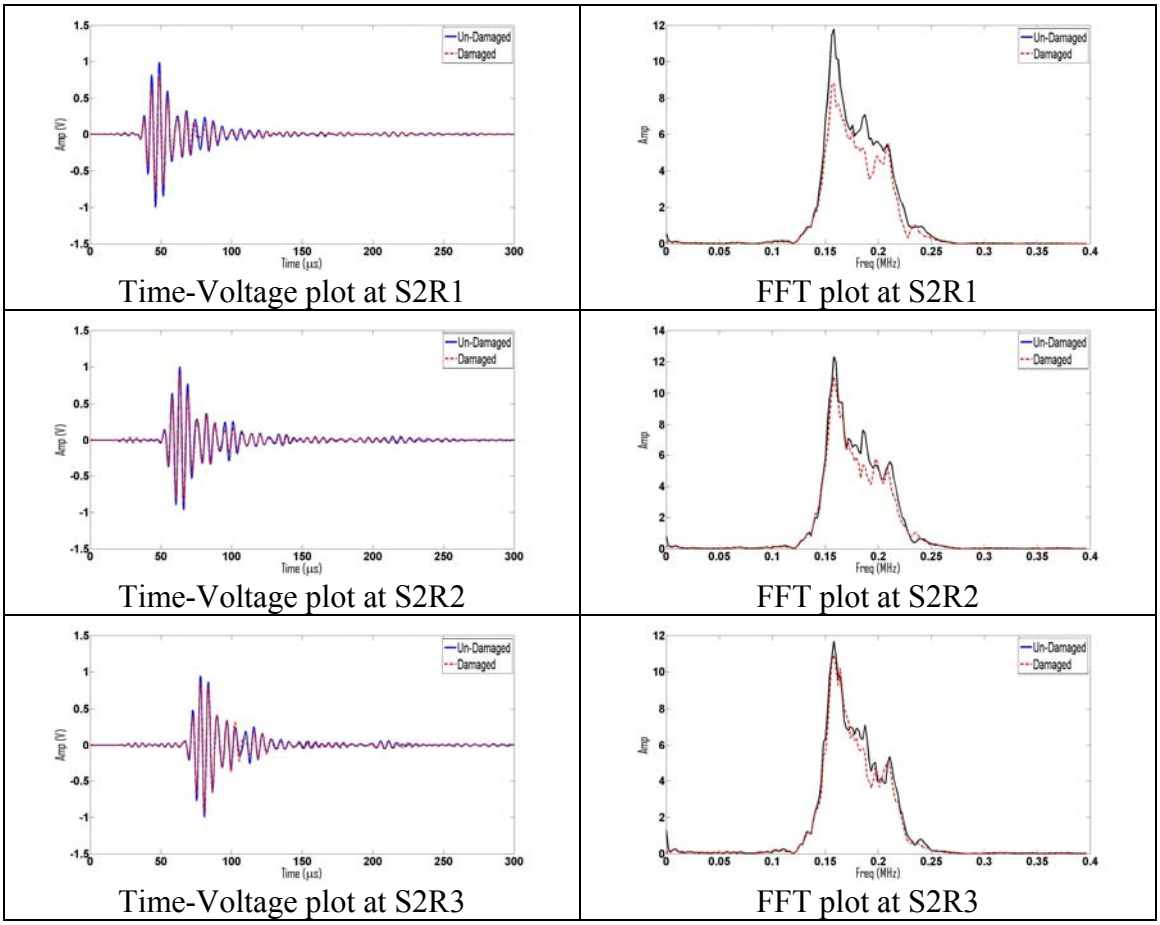

Time-Voltage plot at S2R1 | FFT plot at S2R1

Time-Voltage plot at S2R2 | FFT plot at S2R2

Time-Voltage plot at S2R3 | FFT plot at S2R3

Figure 4-9: Same as Figure 4-7 at locations S3R1, S3R2, and S3R3

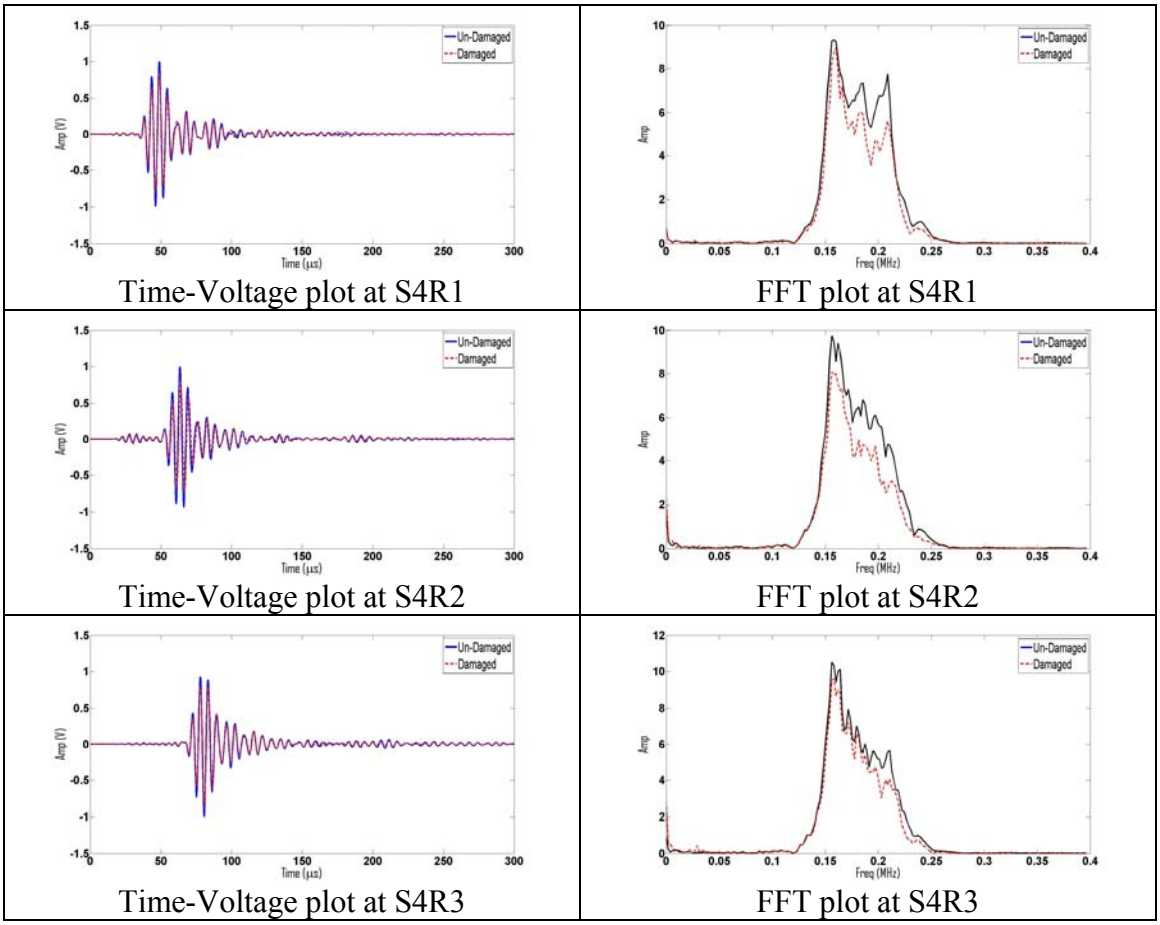

Time-Voltage plot at S4R1 | FFT plot at S4R1

Time-Voltage plot at S4R2 | FFT plot at S4R2

Time-Voltage plot at S4R3 | FFT plot at S4R3

Figure 4-10: Same as Figure 4-7 at locations S4R1, S4R2, and S4R3

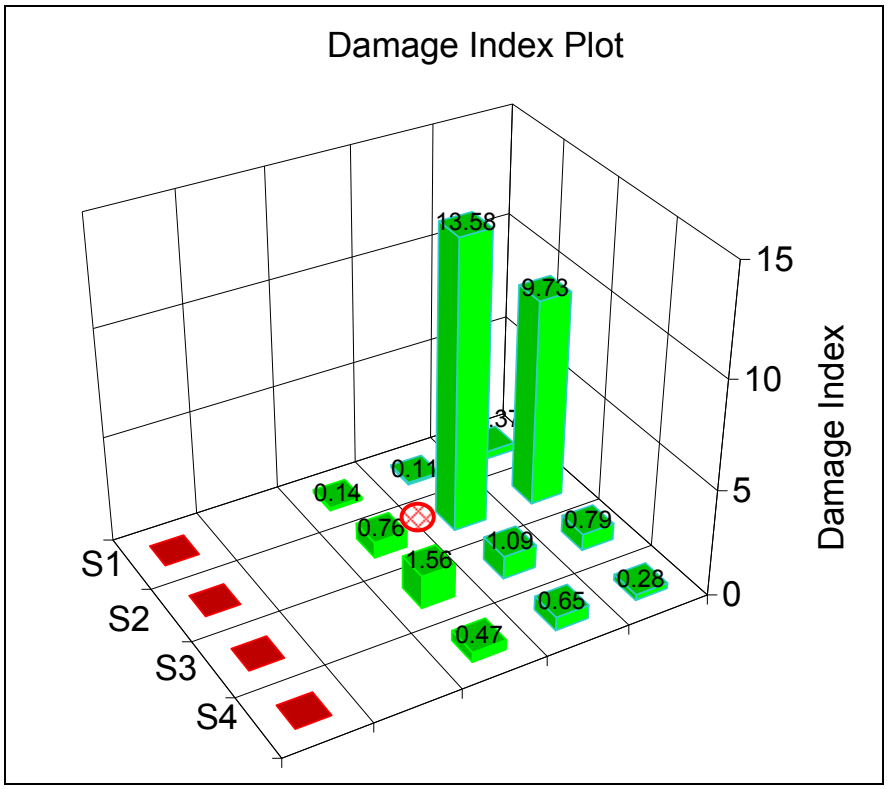

Figure 4-11: Damage Index at the receiver location for a single trial

Statistical Analysis

Experimental measurements can be affected by different operators, random errors or environmental noise that could affect damage detection, as their influence may lead to positive DI values. In order to correlate statistically the DI values to the presence of damage with a certain confidence level, a number (M) of frequency response functions (FRFs) are acquired in the "starting configuration" (without any structural damage, i.e. the baseline). One of these has been adopted as the reference and DI in equations (4.2) have been evaluated for the remaining M-1. Then, after damage occurs M FRFs related to the "damaged configuration" are acquired and the DI values are calculated using the FRF acquired in the healthy configuration. In the following tests M = 5 has been fixed and consequently 4 DIs have been obtained for the healthy configuration and 5 DIs for the damaged configuration. A coupled Student's Test has been

applied in order to verify that these "samples sets" belonged to different structural configurations with a confidence level of 99.5%. If the experimentally evaluated statistic *t*, defined in equation (4.3) below, is higher than the value obtained from the Student's distribution, then it is possible to assert that, with the chosen confidence level, the two data sets can be statistically associated with two different physical conditions (healthy and damaged), and consequently, the difference between the means of the sets is not casual. The statistic *t* is defined as follows:

$$t = \frac{\left|\overline{x}_1 - \overline{x}_2\right|}{\sqrt{A \cdot B}} \tag{4.3}$$

where,

$$A = \frac{n_1 + n_2}{n_1 \cdot n_2}, B = \frac{\left[\left(n_1 - 1\right) \cdot \sigma_1^2 + \left(n_2 - 1\right) \cdot \sigma_2^2\right]}{\left[n_1 + n_2 - 2\right]} \tag{4.4}$$

In the equations (4.3) and (4.4) $\overline{x}_1$ and $\overline{x}_2$ are the means of the two sets of DIs related to the healthy and damaged configurations, σ_1 and σ_2 are their standard deviations and n_1 and n_2 are the number of samples for the two sets. The number of "degrees of freedom," ν of the T-test is function of n_1 and n_2 ($\nu = n_1 + n_2 - 2$) and is related to the "confidence level" of each test. If $n_1 = 4$ and $n_2 = 5$, then $\nu = 8$, and for a confidence level of 0.995, $t_{0.995} = 3.355$. This means that if the t value calculated from equations (4.3) and (4.4) is greater than 3.355, then the difference between the means of the compared data sets is not casual but it is due to a structural disturbance. By using the proposed approach, it has been possible to identify very small damages with a high reliability level, and is shown in Figure 4-12.

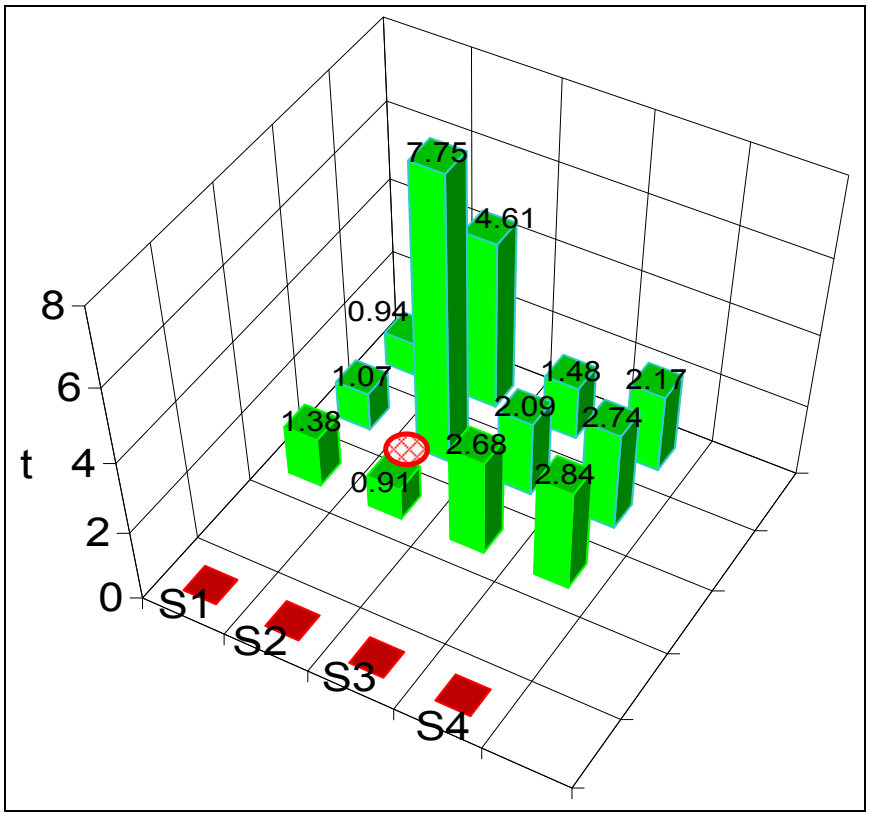

Figure 4-12: Statistic t evaluated for the damage index formulation (equation 4.3).

The damage index approach presented here can be used for detection and, under certain conditions, characterization of degradation in aircraft, aerospace and civil structures. It is clearly demonstrated that the damage indices are pronounced for the sensors located closer to the impact location. It should be noted that the method proposed here has a number of limitations. These include the inability for accurate localization and detailed characterization of the damage. Some of the limitations may be addressed through further research. In spite of these limitations, the present study clearly illustrates the potential effectiveness of the "damage-index" to predict the *approximate* location and severity of the impact. In addition, the effect of random noise and different operators was studied using a t-distribution. It is determined beyond a 99.5% confidence level that the higher damage indices near the impact were due to local changes in the FRFs.

Chapter 5 DAMAGE DETECTION IN A THICK ALUMINUM PLATE USING GUIDED WAVES

Due to the complexity of the honeycomb composite sandwich structure, a much simpler structure, namely, a thick aluminum plate is analyzed first to analyze the guided waves with and without damage. Guided wave propagation in the plate is investigated both numerically (finite element analysis) and experimentally. In the experiments, the elastic waves are generated by a broadband PZT transducer located on the plate surface and recorded by an identical transducer placed at different locations on the surface of the plate as well. The simulations are carried out using the finite element code ABAQUS for a two dimensional model of the problem to understand these features and to predict other expected features of the interaction process.

5.1 Guided Wave Propagation in a Thick Aluminum Plate

In this section the response of the thick aluminum plate to a dynamic load is calculated by means of the numerical (Finite Element) method. The aluminum plate considered here is a 12x12 inch (304.8x304.8 mm) squared plate with a thickness of 10 mm. The calculated waveforms are compared with those obtained from ultrasonic experiments using the test set up described in section 3.3

The general experimental setup used for the tests is shown in Figure 5-1 and described in section 3.3.

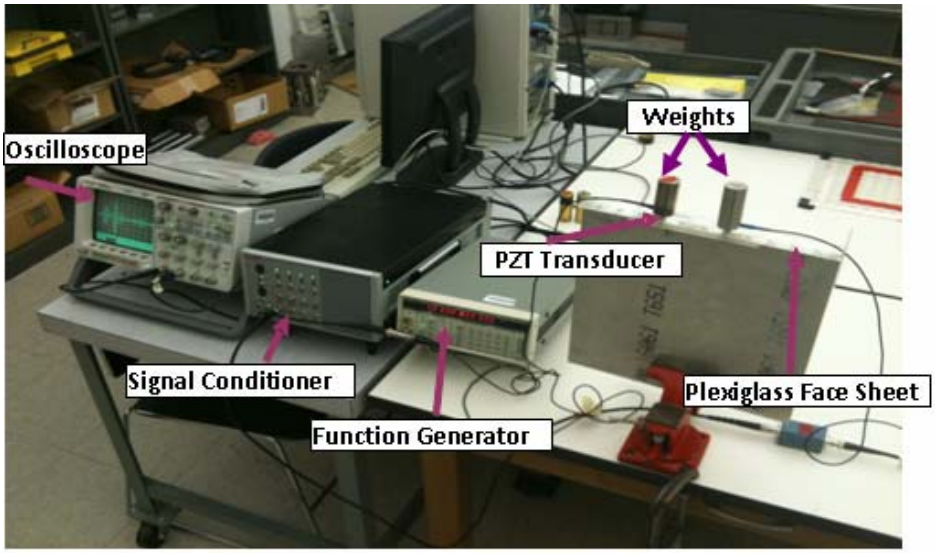

Figure 5-1: Experimental setup for ultrasonic NDE

Response data was created for the undamaged specimen. Figure 5-2 shows the distribution of transmitter and receiver sensors on the aluminium plate in the experiment. The red spot represents source location whereas the blue spots represent receiver location.

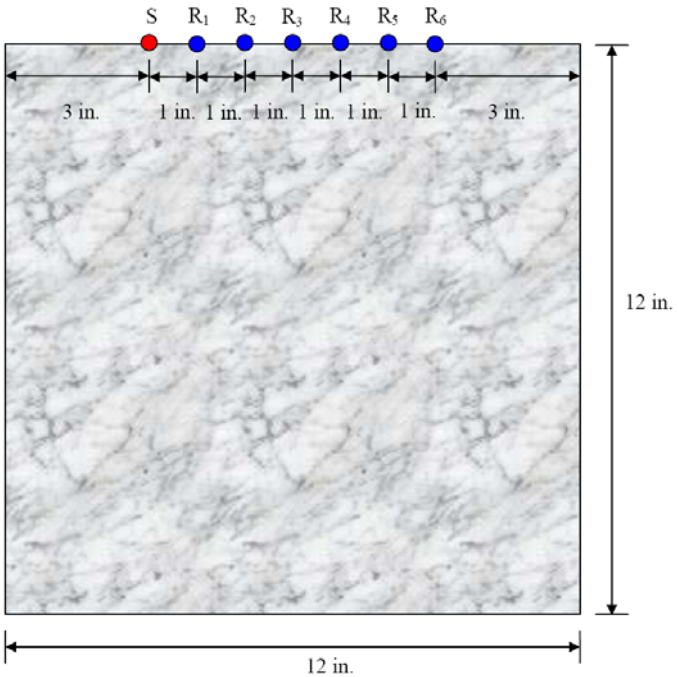

Figure 5-2: Source is fixed at S and receiver is moved from R_1 to R_6

A finite element simulation is carried out to determine the characteristics of guided waves in a plane-stress model of a 12x12 inch (304.8x304.8 mm) aluminum plate. The 12x12 inch (304.8x304.8 mm) plate was composed of a 1.78 mm thin plate and 303.03 mm thick plate. Both the plates were modeled separately and then assembled together. Surface-based tie constrains is used to connect the nodes at the interface. The 2-D plane stress finite element model of the aluminum plate contains 140,762 CPS4R elements (ABAQUS, 4-node bilinear plane stress quadrilateral, with reduced integration, hourglass control) and 663 CPS3 elements (ABAQUS, 3-node linear plane stress triangle) with 143,904 nodes. Modulus of elasticity (E) of 70.5 GPa, Poisson ratio (ν) of 0.33, and density (ρ) of 2800 kg/m^3 were used for both the plates. The model was supported to simulate the same boundary conditions as existed in the experiments. Both the displacement and rotation were fixed to zero at the bottom edge of the plate. As indicated earlier, the forcing function used in the FEA was the modified source incorporating the system response (Figure 5-4). Figure 5-3 shows the schematic of the 2-D model with appropriate boundary conditions, applied vertical source and receiver locations; red spot represents source locations and blue spots represent receiver locations. Vertical displacement on the surface of the plate were recorded at locations R_1, R_2, R_3, R_4, R_5 and R_6.

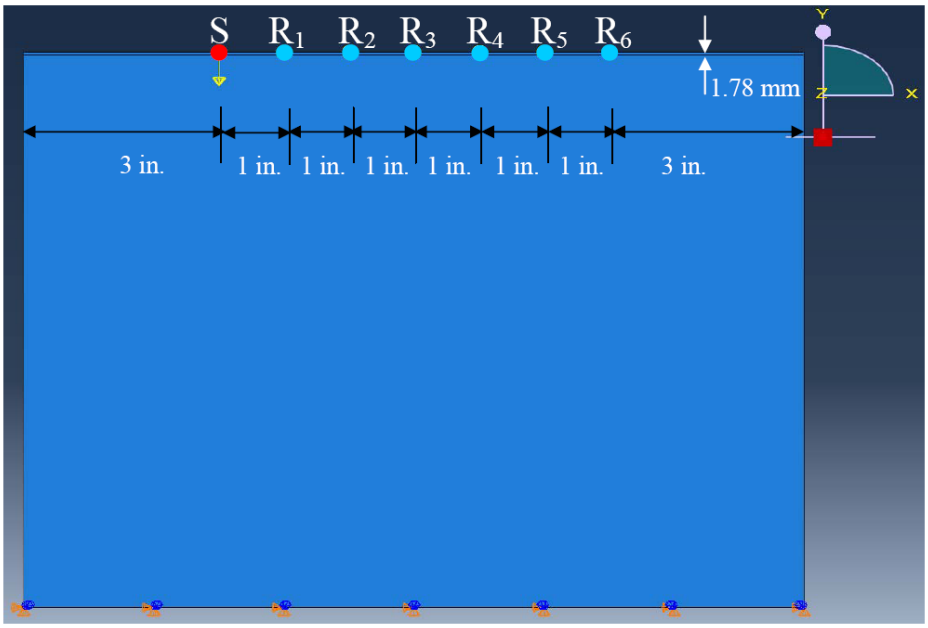

Figure 5-3: 2-D plane stress finite element model with applied vertical source and receiver positions.

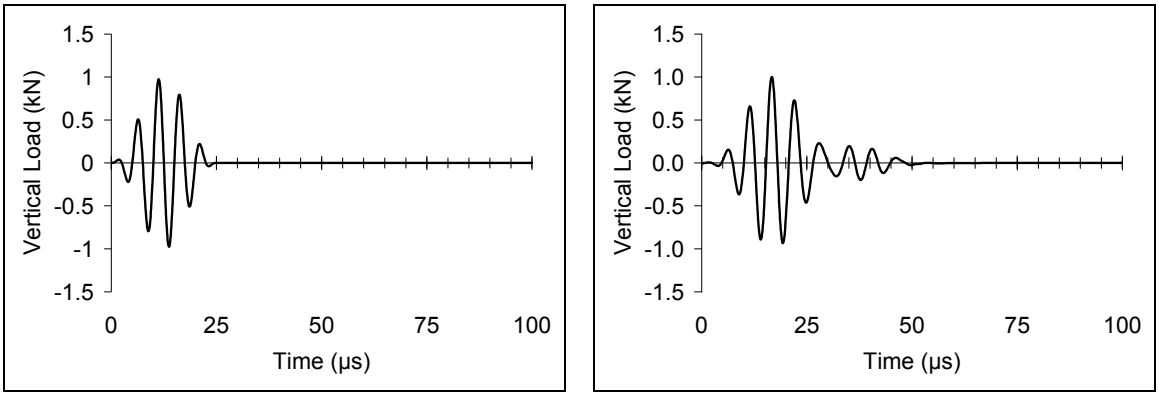

Figure 5-4: A narrow band pulse - central frequency 200 kHz (a) Actual Signal (left) (b) Modified Signal (right)

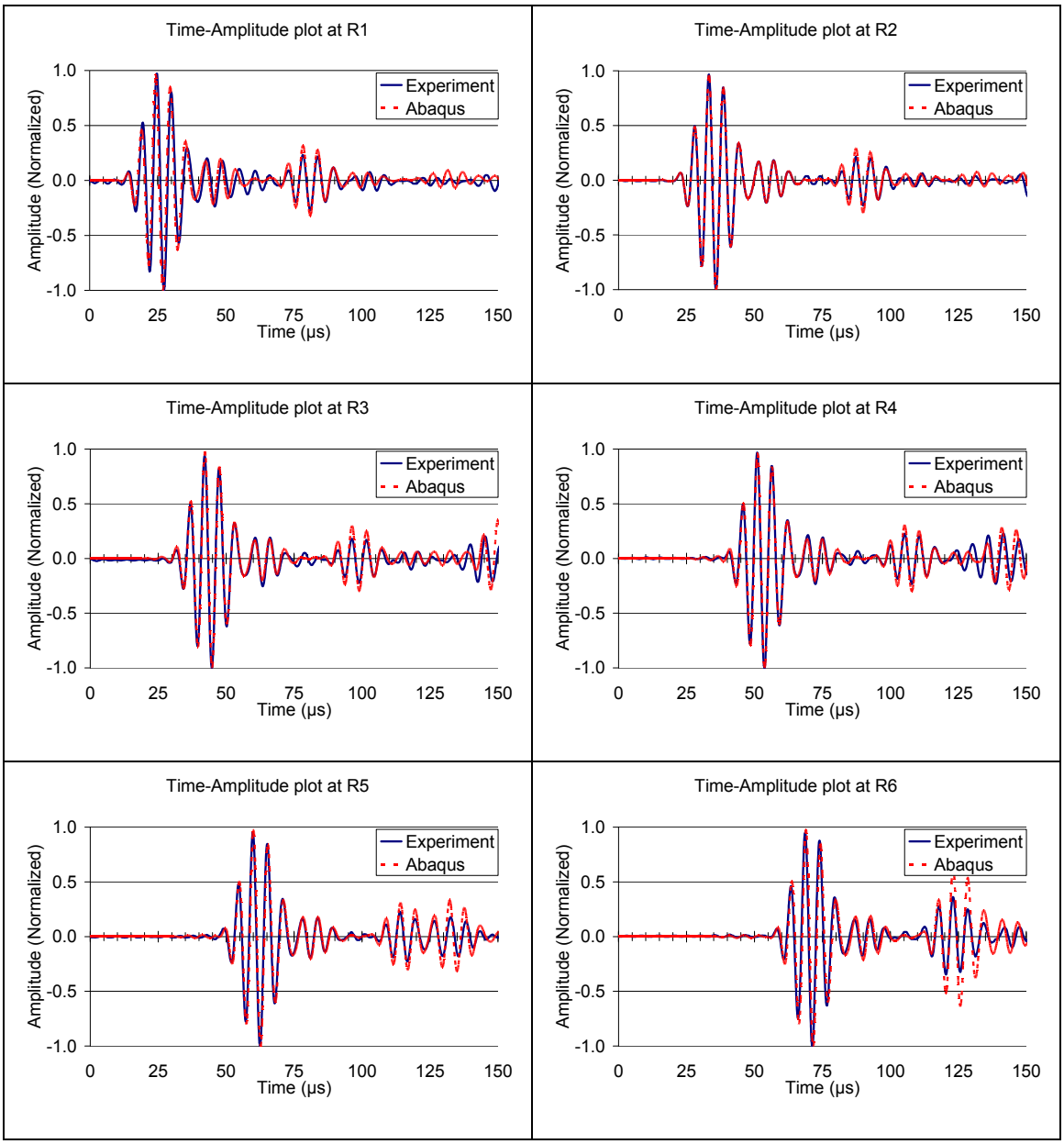

Figure 5-5: Experimentally and numerically obtained signals at 1-6 inches (25.4 mm - 152.4 mm) in the thick aluminum plate.

From Figure 5-5, it is evident that the results obtained from finite element simulation agrees very well with those obtained in the experiment.

5.2 Guided Wave Propagation in a Thick Aluminum Plate with a Crack

In this section we use the experimental and finite element approaches to understand the interaction of guided waves in the thick aluminum plate with a crack. In this case a crack of length 25.4 mm (1 inch) with left tip located at 63.5 mm (2.5 inches) from the source location and 1.78 mm (0.07 inches) from top surface as shown in Figure 5-6 was introduced in the test sample using an EDM equipment.

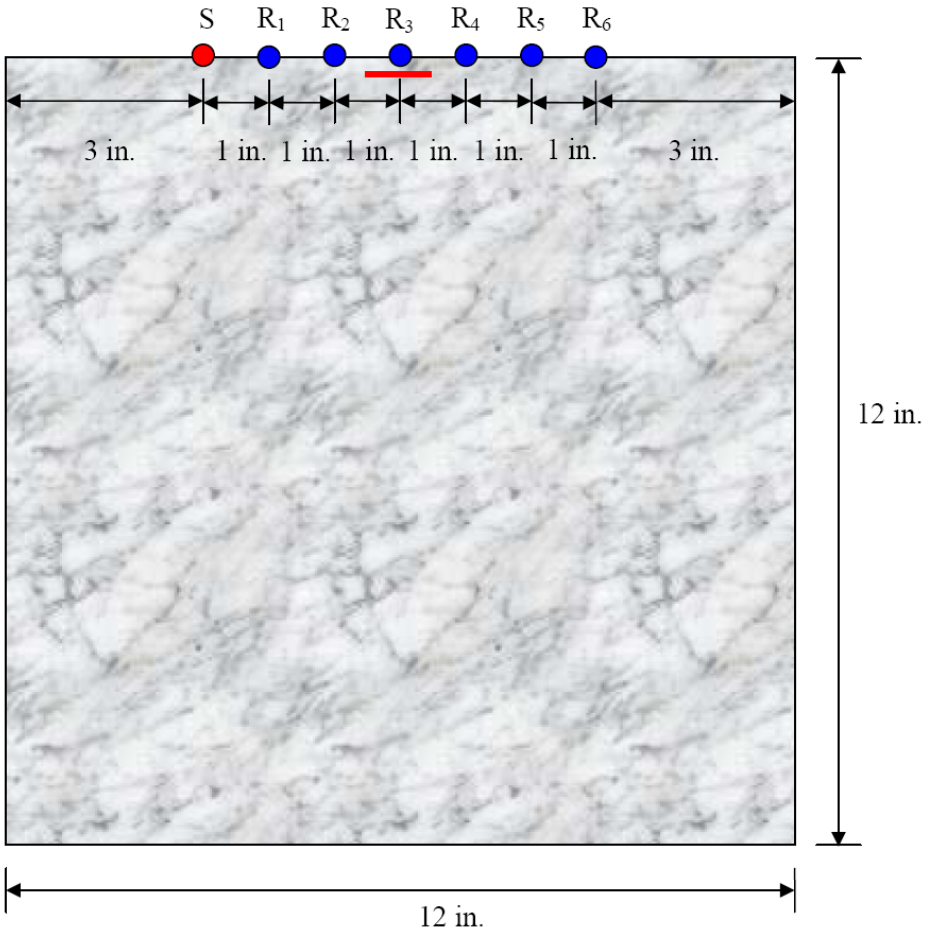

Figure 5-6: Source is fixed at S and receiver is moved from R_1 to R_6

Experimentally obtained responses for undamaged and damaged cases at receiver locations is shown in Figure 5-7.

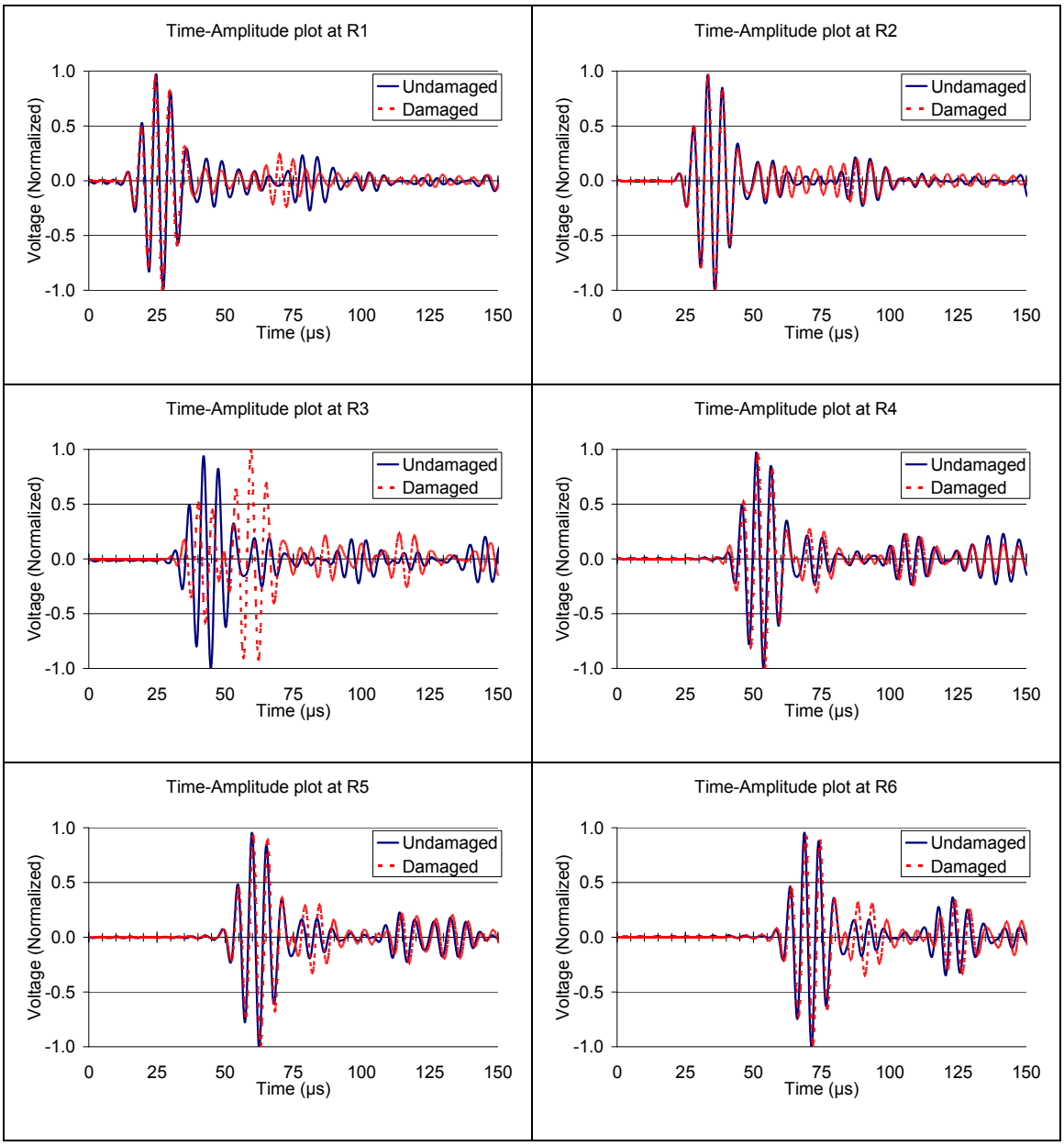

Figure 5-7: Time-voltage plots for undamaged and damaged cases in a thick aluminum plate obtained experimentally

The response at receiver locations 1 and 2 did not show any significant changes in the waveform, especially the first part of the wave. Receiver location 3, which is located right on the top of the crack, showed a significant change in the first part of the wave. At locations 4, 5, and 6 in the damaged case there was a delay in the signal. Time-voltage plot at locations R_2 through R_6 is magnified in Figure 5-8 to view the significant change in the delay of the signal.

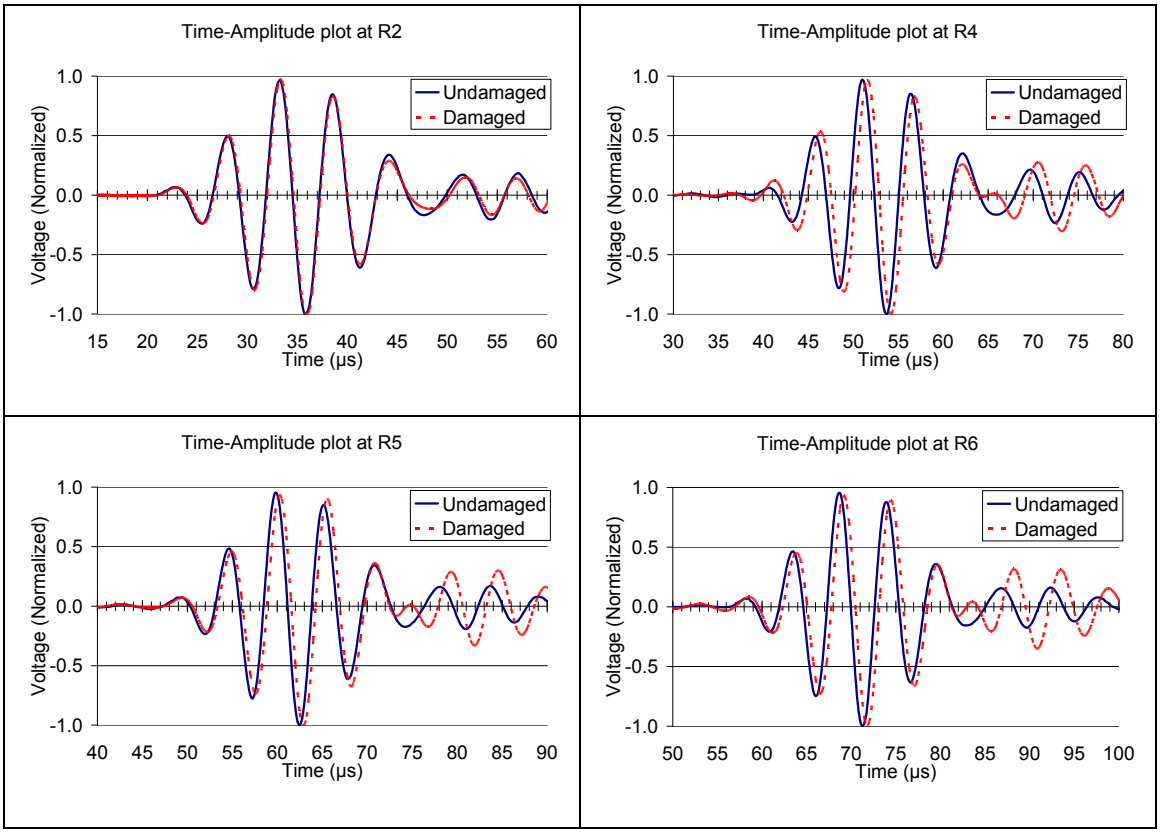

Figure 5-8: A magnified view of time-voltage data for undamaged and damaged cases in the thick aluminum plate

Similar to section 5.2, a finite element simulation is carried out to determine the characteristics of the guided waves in a plane-stress model of the aluminum plate with a disbond between the top and the bottom layer. In order to mimic the crack from the experimental case the disbond

between the top and the bottom layer was generated by suppressing the surface-based tie bonds at the same location, introducing discontinuity between the two layers. For the finite element simulation, the surface response for both undamaged and damaged case at receiver locations is shown in Figure 5-9.

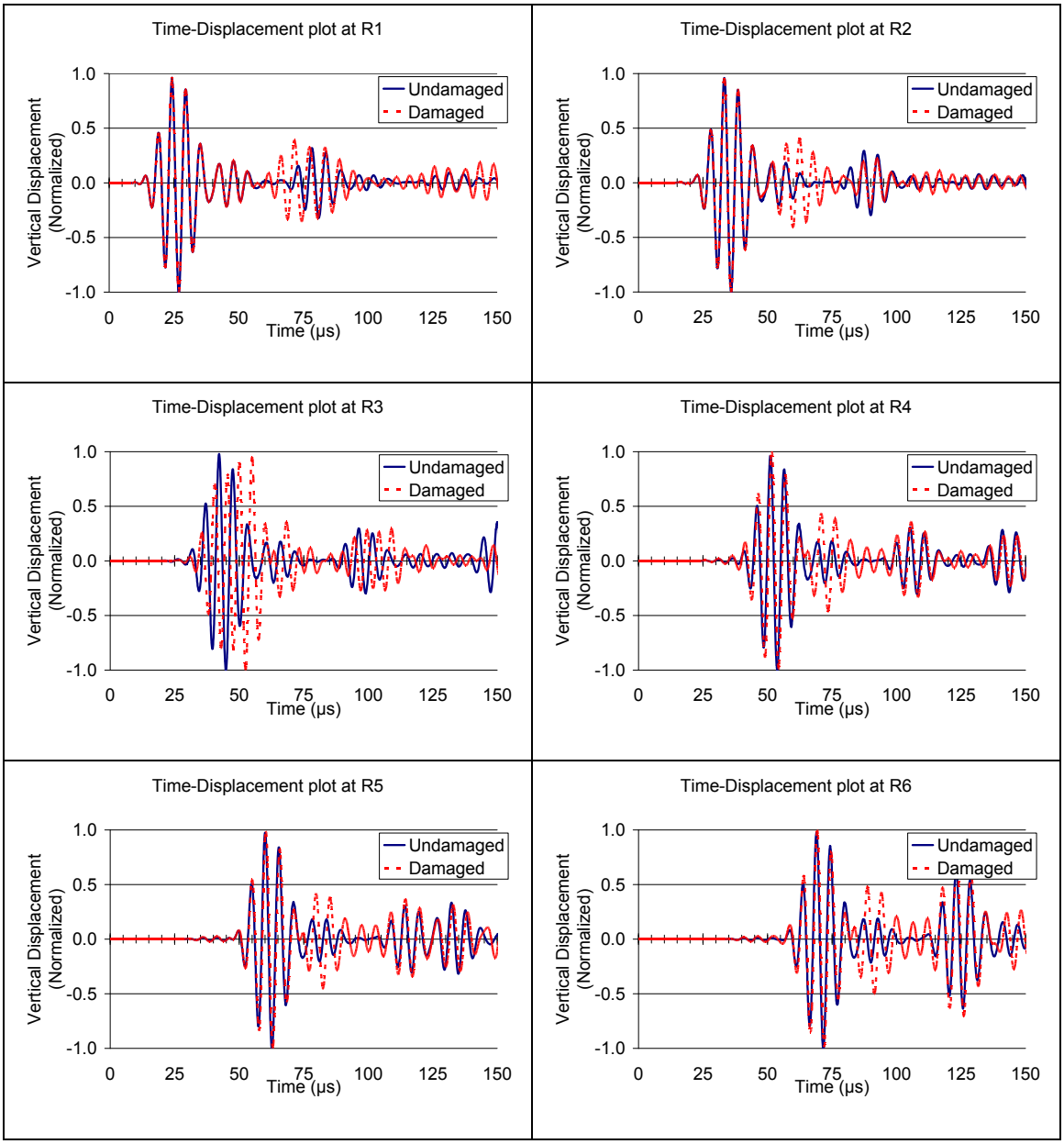

Figure 5-9: Time-voltage plots for undamaged and damaged case in a thick aluminum plate obtained numerically

As in the experiment the response at receiver locations 1 and 2 did not show significant changes especially the first part of the waveform. Receiver location 3, which is located on the top of the crack, showed a significant change in the first part of the wave. At locations 4, 5, and 6 for the damage case, there is a delay in the signal. Again time-displacement plot at locations R_1 through R_6 is magnified to view the significant change in the delay of the signal.

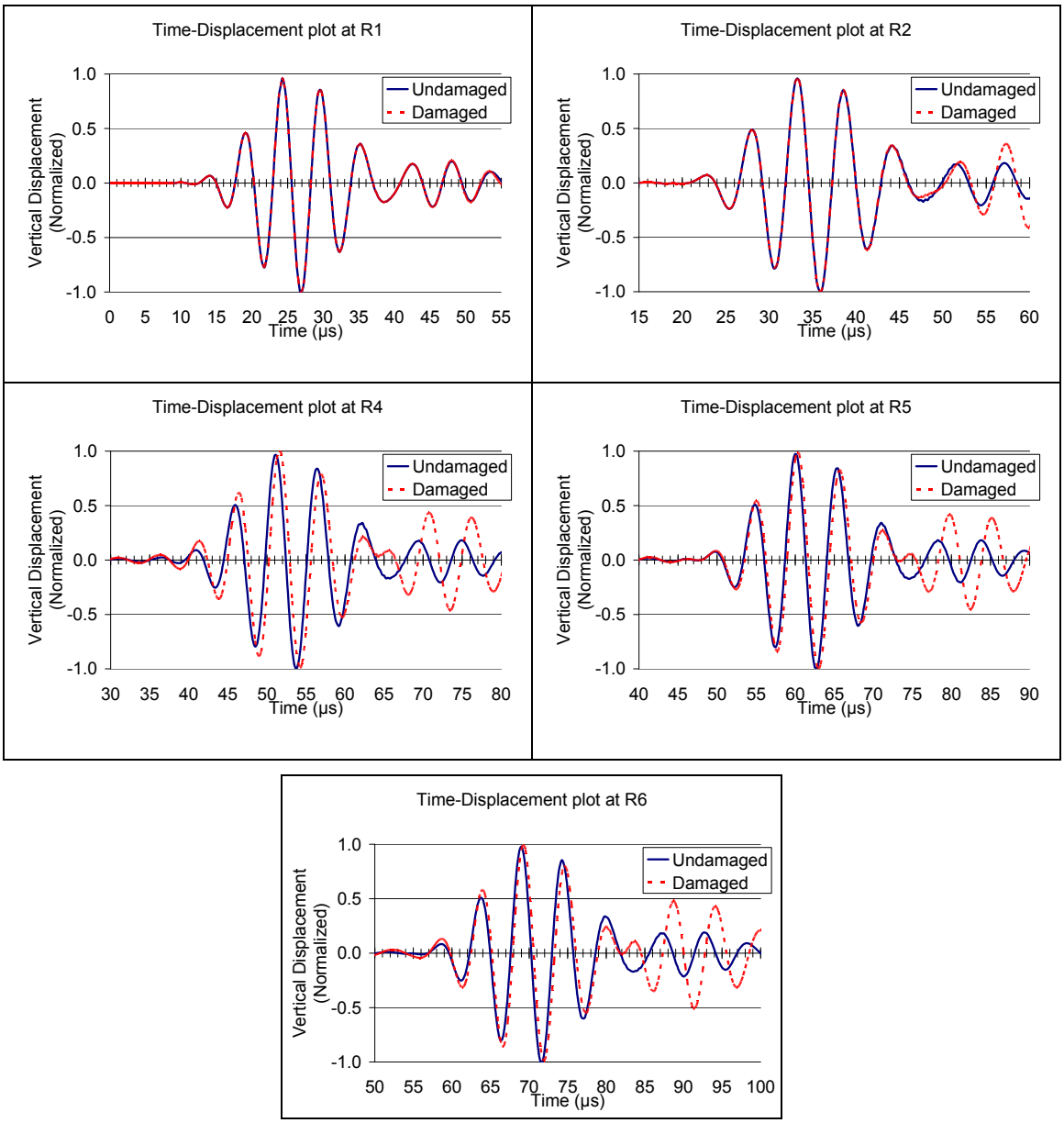

Figure 5-10: A magnified view of time-voltage plots for undamaged and damaged cases in the thick aluminum plate obtained numerically

It can be seen that as a result of the interaction between the propagating waves and the disband-like crack, there is a delay in the signal. The simulations carried out using the finite element code ABAQUS for a two dimensional model of the problem provides a clear understanding of this feature and also predict other expected features of the interaction process. Examples of the simulated displacement field with and without damage at different time intervals are presented in Figure 5-11 and Figure 5-12. A more detailed image of wave interaction with damage is shown in Figure 5-13 and Figure 5-14. It is evident that as the wave profile encounters the disbonded region, it splits in two parts, with one traveling in the disbonded upper layer and the other below it. The delay in the signal is due to the slower propagation speed in the upper layer.

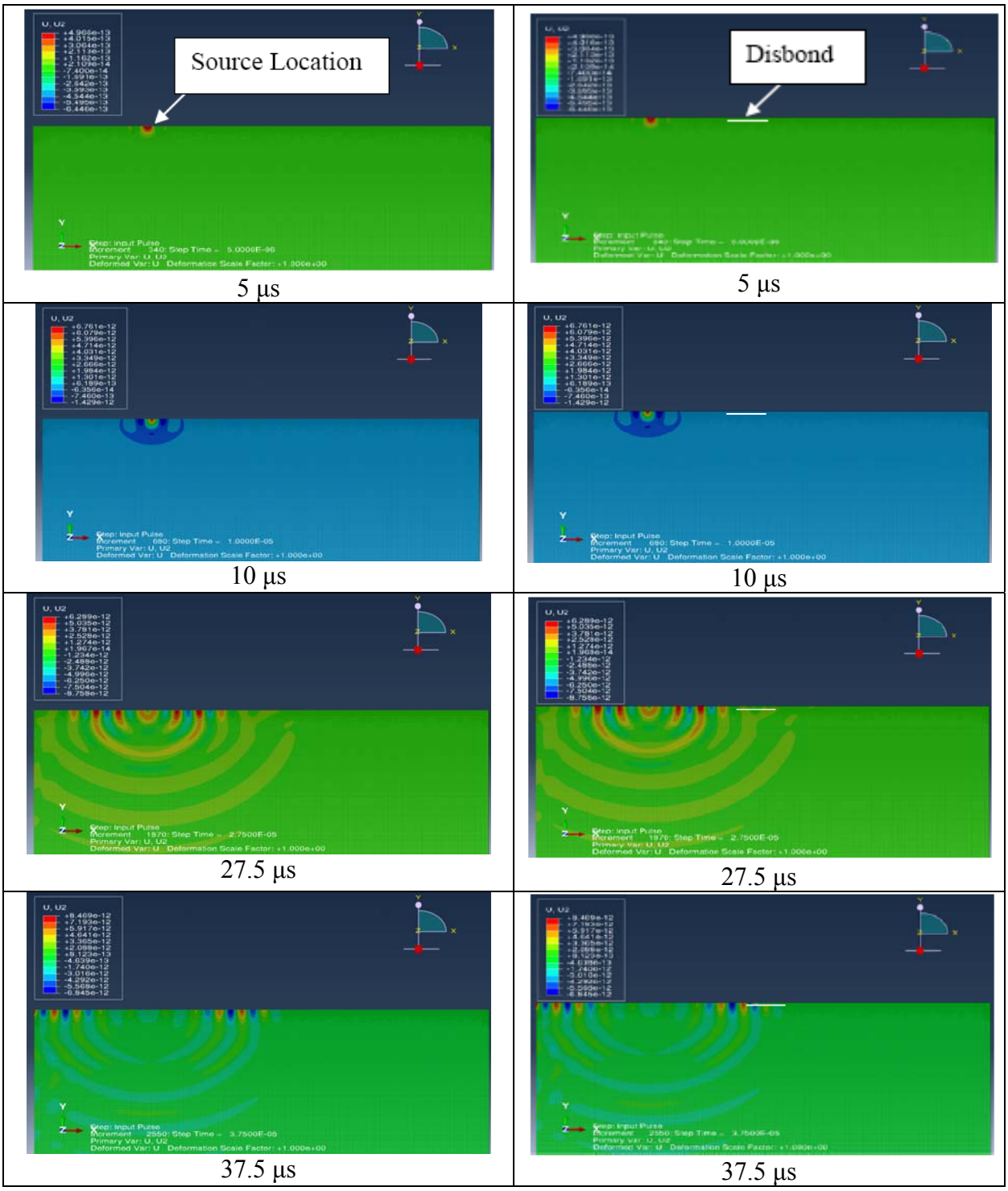

Figure 5-11: Contour plot of vertical displacement profile in an undamaged and damaged aluminum plate at time intervals for 5 µs to 37.5 µs

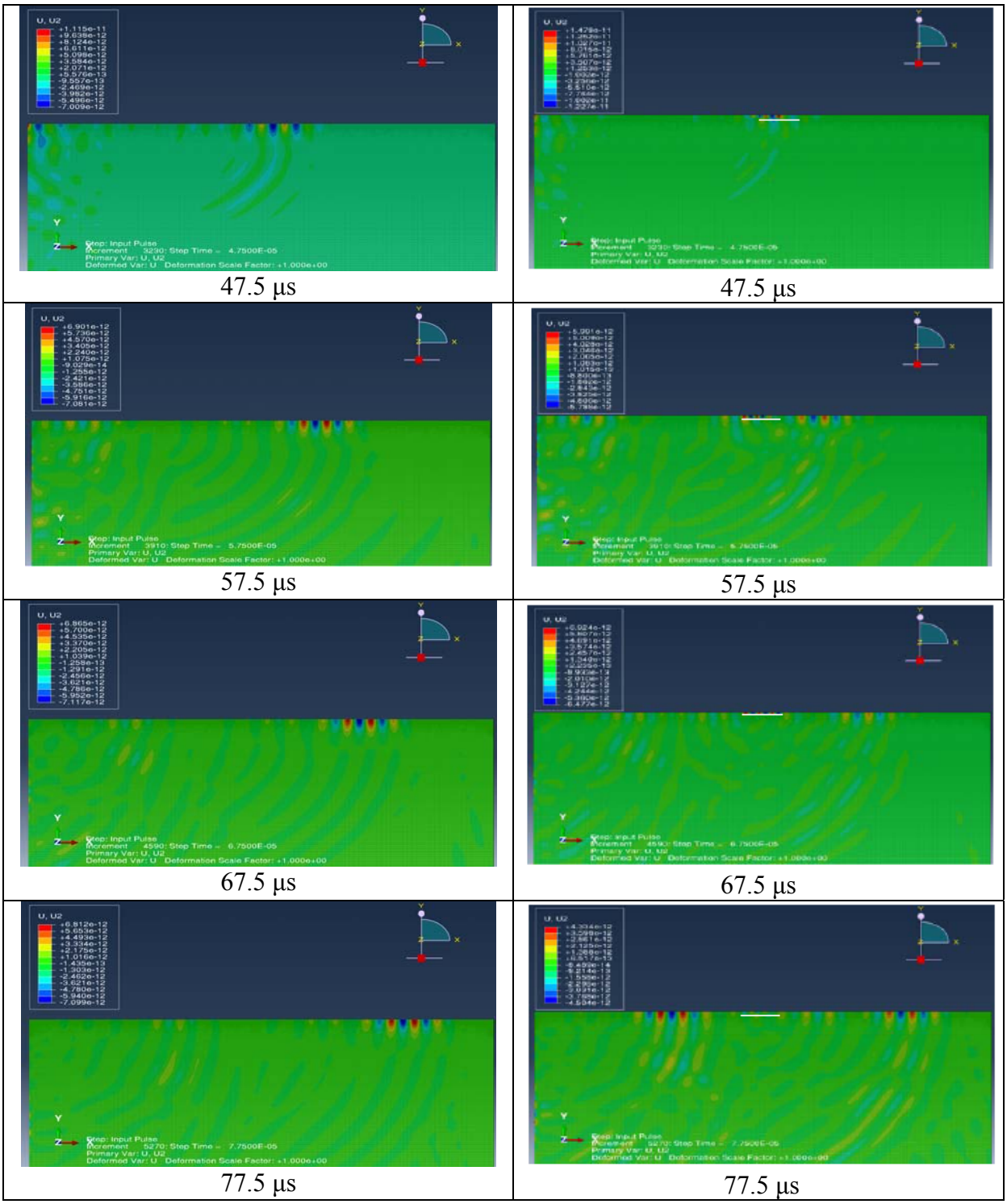

Figure 5-12: Same as Figure 5-11 at time intervals for 47.5 µs to 77.5 µs

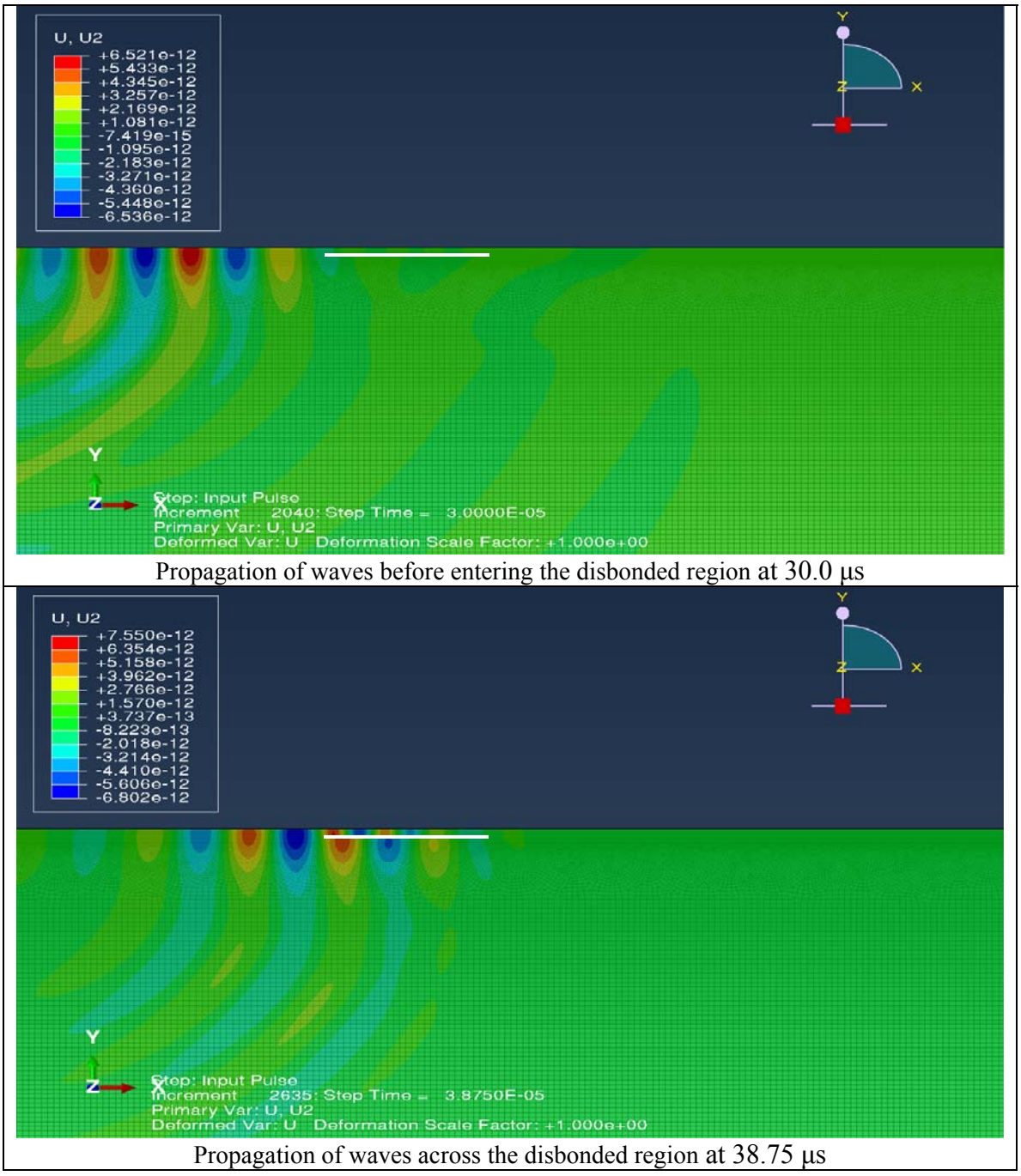

Figure 5-13: Contour plot of detailed vertical displacement profile in a damaged aluminum plate at 30 µs and 38.7 µs

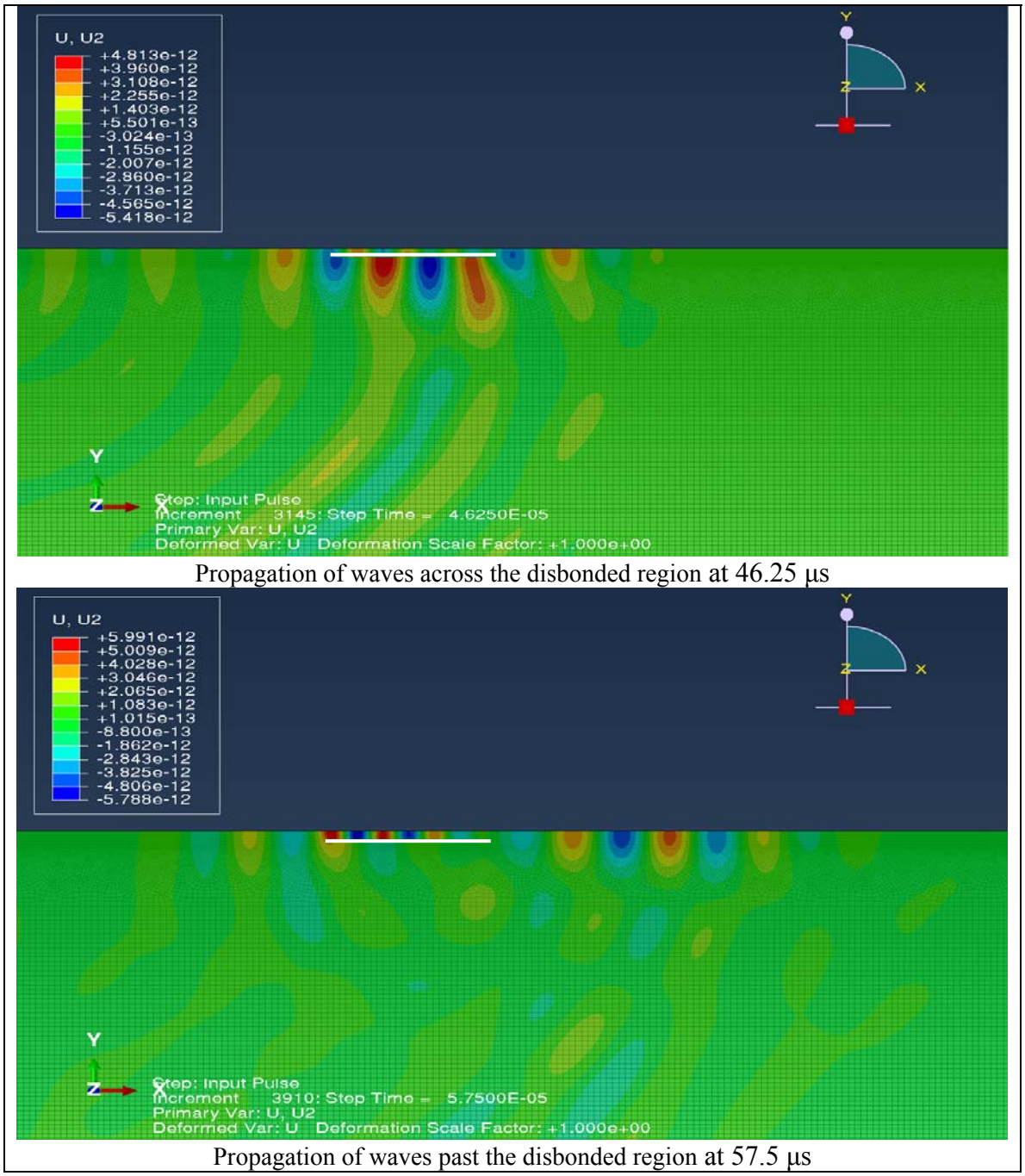

Propagation of waves across the disbonded region at 46.25 μs

Propagation of waves past the disbonded region at 57.5 μs

Figure 5-14: Same as Figure 5-13 at 46.25 μs and 57.5 μs

Chapter 6 DAMAGE DETECTION IN A HONEYCOMB COMPOSITE STRUCTURE USING GUIDED WAVES

Guided wave propagation in sandwich plate is investigated numerically (finite element analysis) and experimentally using wave propagation approach. The sandwich plate consists of a 12.7 mm thick aluminum honeycomb core sandwiched between two 1.78 mm thick 2/2 twill woven composite panels. The equivalent cell diameter of the core is about 5.5 mm. Due to the relatively low frequencies used in this work, both materials can be assumed to be transversely isotropic with a common symmetry axis normal to the plate. The elastic properties of the composite and the honeycomb were determined using a combination of mechanical and ultrasonic tests as discussed in Chapter 2. For the damaged case a disbond at the skin-core interface is assumed to be present. In the experiments, the elastic waves are generated by a broadband PZT transducer located on the plate surface and recorded by an identical transducer placed at different locations on the surface of the plate (Figure 3-6). The simulations are carried out using the finite element code ABAQUS for a two dimensional model of the problem to understand these features and to predict other expected features of the interaction process.

6.1 Guided Wave Propagation in a Honeycomb Composite Sandwich Structure

In this section we use both experimental and finite element approaches to understand the propagation of guided waves in honeycomb composite sandwich structure. Similar to section 5.1 for the experimental part an improved ultrasonic test setup consisting of distributed, high fidelity sensor array is used to determine the propagation of waves in the structure. A computer model using the Finite Element Method is used to calculate the waveforms of the propagating waves in

the sandwich structure and the results are compared with the experimental data. In the next section an artificially generated debonding is introduced between the skin-core interface and the changes in the dynamical properties of the sandwich structure with the appearance of disbond is analyzed using experimental and numerical methods.

The general experimental setup used for the test is shown in Figure 3-6 and the details can be found in section 3.3.

First baseline ultrasonic response data (time-voltage) is obtained in a region which is known to have no damage. Figure 6-1 shows the top view of distribution of transmitter and receiver sensors on the sandwich plate. The red spots represent source locations whereas the blue spots represent the receiver locations. The row containing S1 as source is assumed to be the undamaged region.

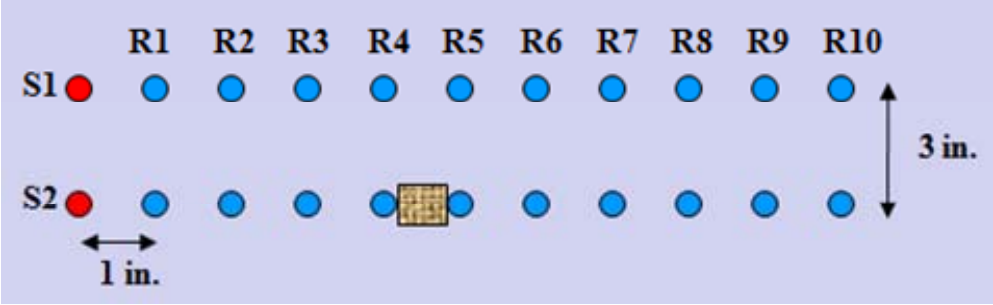

Figure 6-1: Source is fixed at S and receiver is moved from R_2 to R_7

A finite element simulation described in section 3.7 is carried out to determine the characteristics of Lamb waves in a three-layered plane-strain model of the sandwich plate. Guided wave propagation was activated in the sandwich structure using a waveform of modified source given in equation (3.24) with central frequency 200 kHz (Figure 6-3). Figure 6-2 shows

the schematic of the 2-D model with appropriate boundary conditions and applied vertical source and receiver locations. The dynamic simulation was accomplished using the ABAQUS/EXPLICIT® code. The vertical displacements on the surface of the plate were obtained at locations R_2, R_3, R_4, R_5, R_6 and R_7.

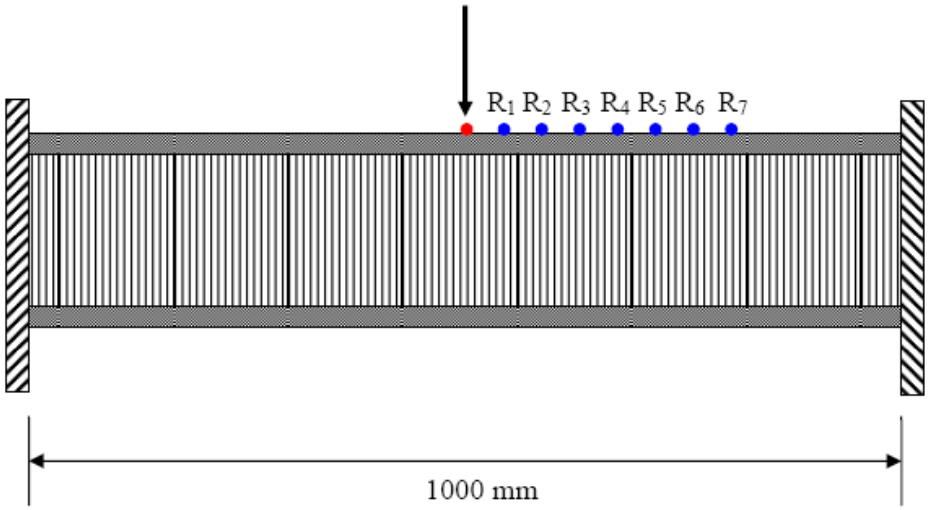

Figure 6-2: Schematic of the 2-D model of sandwich structure with applied load and the receiver positions.

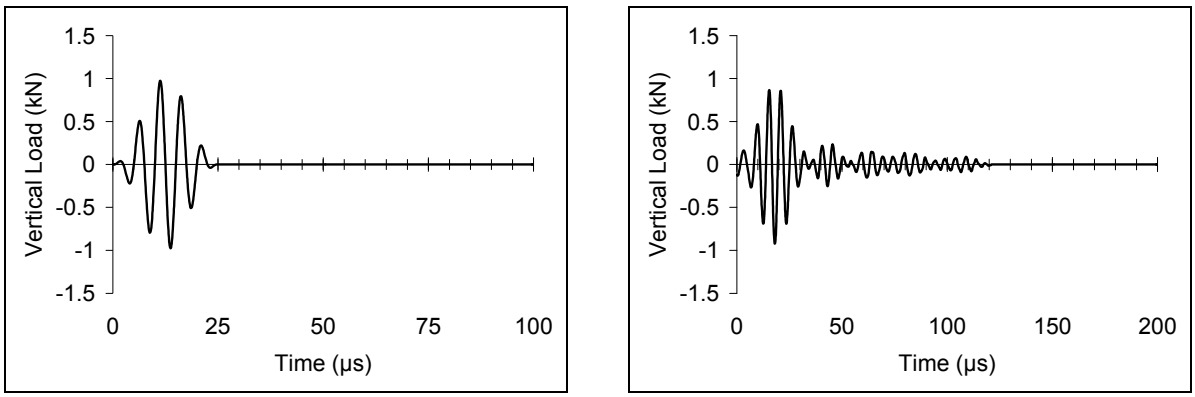

Figure 6-3: A narrow band pulse - central frequency 200 kHz (a) Actual Signal (left) (b) Modified Signal (right)

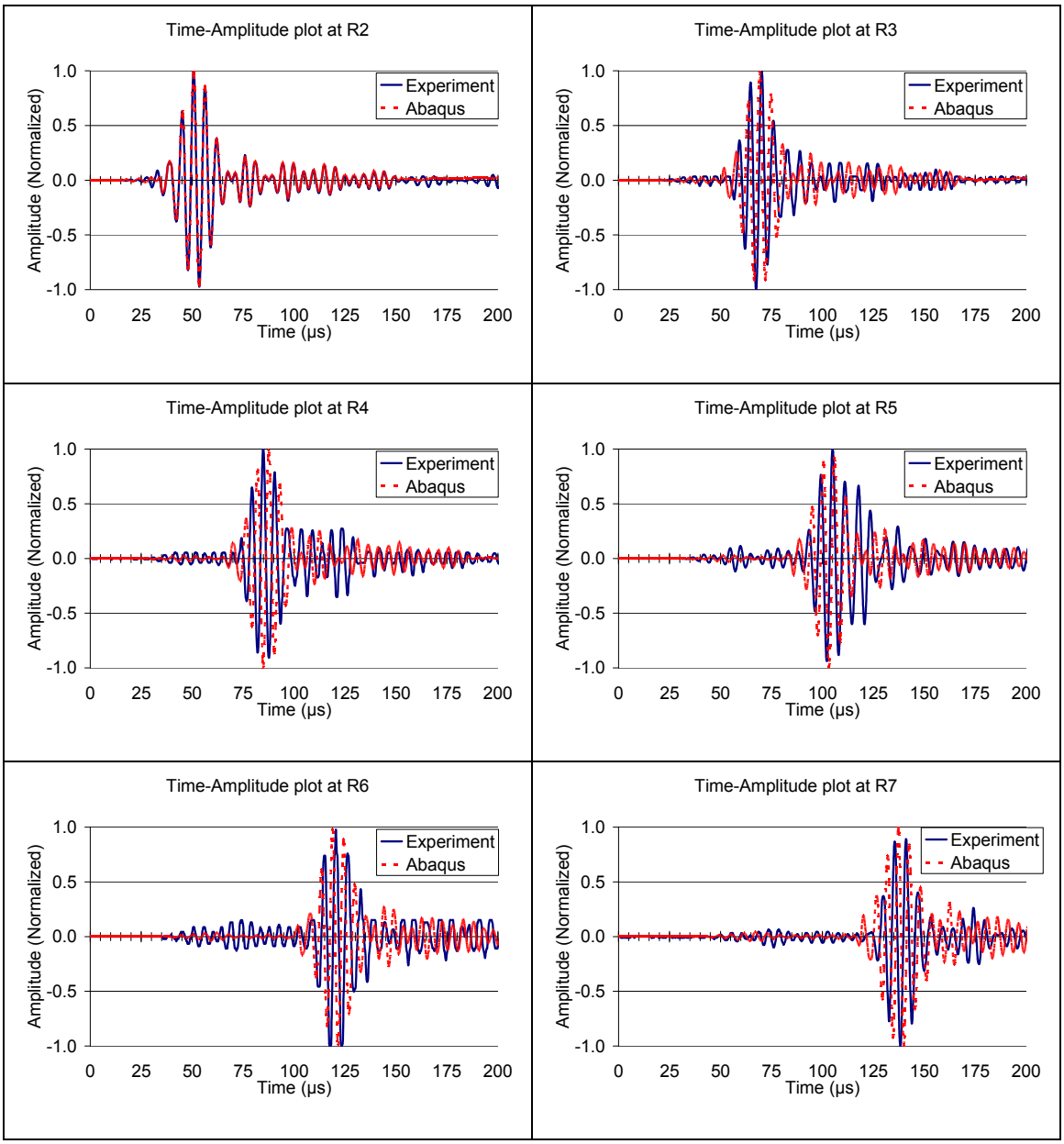

Figure 6-4: Experimentally and numerically obtained time-amplitude plot of the received signals at 1-6 inches (25.4 mm - 152.4 mm) in the sandwich plate.

It should be noted that the model of the honeycomb composite used in the finite element simulation is highly idealized. However, in spite of this, the main features of the signals in the finite element simulation match quite well with those obtained experimentally.

6.2 Guided Wave Propagation in a Honeycomb Composite Sandwich Structure with Disbond

In this section we consider the problem of guided wave propagation in the sandwich structure with a disbond between the composite face sheet and the aluminum core. The disbond was created by inserting a thin piece of teflon during the manufacturing of the sandwich plate. The experimentally obtained time-voltage surface response for both undamaged and damaged regions at receiver locations due to the modified five-cycle sine pulse with 150 kHz and 200 kHz central frequencies are shown in Figures 6-5 through 6-8.

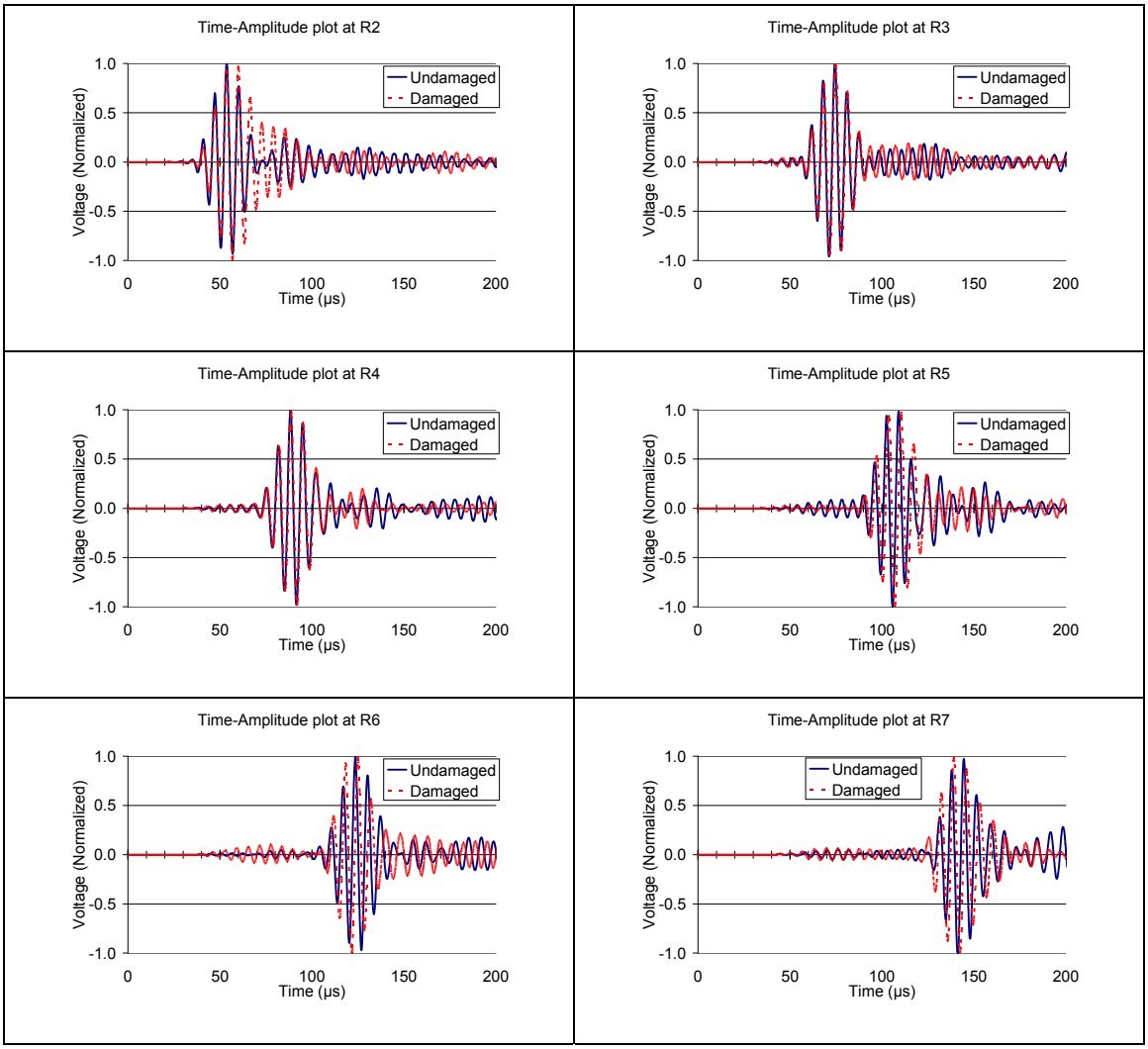

Figure 6-5: Received signals for undamaged and damaged cases in the sandwich structure at 150 kHz central frequency obtained experimentally

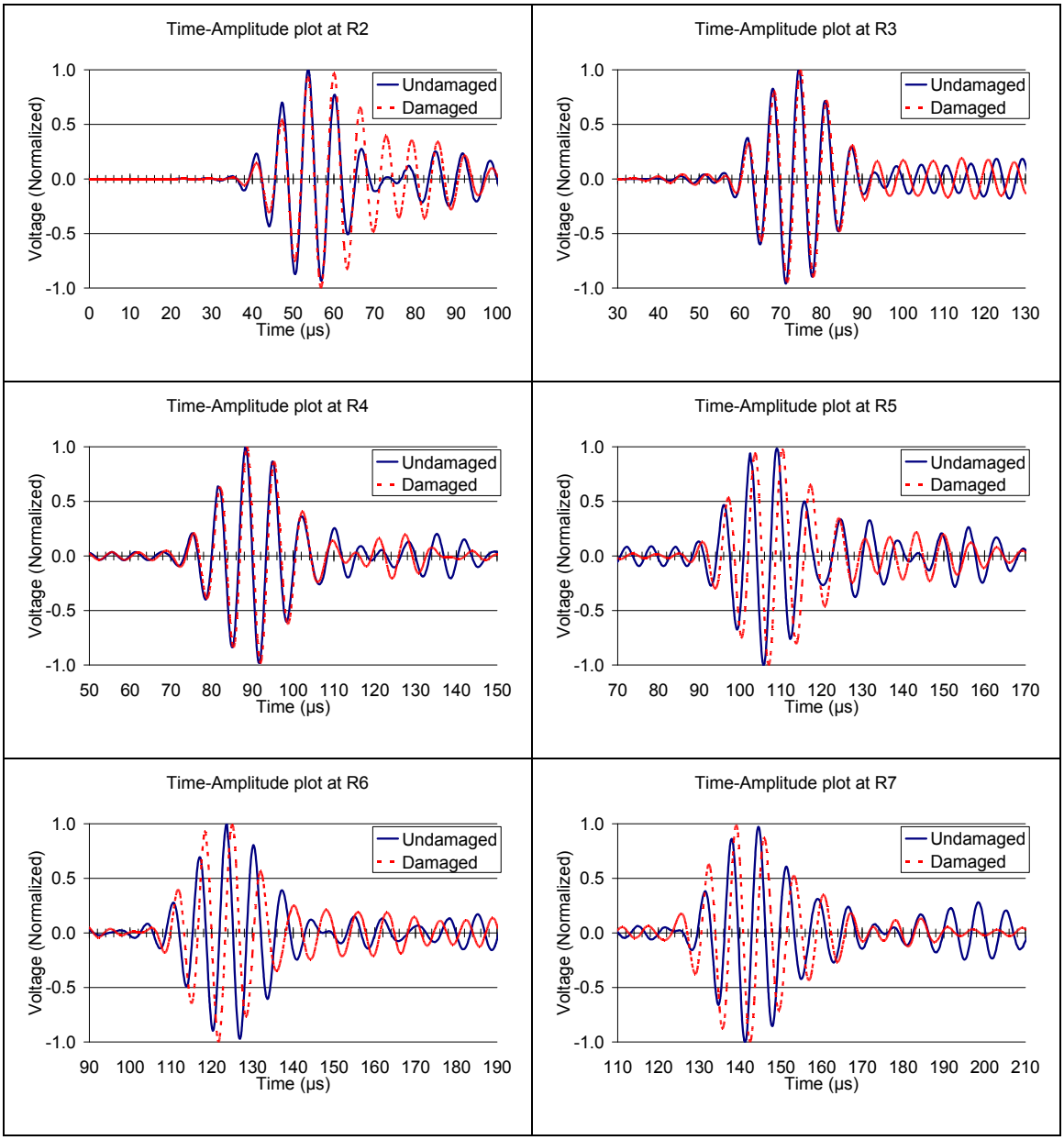

Figure 6-6: A magnified view of time-voltage plots for undamaged and damaged cases in the sandwich structure at 150 kHz central frequency obtained experimentally

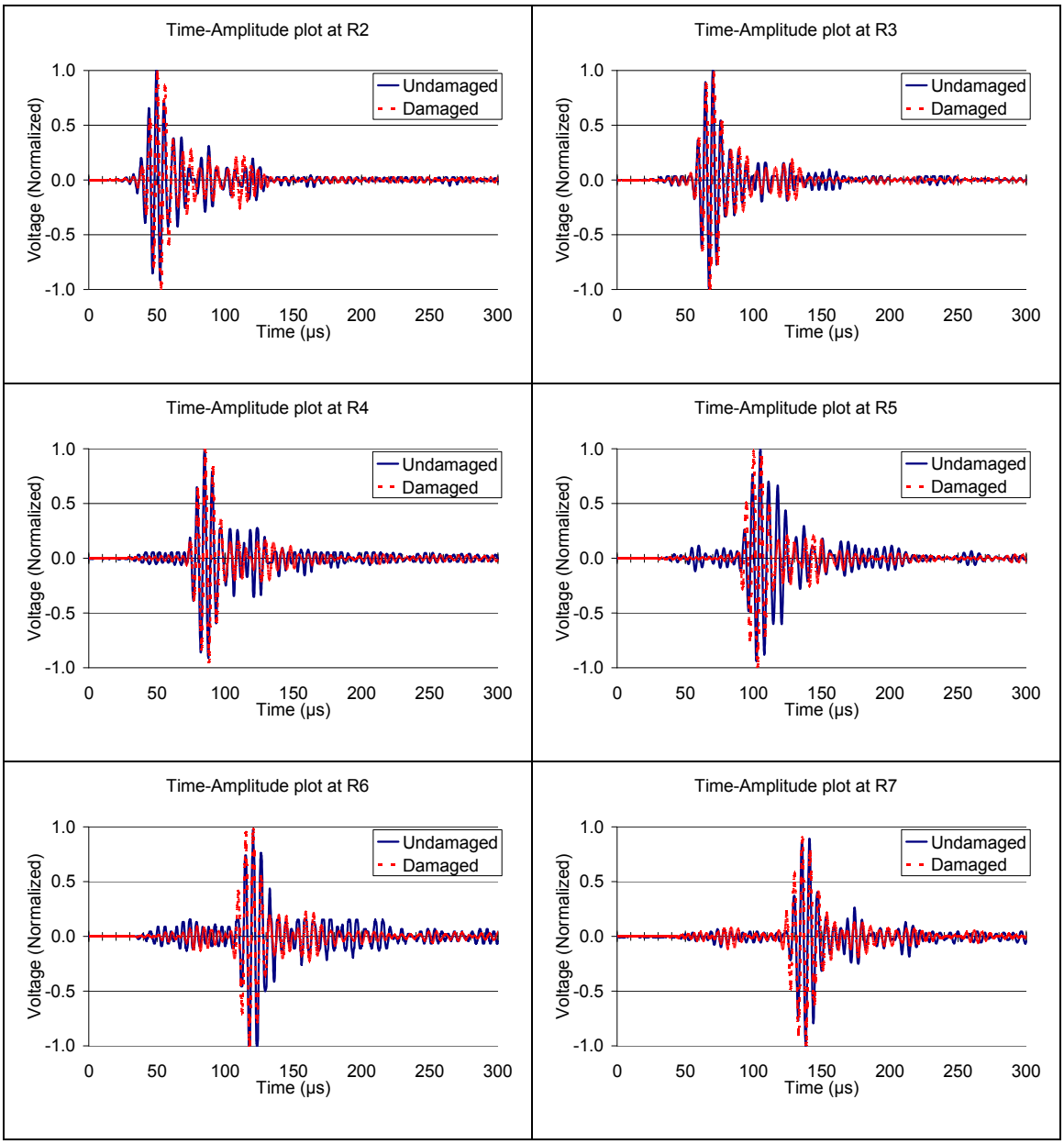

Figure 6-7: Time-voltage plots for undamaged and damaged cases in the sandwich structure at 200 kHz central frequency obtained experimentally

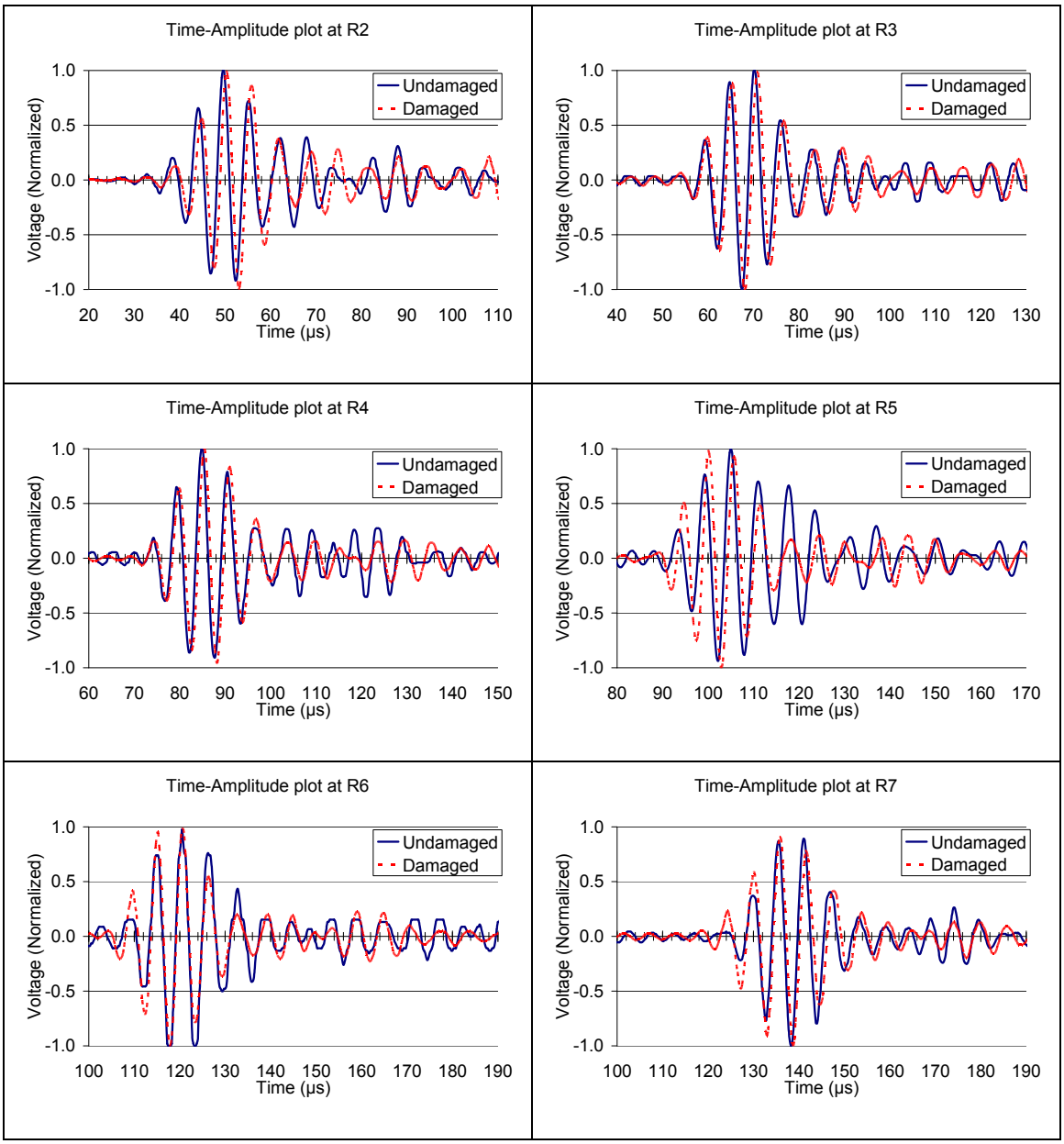

Figure 6-8: A magnified view of time-voltage plots for undamaged and damaged cases in the sandwich structure at 200 kHz central frequency obtained experimentally

The signals at receiver locations 2, 3 and 4 do not show significant changes in their waveforms, especially in the first part. Locations 5, 6, and 7 for the damaged signal there is a delay in the signal and also initial increase in the amplitude; the signals are magnified in Figure 6-6 and Figure 6-8 to view the delay.

Similar to section 6.2 a finite element simulation was carried out to evaluate the wave propagation characteristics in the disbonded sandwich structure. The calculated surface response for the undamaged and damaged cases at the receiver locations due to the modified source with 200 kHz central frequency is shown in Figure 6-9.

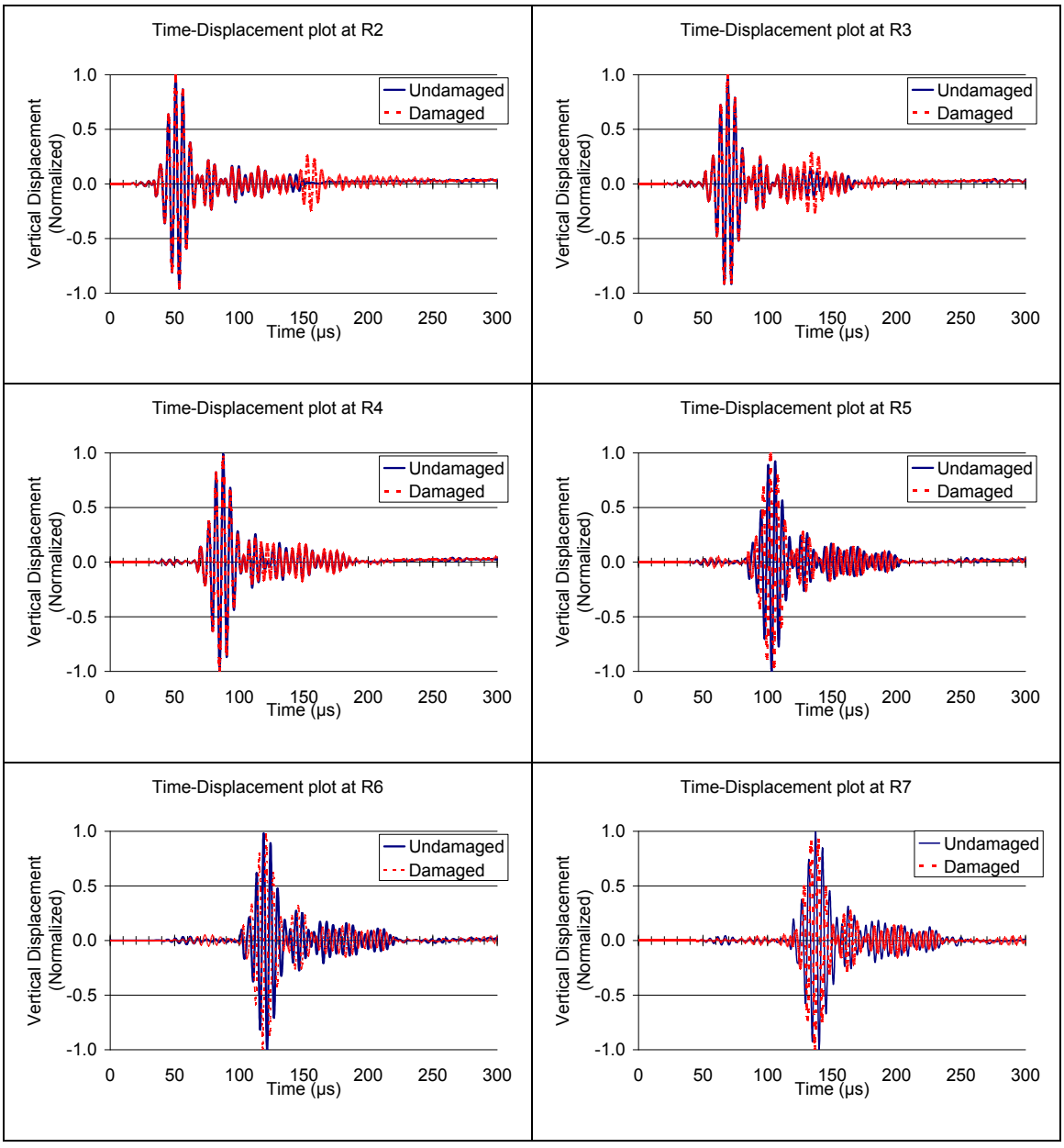

Figure 6-9: Time-voltage plots for undamaged and damaged cases in the sandwich structure at 200 kHz central frequency obtained numerically

Similar to experimentally obtained data, the responses at receiver locations 2, 3 and 4 do not show any significant changes in the waveform, specially the first part of the waveform. At locations 5, 6, and 7 for the damage case there is a delay in the signal and also initial increase in the amplitude. A magnified view of the signals is presented in Figure 6-10.

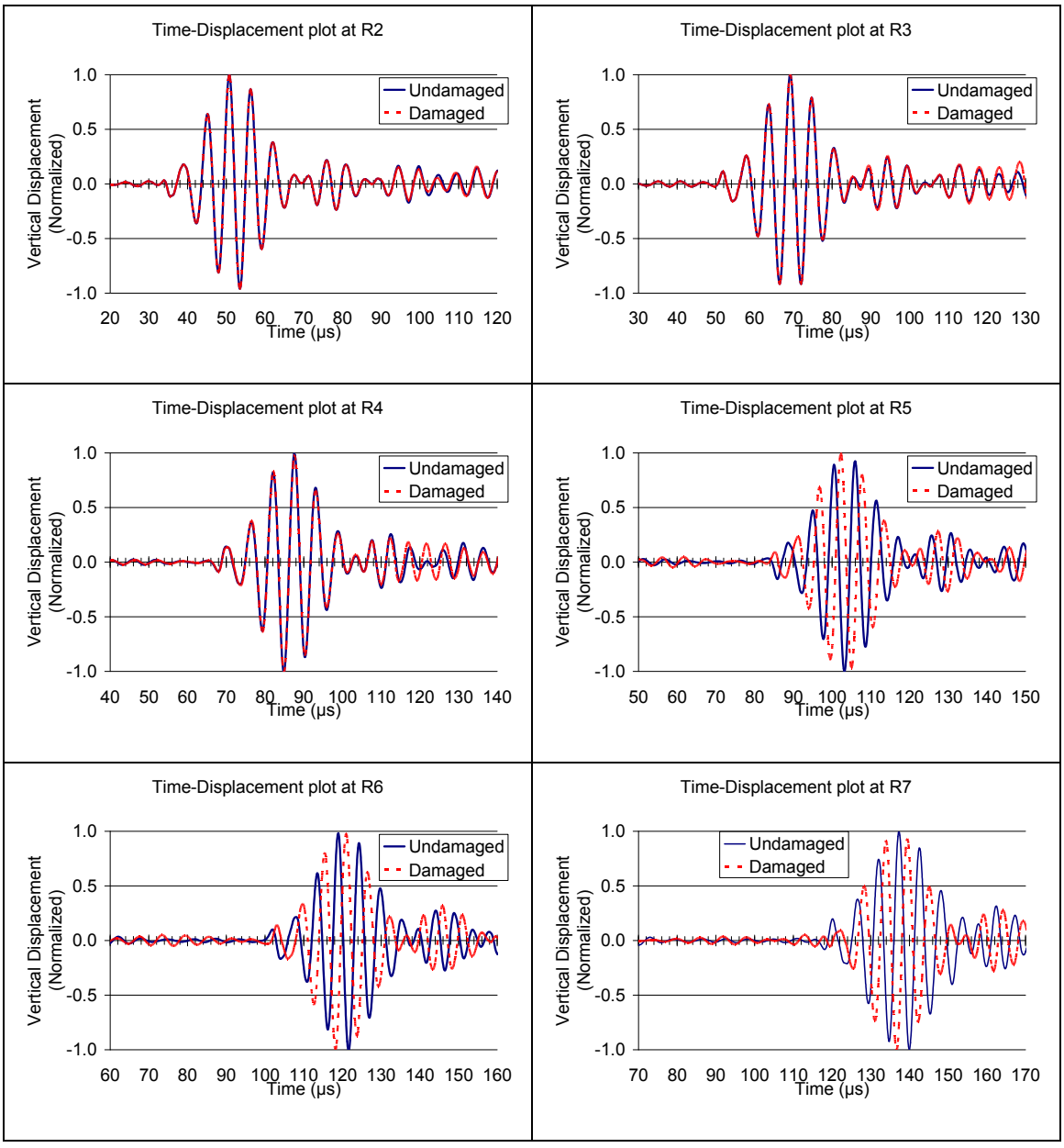

Figure 6-10: A magnified view of time-voltage plots for undamaged and damaged cases in the sandwich structure at 200 kHz central frequency obtained numerically

It can be seen that as result of the interaction between the propagating waves and the disbond, there is an initial increase in the amplitude as well as a delay in the signal. The simulations carried out using the finite element code, ABAQUS, for a two dimensional model of the problem gave a clear understanding of this feature and further it also predicts other expected features of the interaction process. Examples of the simulated displacement field with and without damage at different time interval is presented in Figure 6-11 and Figure 6-12. A more detailed image of wave interaction with damage is shown in Figure 6-13 and Figure 6-14. It is evident that as the wave profile encounters the disbonded region, it splits in two parts, with one traveling in the disbonded upper layer and the other below it. The delay in the signal is due to the slower propagation speed in the skin, the amplitude variation is due the complex interaction between the propagating waves and the disbond tips.

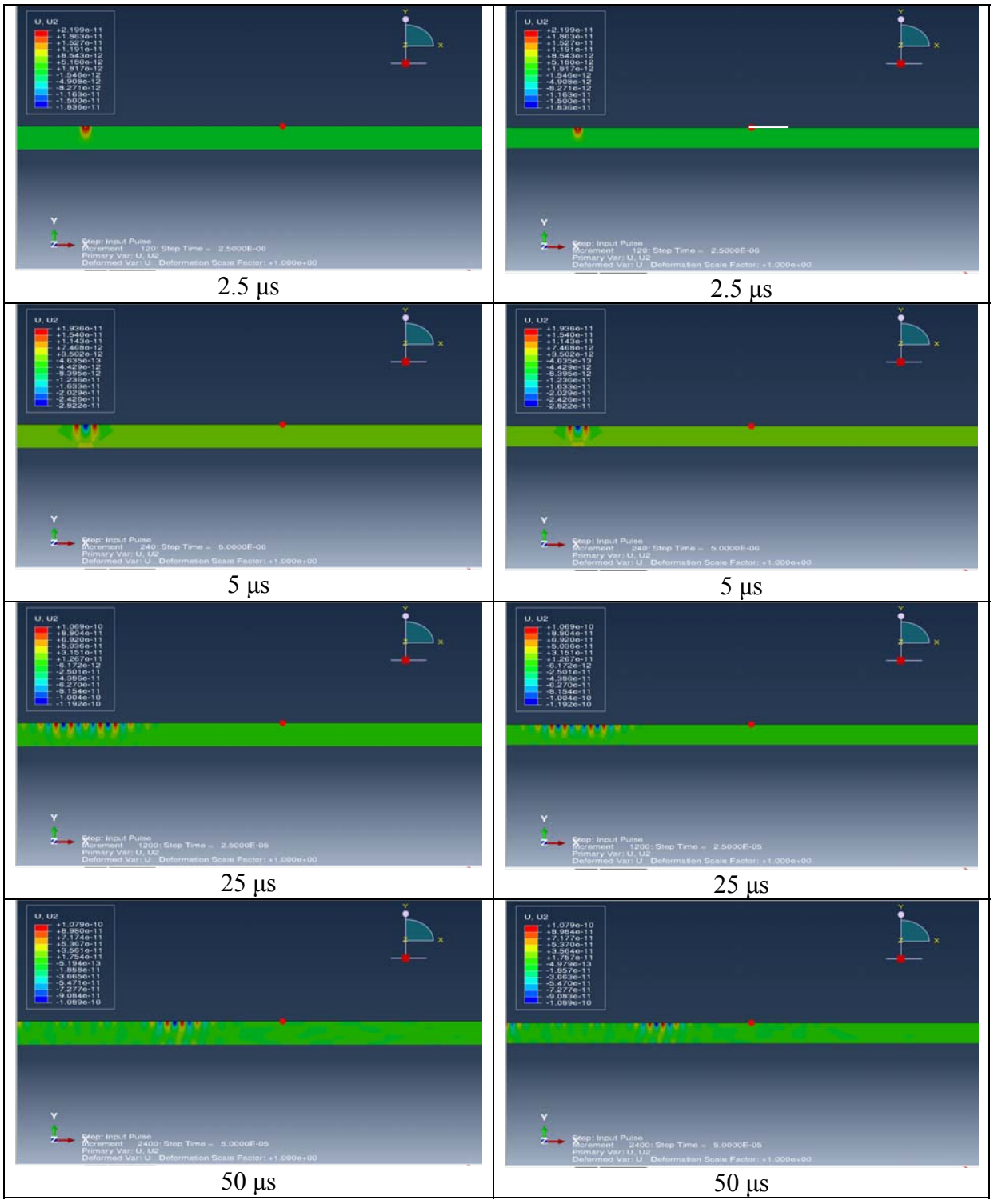

Figure 6-11: Contour plot of vertical displacement profile in an undamaged and damaged sandwich structure at time intervals for 2.5 µs to 50 µs

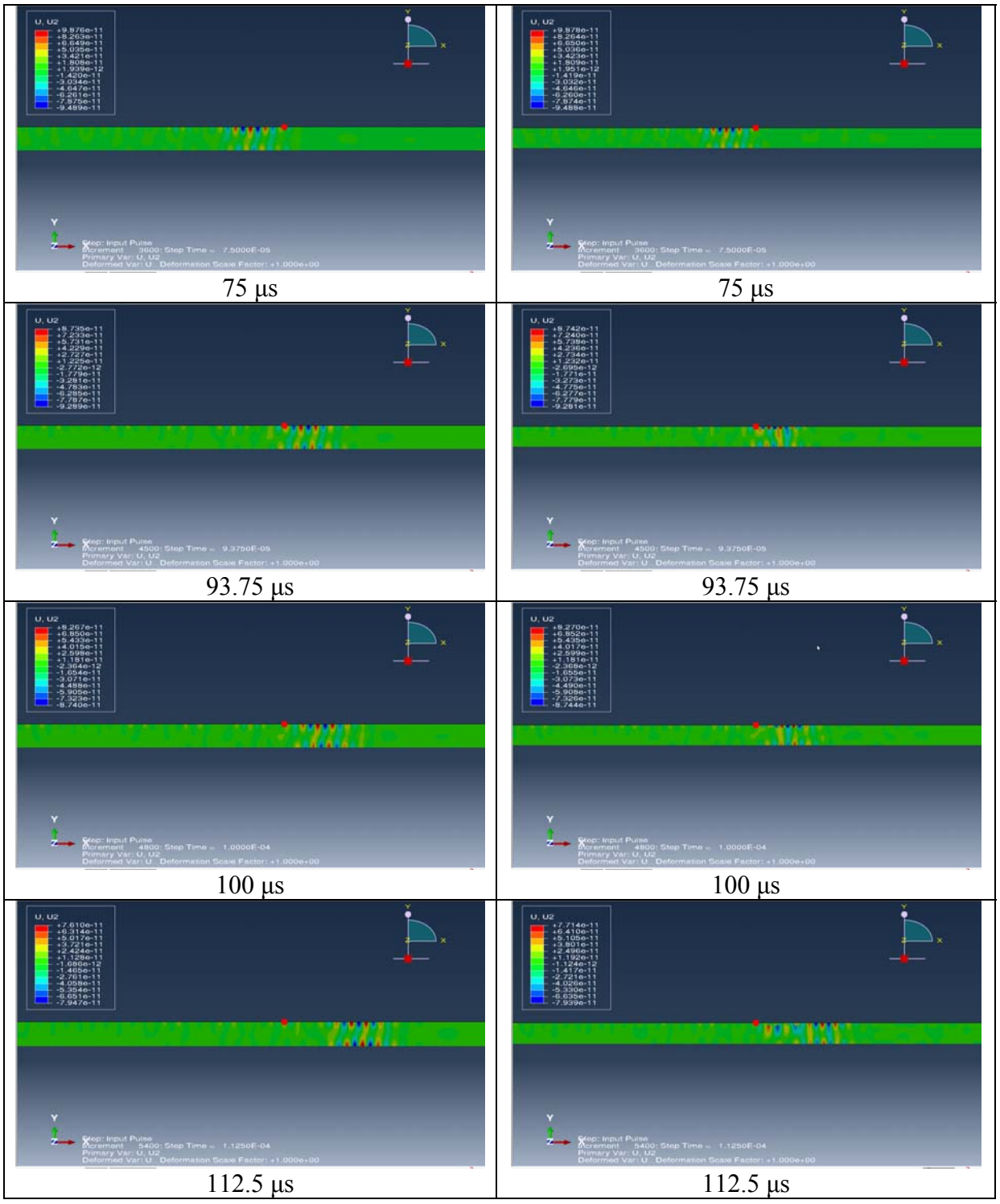

Figure 6-12: Same as Figure 6-11 at time intervals for 75 µs to 112.5 µs

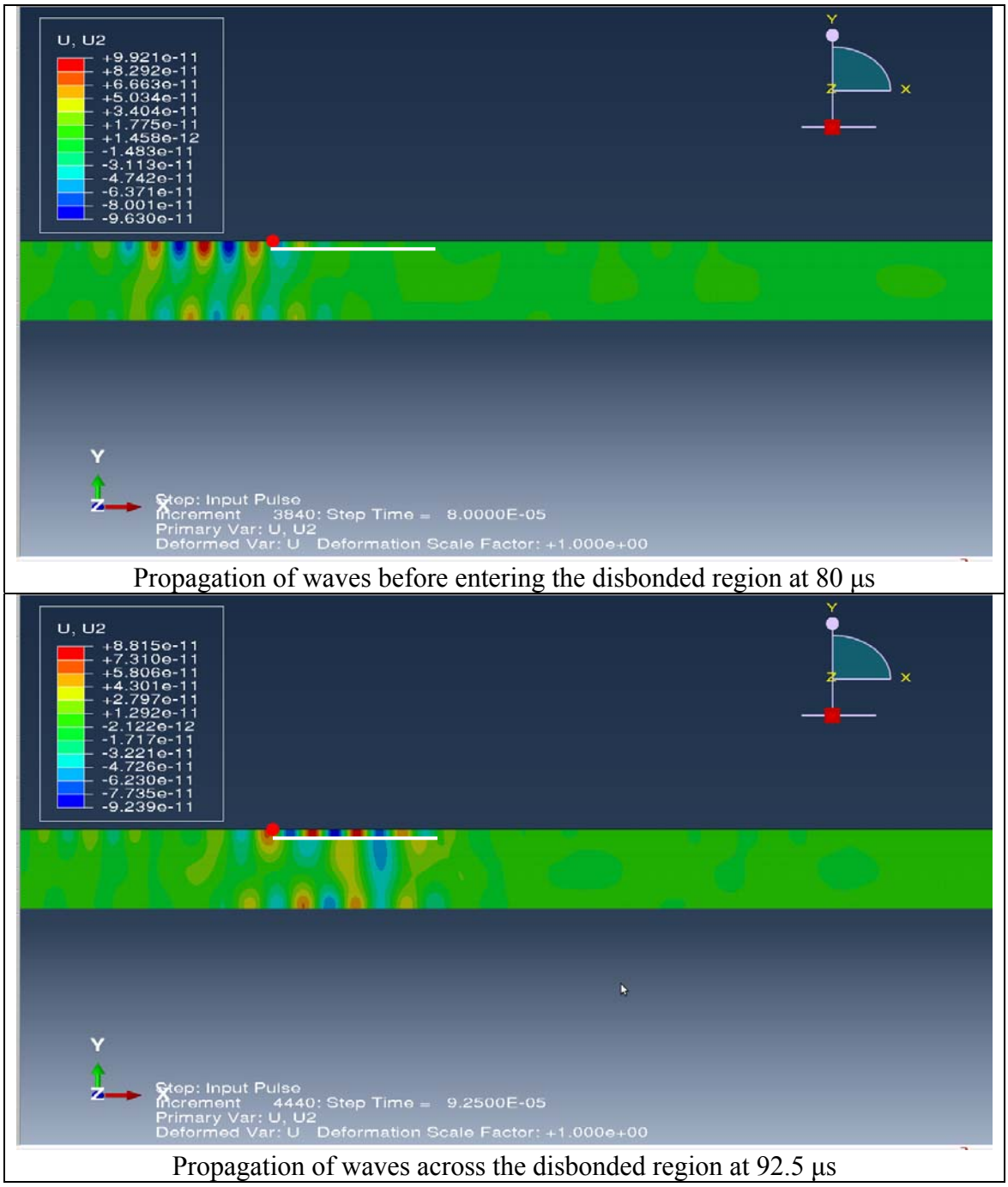

Figure 6-13: Contour plot of detailed vertical displacement profile in a damaged sandwich structure at 80 µs and 92.5 µs

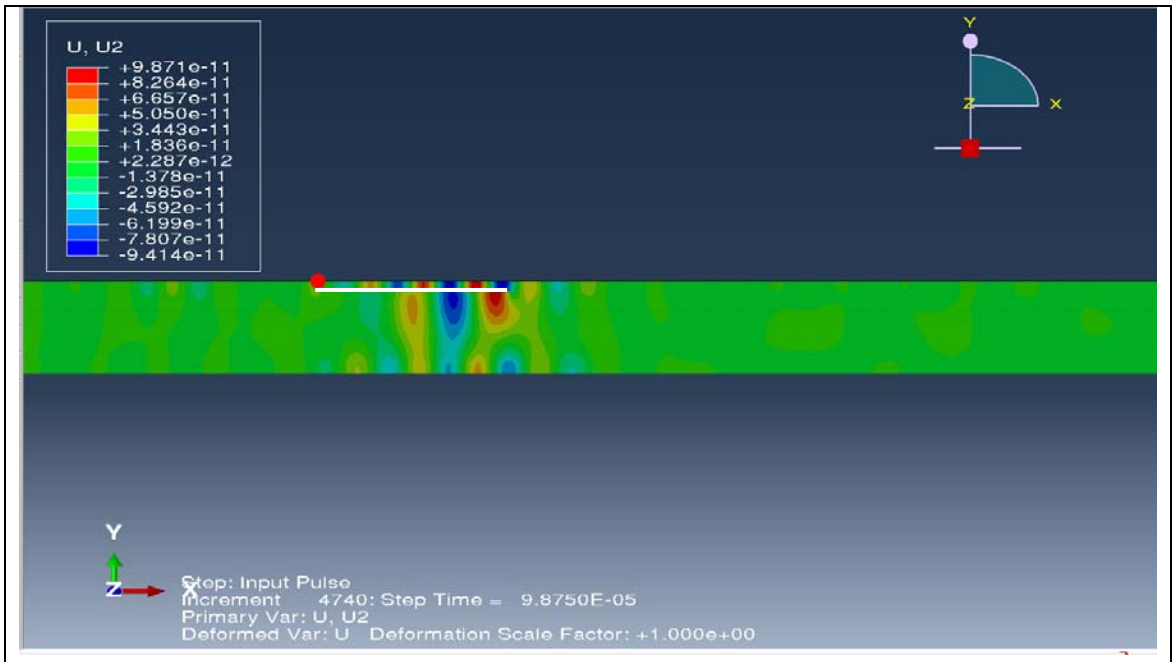

Propagation of waves across the disbonded region at 98.75 μs

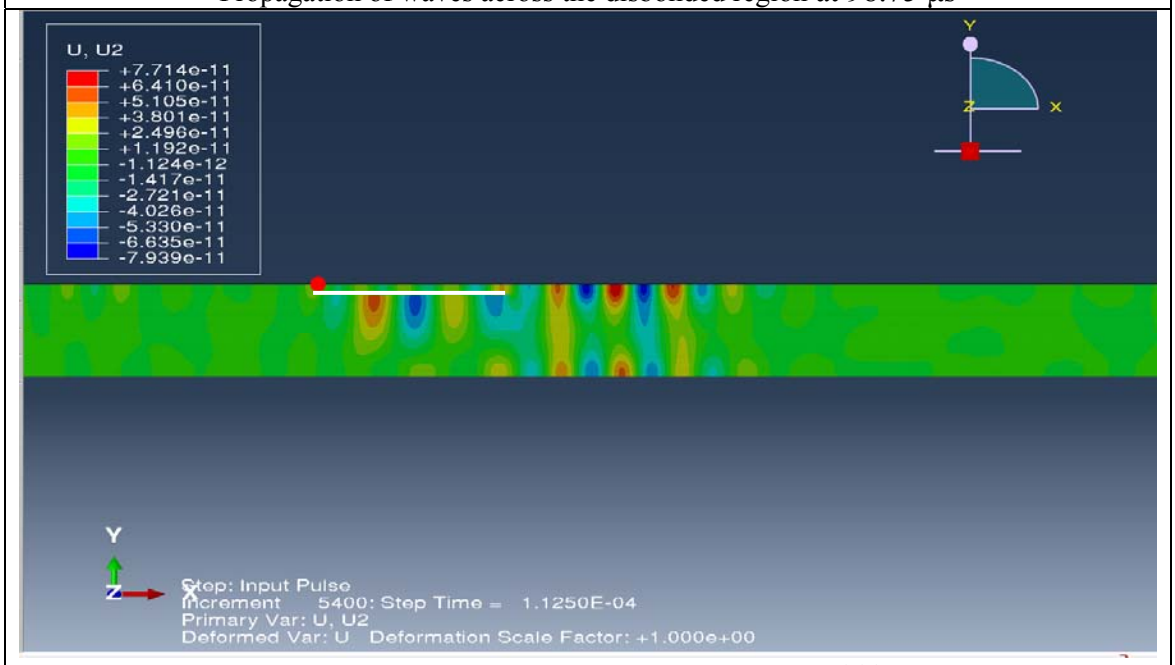

Propagation of waves after the disbonded region at 112.5 μs

Figure 6-14: Same as Figure 6-13 at 98.75 μs and 112.5 μs

Chapter 7 CONCLUDING REMARKS

7.1 Concluding Remarks

The ultrasonic signals obtained by surface-mounted, removable transducers in a woven composite panel and a sandwich plate consisting of an aluminum honeycomb core and woven composite face-sheets are analyzed. The results can be summarized as follows:

1. Guided waves can be efficiently transmitted along the surface of both the composite plate and the sandwich structure.
2. For both structures, adequate signal strength could be obtained at a distance of about 20 cm from the source at 2V and 200 kHz.
3. The damage index approach presented here can be used for detection and, under certain conditions, characterization of the degradation in aircraft, aerospace and civil structures. It is determined beyond a 99.5% confidence level that the higher damage indices near the impact were due to local changes in the FRFs.
4. As a result of the interaction between the propagating waves and the disbond like crack in a thick aluminum plate, there is a delay in the signal. The simulations carried out using the finite element code ABAQUS for a two dimensional model of the problem provided a clear understanding of this feature and also predicted other qualitative features of the interaction process.
5. As a result of the interaction between the propagating waves and the disbond in the honeycomb composite sandwich structure, there is an initial increase in the amplitude as well as a delay in the signal. As in the thick aluminum plate, the Finite Element simulations carried in a two dimensional model of the sandwich structure gave a clear understanding of this feature. It is evident that as the wave profile encounters the

disbonded region, it splits in two parts, with one traveling in the disbonded upper layer and the other below it. The delay in the signal is due to the slower propagation speed in the skin, the amplitude variation is due the complex interaction between the propagating waves and the disbond tips.

BIBLIOGRAPHY

[1] Gunn, L. C., "Operational Experience With Health Monitoring on The Delta II program", *Structural Health Monitoring*, F.-K. Chang ed., pp. 133-141, 2000.

[2] Alfonso-Zaldivar, R., "NASA to Study Tail Fin From Jet Crash", *Los Angeles Times*, November 30, Home Edition A37, 2001.

[3] Final Report of the X-33 Liquid Hydrogen Tank Test Investigation Team, NASA Marshall Space Flight Center, May 2000. [http://www.tc.cornell.edu/ Research/ CMI/RLVsource/Docs/NASA_x33tankreport.pdf]

[4] Mal. A.K., "Structural Health Monitoring," *Mechanics*, American Academy of Mechanics, Vol. 33, 2004.

[5] Mal, A.K, Ricci, F. and Banerjee, S., "A Conceptual Structural Health Monitoring System Based on Vibration and Wave Propagation", *Structural Health Monitoring: An International Journal*, **4**(3), pp. 283-293, 2005.

[6] Banerjee, S., Ricci, F., Shih, F. and Mal, A.K., "Health Monitoring of Composite Structures Using Ultrasonic Guided Waves," *Advanced Ultrasonic Methods for Material and Structure Inspection*,, T. Kundu, Hermes Science Publications, Paris, France, 43-86, 2007.

[7] Mal, A.K., Banerjee, S. and Ricci, F., "An Automated Damage Identification Technique Based on Vibration and Wave Propagation Data", *Philosophical Transactions of Royal Society A* **365**, pp. 479-491, 2007.

[8] Banerjee, S., Ricci, F., Monaco, E., and Mal, A.K., "Autonomous Impact Damage Monitoring in a Stiffened Composite Panel", *Journal of Intelligent Material Systems and Structures*, **18**, pp 623-633, 2007.

[9] Ajit Mal, Indu Saxena, Harsh Baid, and Dennis Keene, "Detection of disbonds in a honeycomb composite structure using guided waves," IWSHM, Stanford University, 2007.

[10] Harsh Baid, Sauvik Banerjee, Shiv Joshi, Siddhartha Mal, "Detection of disbonds in a honeycomb composite structure using guided waves," *Health Monitoring of Structural and Biological Systems 2008 Proceedings of SPIE*, **6935**, pp 693504-693504-5, Apr 2008.

[11] Banerjee, S., Ricci, F., Monaco, E., Mal, A. K., "A Wave Propagation and Vibration-based Approach for Damage Identification in Structural Components", *Journal of Sound and Vibration,* **332** (1-2), 167-183, 2009.

[12] Sauvik Banerjee, Fabrizio Ricci, Harsh Baid, Ajit K. Mal, "Dynamic based damage detection in composite structures," *Health Monitoring of Structural and Biological Systems 2009 Proceedings of SPIE*, **7295**, pp. 72950H-72950H-5, Apr 2009.

[13] Aki, K. and Richards, P. G., *Quantitative Seismology, Theory and Methods*, Freeman, San Francisco, 1980.

[14] Nayfeh, A. H., Wave Propagation in Layered Anisotropic Media: With Applications to Composites, Amsterdam, Elsevier Science, 1995.

[15] Mal, A. K. and Bar-Cohen, Y., "Ultrasonic Characterization of Composite Laminates," *ASME-SES Symposium on Wave Propagation in Structural Composites*, A. K. Mal and T. C. T. Ting, ed., *AMD*, **99**, pp. 1-16, 1988.

[16] Rose, J. L., *Ultrasonic Waves in Solid Media*, Cambridge University Press, New York, 1999.

[17] Yoseph Bar-Cohen, Ajit K. Mal and Donald J. Roth, "Ultrasonic Testing of Advanced Materials" *Nondestructive Testing Handbook*, Patrick Moore, Gary Workman and Dorn Kishoni, American Society for Nondestructive Testing, Columbus, Ohio, **7**, pp. 357 – 397, 2007.

[18] Mal, A.K., "Wave Propagation in Layered Composite Laminates under Periodic Surface Loads", *Wave Motion*, Vol. 10, pp. 257-266, 1988.

[19] Mal, A.K., Yin, C.-C., and Bar-Cohen, Y., "Analysis of Acoustic Pulses Reflected from Fiber-Reinforced Composite Laminates", *J. Appl. Mech*., **59**, pp. 136-144, 1992.

[20] Mal, A.K., and Lih, S.-S., "Elastodynamic Response of a Unidirectional Composite Laminate to Concentrated Surface Loads: Part I", *J. Appl. Mech.,* **59**, pp. 878-886, 1992.

[21] Lih, S.-S., and Mal, A.K., "Elastodynamic Response of a Unidirectional Composite Laminate to Concentrated Surface Loads: Part II", *J. Appl. Mech.,* **59**, pp. 887-892, 1992.

[22] Lih, S.-S., and Mal, A.K., "On the Accuracy of Approximate Plate Theories for Wave Field Calculations in Composite Laminates", *Wave Motion*, **21**, pp. 17-34, 1995.

[23] Lih, S.-S., and Mal, A.K., "Response of Multilayered Composite Laminates to Dynamic Surface Loads", Guo, D., Mal, A. K. and Ono, K., "Wave Theory of Acoustic Emission in Composite Laminates," *J. Acoust. Emission*, **14**, pp. S19-S46, 1996

[24] Mal, A.K., "Elastic Waves from Localized Sources in Composite Laminates," *Int. J. Solids and Structures*, **39**, pp 5481-5494, 2002.

[25] Mal, A., Shih, F. and Prosser, W., "Lamb waves from impact damage in composite plates," *Instrumentation - Measure –Metrologie,* Special Issue on Ultrasonic Methods for Material Characterization, **3**, pp 11-37, 2003.

[26] Banerjee, S., Prosser, W.H. and Mal, A.K, "Calculation of the Response of a Composite Plate to Localized Dynamic Surface Loads Using a New Wavenumber Integral Method", *ASME Journal of Applied Mechanics*, **72(1)**, pp. 18-24, 2005.

[27] Banerjee, S. and Mal, A.K., "Acoustic Emission Waveform Simulation in Multilayered Composites", *Journal of Strain Analysis for Engineering Design*, 40(1), pp 25-32, 2005.

[28] Guo, D., Mal, A. K., Ono, K., "Wave Theory of Acoustic Emission in Composite Laminates," *Journal of Acoustic Emission*, **14**, S19-S46, 1996.

[29] Chimenti, D. E., "Guided Waves in Plates and Their Use in Material Characterization," *Applied Mechanics Review*, **50**, pp. 247-284, 1997.

[30] Banerjee, S., Prosser, W. H., Mal, A. K., "Analysis of Transient Lamb Waves Generated by Dynamic Surface Sources in Thin Composite Plates", *Journal of the Acoustical Society of America*, **115 no. 5**, pp. 1905-1911, 2004.

[31] Gary, J., Hamstad, M., "On the Far-field Structure of Waves Generated by a Pencil Break on a Thin Plate," *Journal of Acoustic Emission*, **12 no. 3-4**, pp. 157-170, 1994.

[32] Prosser, W. H., Hamstad, M.A, Gary, J., O'Gallagher, A., "Comparison of Finite Element and Plate Theory Methods for Modeling Acoustic Emission Waveforms," *Journal of NDE*, **18 no 3**, pp. 83-90, 1999.

[33] Gibson, L. J., and Ashby, M. J., "*Cellular Solids: Structure and Properties*", Cambridge University Press, Cambridge, U.K., 2nd ed., 1997.

[34] Naik, R. A., "Analysis of Woven and Braided Fabric Reinforced Composites," *NASA Contractor Report CR-194930*, 1994.

[35] Hashin, Z., "Theory of Fiber Reinforced Materials," *NASA Report No. NASA-CR-1974*, NASA, Washington, DC, 1972.

[36] Whitcomb, J. and Xiadong, T., "*Effective* Moduli of Woven Composites," *Journal of Composite Materials*, **35**, No. 23, pp. 2127-2144, 2001.

[37] Naik, N. K., and Ganesh, V. K., "An analytical method for plain weave fabric composites," *Composites*, **26**, Issue 4, pp. 281-289, 1995.

[38] Jones, R. M., "*Mechanics of Composite Materials*", Taylor & Francis, Inc., Philadelphia, U.S.A., 2nd ed., 1999.

[39] Challa, P. and Shivakumar, K. (2001). mmTEXlam - A Graphical User Interfaced Design Code for Laminated Textile Fabric Composites , *In: 42nd AIAA/ASME/ASCE/AHS/ASC Structures, Structural Dynamics, and, Materials Conference and Exhibit*, Seattle, WA, April 16-19, AIAA-2001-1571.

[40] Mal, A.K. and Singh, S., 1991, *Deformation of Elastic Solids*, Prentice Hall, New Jersey.

[41] Lamb H. On waves in an elastic plate. Proc R Soc A – Math Phys Eng Sci; **93(648)**: pp. 114–28, 1917.

[42] Vallen Systeme, The Acoustic Emission Company.

[43] Takemoto, M., Nishino, H. and Ono, K., "Wavelet Transform - Applications to AE Signal Analysis", *Acoustic Emission - Beyond the Millenium*, Elsevier, pp. 35-56, 2000.

[44] Suzuki, H., Kinjo, T., Hayashi, Y., Takemoto, M. and Ono, K., Appendix by Hayashi Y., "Wavelet Transform of Acoustic Emission Signals", *J. of Acoust. Emission*, **14 (2)**, pp. 69-84, 1996.

[45] Abaqus/CAE 6.10-1.